UNIVERSITY OF OKLAHOMA

GRADUATE COLLEGE

ALBEDOS IN THE KUIPER BELT

A DISSERTATION

SUBMITTED TO THE GRADUATE FACULTY

in partial fulfillment of the requirements for the

Degree of

DOCTOR OF PHILOSOPHY

By

MELISSA J. BRUCKER
Norman, Oklahoma
2009

ALBEDOS IN THE KUIPER BELT

A DISSERTATION APPROVED FOR THE
HOMER L. DODGE DEPARTMENT OF PHYSICS AND ASTRONOMY

BY

_____
Dr. William Romanishin (Chair)

_____
Dr. John Cowan

_____
Dr. Karen Leighly

_____
Dr. Susan Postawko

_____
Dr. Deborah Watson

Acknowledgements

This PhD dissertation would not have been possible without my Lowell Observatory advisor Will Grundy who directed this research project and provided invaluable assistance and insights into the subject. This work is based on observations made in Cycle 1 program P3542 with the Spitzer Space Telescope, which is operated by the Jet Propulsion Laboratory, California Institute of Technology under a contract with NASA. Support for this work was provided by NASA through an award issued by JPL/Caltech. I thank the Deep Ecliptic Survey team for allowing access to their orbit integration results.

This dissertation is presented in loving memory of my dearly departed grandparents Charles A. Brucker, Naomi (Ball) Brucker, and Robert L. Kurtz, Sr. and my dearly departed friends Merinda Rossello, Jason Kumor, and Julie Jogwick.

I would like to thank my family for all of their support and encouragement: my parents James D. Brucker and Marie A. (Kurtz) Brucker, my sister Suzanne Marie Brucker Heiney, my brother-in-law Robert Heiney, and my grandmother, Lois (Bandelow) Kurtz. My father had thought that I finished college in 1999. After eight more years of school, on this one point at least I have proved him wrong.

I also thank Lisa Prato for her support and encouragement and for her efforts without which Lowell Observatory's pre-doctoral fellowship program would not have become a reality. Thank you to the director of Lowell Observatory (retired), Bob Millis, and to the observatory staff.

Thank you to all of my OU compadres: Kimberly Prescott for an excellent example of a PHY/AST department thesis, Juliette (Rupert) Dalhed and Stacey (Long)

Lyne for teaching me the astronomy needed for the qualifying exam, Tim Wofford for teaching me what a Hamiltonian is, Chris McRaven for programming insights, Rachel (DeYoung) Hughes, Karen Bottoms, Allison (McCoy) Fleshman, Bobby Fleshman, Larry Maddox, Aida Nava Jason Collier, Logan Cox, and Mandy Rominsky.

I acknowledge Tim Marsh and Mr. Taylor for turning me into who I am today and thank Karl J. Wolf, Eric Fitton, Sean Williams, and Kevin J. Davis for keeping me put together with help from Ani (Grover) Wiggins, Christine Marable, Julie (Tilli) Poisson, Joey Martin, Chris Poisson, Autumn Chapman, and music. A world without music is empty indeed.

Table of Contents

List of Tables

Page

List of Figures

Abstract

I have focused my research on the visual geometric albedos of transneptunian objects (TNOs), how the albedo varies with dynamical class, and whether or not it is correlated to orbital parameters. TNOs are among the least-processed objects in the solar system. By studying them, we can learn about the conditions in the solar system: the density of matter in the protoplanetary disk, the composition of different primordial regions, planetary migration, stirring of the disk, stellar close encounters, collision histories, binary capture, and space weathering. What we learn about how our solar system evolved also can be applied to debris disks surrounding other stars.

Using infrared images from the Multiband Imaging Photometer for *Spitzer* (MIPS) on the *Spitzer Space Telescope* (*SST*), I measured the thermal flux in two different wavelength bands for sixteen transneptunian objects with point-spread function (PSF) fitting photometry. I converted the measurements to monochromatic flux densities at 23.68 μm and 71.42 μm. Next, I fit the Standard Thermal Model (STM), employing a linear function for the phase integral and Monte Carlo simulations, to the flux measurements and the absolute visual magnitude for each object in order to constrain its albedo and radius. Fitting a thermal model to infrared thermal radiation measurements resolves the ambiguity found with visual reflected radiation between a small object with a high albedo and a large object with a low albedo as they would have different temperatures. Once accurate albedos and radii are determined, they can be applied to size and mass distributions of the Kuiper belt.

The sample was constructed from new targets and those previously published in the work of Stansberry et al. (2008), Grundy et al. (2005), and Grundy et al. (2009). A

correlation was found between albedo and inclination for Classical Kuiper belt objects (KBOs) not including inner Classicals. The dynamically cold Classicals have higher albedos than hot Classicals. The albedos of the two populations are drawn from different parent distributions if one assumes an inclination break between them of 2.4º to 8.8º. It has already been shown that cold Classicals and hot Classicals differ in color, magnitude, and binary fraction. The high albedos of cold Classicals extend support for orbital dynamic theories that involve different formation regions, methods of transport, or surface alterations for the hot and cold Classical KBO populations. In addition, the high albedos found for cold Classical KBOs reduce the estimate for the total mass in this region by almost an order of magnitude.

Chapter 1

Introduction

Transneptunian objects (TNOs) are small, icy objects in the outer solar system between Neptune and the Oort cloud. They are among the least processed objects available for study in our solar system having never been in close proximity to the Sun. As such, they can reveal clues to planet formation, the conditions of the early solar system, and their evolutionary history. Figures 1.1 and 1.2 show the current known positions of minor planets discovered in the outer solar system as estimated by their ecliptic latitude and ecliptic longitude respectively. In this chapter, we will introduce the major dynamic classification schemes, some discovery surveys and magnitude distribution estimates, general properties, orbital evolution theories, and the objective of this dissertation.

1.1 Classification Schemes

Objects in the outer solar system are classified into categories based on their orbital dynamic properties. The two main classification systems are from the Deep Ecliptic Survey (DES) team (Elliot et al. 2005) and Gladman et al. (2008). Lykawka and Mukai (2007b) also have defined a classification system on which I will not elaborate. Here, the term Kuiper belt object (KBO) is used interchangeably with TNO.

The DES system (Elliot et al. 2005) takes the observed orbital elements of a TNO candidate and forward integrates the object's trajectory under the influence of the Sun and the gas giants for 10 Myr assuming that the object is a massless test particle. Membership in one of five categories is based on the results of the orbital integrations. If

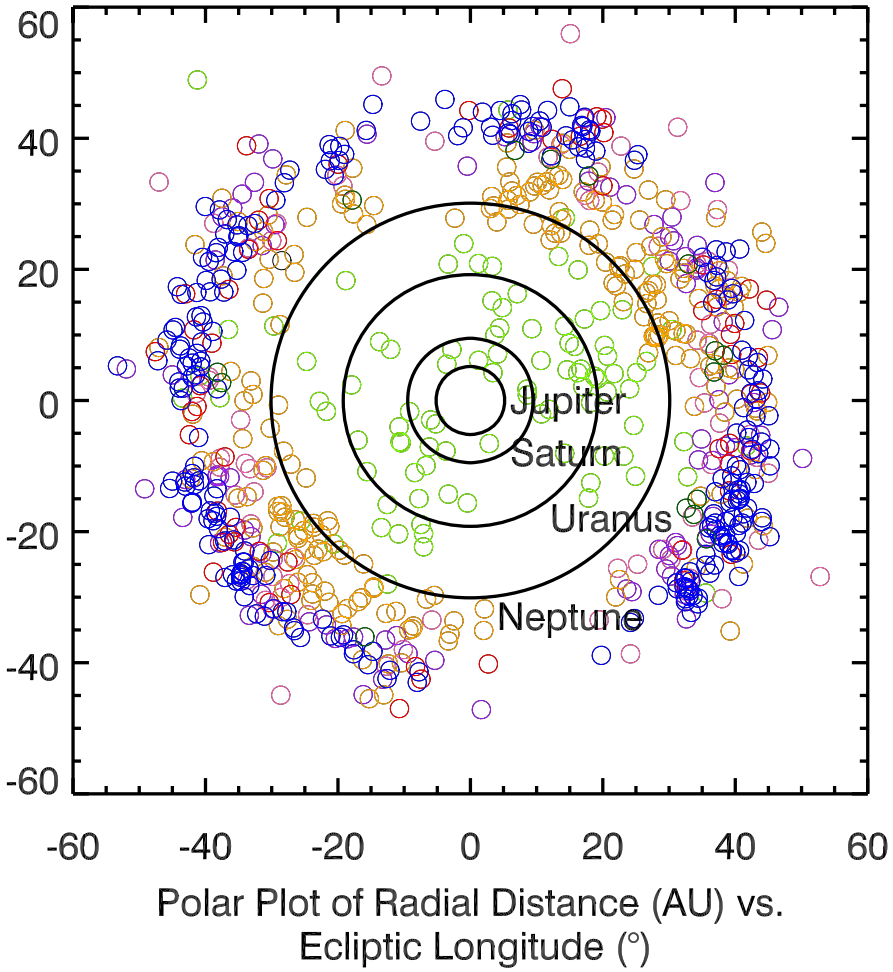

Figure 1.1. The approximate current positions of TNOs and Centaurs (ecliptic longitude vs. distance from the Sun). Centaurs are shown in light green, Resonant objects are orange, Scattered-Near KBOs are pink, Scattered-Extended KBOs are purple, inner Classicals are dark green, cold Classicals are blue, and hot Classicals are red. The black circles represent the semimajor axes of the giant planets. Direct motion of bodies is in the counterclockwise direction. The apparent lack of objects in the lower right hand corner is due to detection difficulties arising from the Milky Way lying in the background.

the object experiences bounded oscillations such that one or more resonant arguments librate, then it is in mean motion resonance (MMR) with Neptune and considered to be a Resonant KBO. Elliot et al. (2005) originally only tested MMRs up through the fourth order (for a resonance *p:q*, the order is *p-q* where *p* represents the number of orbits completed by the inner object while *q* orbits are completed by the outer object where *p* and *q* must be integers). Pluto is a 3:2 Resonant KBO; thus, other 3:2 Resonant KBOs

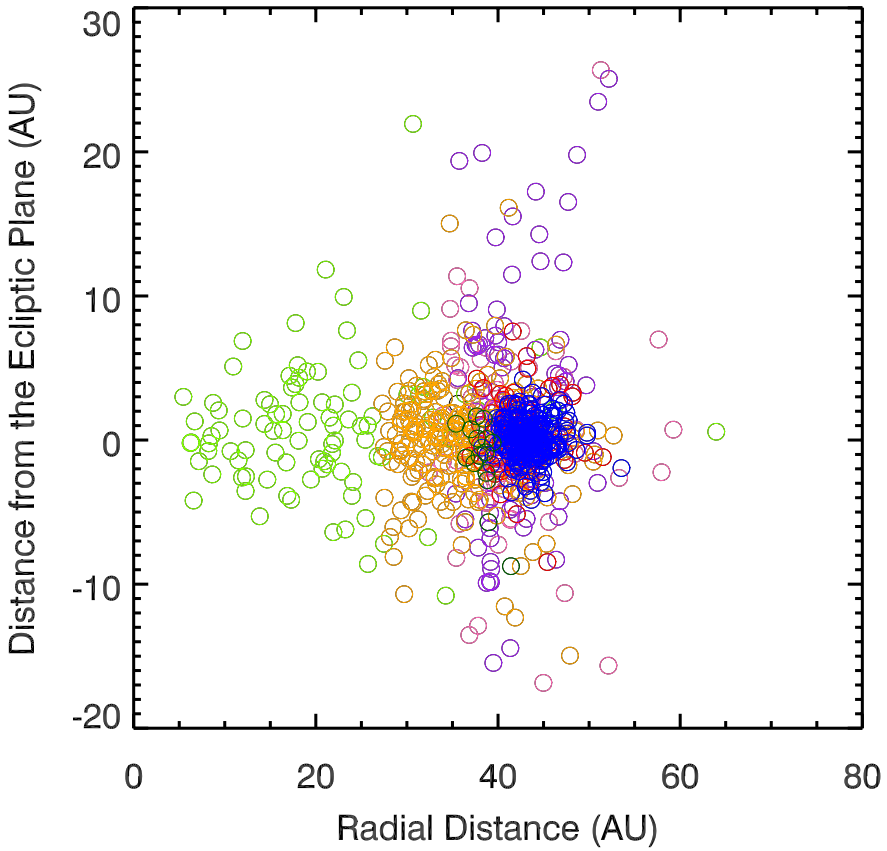

Figure 1.2. The approximate current positions of TNOs and Centaurs (distance from the Sun multiplied by the sine of the ecliptic latitude vs. distance from the Sun). The colors are as in Figure 1.1. The region between 39.5 AU and 48 AU contains many overlapping symbols due to the concentration on the ecliptic plane of many discovery surveys.

are often referred to as Plutinos (not to be confused with dwarf planet TNOs that are sometimes referred to as Plutoids).

If the object is not resonant, next it is determined whether or not the object is a Centaur. Centaurs have perihelia less than the semimajor axis of Neptune. Since Centaurs have giant planet-crossing orbits, their orbits are dynamically unstable and they have short lifetimes relative to the age of the solar system.

If the object is not a Resonant KBO or a Centaur, then its Tisserand parameter with respect to Neptune is calculated. The Tisserand parameter is a constant of the

motion in a restricted circular three body dynamical problem and describes the amount of interaction between the two smaller bodies (in this case Neptune and the TNO). It is given by:

$$T_N = a_N / a + 2\cos(i)\sqrt{\left(1 - e^2\right) a / a_N} \tag{1.1}$$

where a_N is Neptune's average semimajor axis, a is the object's semimajor axis, i is the object's average inclination, and e is the object's average eccentricity. Objects with $T_N <$ 3 are designated as Scattered-Near KBOs. Objects with $T_N > 3$ and average eccentricities $e > 0.2$ are Scattered-Extended objects (the division in eccentricity was arbitrarily chosen to select objects with large eccentricities). The remaining TNOs that have orbital solutions with acceptable errors are Classical KBOs (those with $T_N > 3$ and $e < 0.2$). Classical KBOs, or Classicals, comprise the main Kuiper belt. These objects with low to moderate eccentricities and inclinations have semimajor axes between Neptune and about 50 AU. Classicals can be divided into three groups. The dynamically hot Classicals have moderate to high inclinations and eccentricities and the dynamically cold Classicals have low inclinations and eccentricities. The hot and cold Classicals mainly reside between 40 AU and 50 AU. Inner Classicals have semimajor axes interior to the 3:2 MMR with Neptune ($a < 39.46$ AU). The inner Classicals recently have been found to be distinct from the cold Classicals (Romanishin et al. 2008, 2009). See Figure 1.3 for the population distribution of detected TNOs with well-defined orbits.

The main difference between the classification systems of Gladman et al. (2008) and the DES system lies in the description of scattered disk objects (SDOs). In the Gladman et al. (2008) system, objects are classified based on their current orbital elements and the results from a 10 Myr orbital integration. First, the semimajor axis must

be greater than that of Jupiter. Jupiter family comets have perihelia less than 7.35 AU and Tisserand parameters with respect to Jupiter less than 3.05. To separate Centaurs in gas giant-crossing orbits from TNOs, Centaurs have semimajor axes less than Neptune's. In the Gladman et al. (2008) system, the outer edge of the transneptunian region is given by a = 2000 AU, the point at which galactic forces are appreciable. Objects with a > 2000 AU are members of the Oort cloud.

Objects between the Centaurs and the Oort cloud are divided into four categories in the system of Gladman et al. (2008): Resonant objects, Scattering Disk Objects, Detached, and Classical Kuiper belt objects. Resonant objects have angular orbital elements such that a resonant argument librates. Gladman et al. (2008) examined resonances up through sixth order and also searched for higher order resonances where the object is currently in resonance (and not necessarily at the end of the 10 Myr integration). Including higher order resonances means that some DES Scattered-Extended and Scattered-Near objects may be Resonant according to Gladman et al. (2008).

If a TNO is not Resonant and it is 'currently scattering off Neptune', then it is designated as a Scattering Disk Object. An SDO is identified by its swift changes in semimajor axis during integration. An object is a member of the Detached TNO population if its eccentricity is greater than 0.24. This eccentricity is greater than in the DES system so that stable objects with the same eccentricity lying on either side of the 2:1 MMR are both considered to be Classical. The designation of Detached is used as opposed to Scattered-Extended since the transport mechanism from their primordial to current orbits for these objects is still under debate. The remaining objects are members

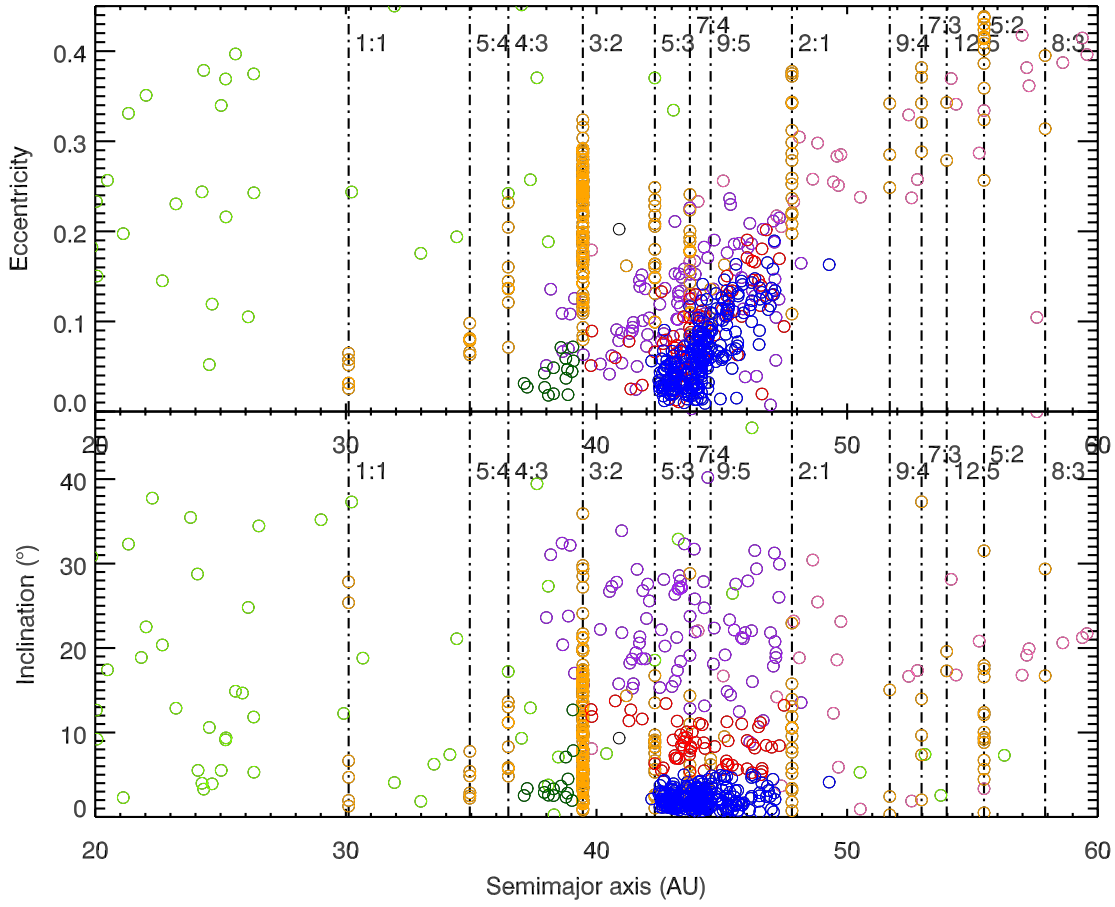

Figure 1.3. Plots of eccentricity and inclination with respect to semimajor axis. Objects are sorted by their DES classification (Elliot et al. 2005). Centaurs are plotted in light green, Resonant objects are orange, cold Classical KBOs are blue, hot Classical KBOs are red, inner Classical KBOs are dark green, Scattered-Near KBOs are pink, and Scattered-Extended KBOs are purple. This plot is not all-inclusive for TNOs. Of the total 1342 discovered objects (according to the May 2009 issue of *Distant EKOs: the Kuiper Belt Electronic Newsletter*), we have 811 DES-classified objects. Only a majority of the classified objects appear in this figure as their semimajor axes range from 6.2 AU to 767 AU, their eccentricities range from 0.007 to 0.96, and their inclinations range from 0.26º to 105º (objects with inclinations greater than 90º orbit in retrograde motion).

of the Classical belt. They consist of the inner belt (a < 39.4 AU), the outer belt (a > 48.4 AU and e < 0.24; 48.4 AU is the approximate location of the 2:1 MMR), and the main belt (39.4 AU < a < 48.4 AU). Some of the DES Scattered-Near and Scattered-Extended objects are Classical in this system. Gladman et al. (2008) acknowledge the dynamically hot and cold populations but do not pick a dividing inclination since a divisor is arbitrary

at this point in investigations. We will use a dividing inclination of 5º with respect to the invariable plane of the solar system (the plane centered about the solar system's center of mass and perpendicular to its angular momentum vector) for purposes of analysis as objects near 5º inclination may belong to either the hot or the cold population and their membership should be evaluated on a case-by-case basis.

Tegler and Romanishin (2000) noticed that the KBOs with low eccentricity and low inclination in their observational sample were all red. Levison and Stern (2001) also noticed that brighter objects tend to have higher inclinations. Then, Brown (2001) noted that the Classical Kuiper belt inclination distribution is well-fit by two Gaussians. Thus a distinction was made between dynamically hot and cold Classicals in view of the fact that the cold population has different properties than other TNO populations. The cold Classical population is red in V-R whereas hot Classicals range from gray (solar) to red (Tegler and Romanishin 2000, Trujillo and Brown 2002, Doressoundiram et al. 2002, Tegler et al. 2003, Gulbis et al. 2006, Chiang et al. 2007, Doressoundiram et al. 2008, Morbidelli et al. 2008) although no red hot Classicals have been measured above an inclination of 20º (Peixinho et al. 2004). The cold Classicals are less likely to be intrinsically brighter than hot Classicals (Morbidelli et al. 2008) "as objects with absolute visual magnitudes brighter than 6.5 tend to have higher inclinations than objects with absolute magnitudes fainter than 6.5 (Levison and Stern 2001)" (Brucker et al. 2009). Cold Classicals also have a higher rate of binarity than hot Classicals. Noll et al. (2008b) determined a binary fraction of $29.3^{+7.3}_{-6.4}\%$ for observed cold Classicals (17 of 58 objects). For hot Classicals, the binary fraction was only $9.3^{+6.7}_{-4.4}\%$ (4 of 43 objects). I will show that cold Classicals also have a different albedo distribution than hot Classicals.

1.2 Observational Surveys and Luminosity Distribution Functions

The discovery of new objects in the Kuiper belt began with 1992 QB_1 long after the serendipitous discovery of Pluto during a directed search for Planet X by Clyde Tombaugh at Lowell Observatory. Since then, several surveys have been conducted to find additional objects and determine the power law magnitude distribution of TNOs. A table of Kuiper belt surveys can be found in Kavelaars et al. (2008) along with a discussion on debiasing survey results.

The Deep Ecliptic Survey is responsible for the greatest number of discoveries, having found 382 objects with designations and 240 undesignated objects at the time of their manuscript preparation (Elliot et al. 2005). Their intermediate-magnitude survey reached 50% sensitivity at a VR magnitude of 22.5 and covered 500 deg^2 of sky by the end of 2003.

The sky density of KBOs brighter than *m* at a Kuiper belt plane latitude of 0º is given by:

$$\sum(<m,0) = 10^{\alpha(m-m_0)} \tag{1.2}$$

where m_0 is the magnitude at which the sky density of brighter objects at opposition is 1 deg^{-2} and α is the logarithmic slope of the distribution. This equation is sometimes referred to as the apparent luminosity function. Elliot et al. (2005) fit the magnitudes of their sample with a single power law distribution with $\alpha = 0.86 \pm 0.10$ and $m_0 = 22.70 \pm 0.13$ or $\sum(<m,0) = 10^{0.86(m-22.70)}$. A review of luminosity function surveys can be found in Petit et al. (2008).

Bernstein et al. (2004) is widely used as a reference for the size distribution and total mass of TNOs. They combine the results of their survey for faint objects, which is

50% complete at 0.606 μm wavelength magnitude of 29.2, with those of Chiang and Brown (1999), Gladman et al. (2001), Allen et al. (2002), Trujillo et al. (2001), Larsen et al. (2001), and Trujillo and Brown (2003). They found that both the faint and bright ends of the magnitude range depart from a single power law distribution. They fit the R magnitude distribution with a double power law with $\alpha_1 = 0.88$ for bright objects, $\alpha_2 = 0.32$ for faint objects, and equal contribution at a magnitude R = 23.

Petit et al. (2006) conducted a survey with the primary goal of discovering irregular satellites of Uranus and Neptune. Towards that aim, they searched 5.97 deg^2 of sky near Uranus and 5.88 deg^2 near Neptune and discovered 66 TNOs. They found a single power law apparent luminosity function for TNOs with R magnitudes between 22 and 25 of $\sum(< m_R) = 10^{0.76(m_R - 23.3)}$.

Fraser et al. (2008) expanded on the search for irregular satellites by searching 3 deg^2 of sky about Uranus and Neptune. They detected 72 objects (70 new) with a 50% limiting magnitude at $m \sim 26.4$. They fit the sample with a single power law luminosity function for $m_R = 21$ to 26 with a slope $\alpha = 0.65 \pm 0.05$ and $m_{R,0} = 23.42 \pm 0.13$. From the magnitude distribution, they extrapolated a corresponding size distribution using collision and accretion models.

Fuentes and Holman (2008) conducted an archival search of Subaru images originally taken to search for irregular satellites of Uranus. This search covers 2.8 deg^2 of sky down to a 50% limiting R magnitude of 25.69 ± 0.01. They detected 82 TNOs and 5 Centaurs (along with 5 irregular satellites). Their best-fit single power law has a slope $\alpha = 0.51^{+0.5}_{-0.6}$ and magnitude $m_{R,0} = 22.6^{+0.3}_{-0.4}$ while their best fit double power law has

slopes of $\alpha_1 = 0.7^{+0.2}_{-0.1}$ and $\alpha_2 = 0.3^{+0.2}_{-0.2}$ and a magnitude break at $R = 24.3^{+0.8}_{-0.1}$. However, the uncertainties in their fit leave much to be desired.

Fraser and Kavelaars (2009) conducted another Kuiper belt survey covering about 1/3 deg^2 of sky with a limiting magnitude of 50% at $m_R \sim 26.8$. They discovered 36 new TNOs and fit their sample combined with previous observations with a double power law distribution of $\alpha_1 = 0.75$ and $\alpha_2 \approx 0.2$ with a break magnitude between 24.1 and 25.3.

Kavelaars et al. (2009) just released data from the first year of the Canada-France Ecliptic Plane Survey (CFEPS) covering about 94 deg^2 of sky in which they detected 73 KBOs.

Schwamb et al. (2009) conducted a search for distant Sedna-like bodies. This bright magnitude search covered ~12,000 deg^2 of sky down to a limiting R magnitude of 21.3. They detected 53 KBOs and Centaurs (25 new) without finding any Sedna-like bodies. They estimate the existence of between 15 and 92 Sedna-sized objects in Sedna-like orbits compared to between 5 and 8 Sedna-sized objects in the Kuiper belt.

Kenyon and Bromley (2004) considered collision models to constrain the power law cumulative size distribution given by:

$$N_C \propto r^{-q} \tag{1.3}$$

for objects of radius r. They found $q \approx 3.5$ for large bodies and $q \approx 2.5$ - 3 for small bodies with a break radius $r_b \approx 1$ - 30 km (the radius at which the slope of the size distribution changes). Bulk material properties are constrained by the size distribution of small objects while formation conditions are constrained by the size distribution of large objects (Fraser et al. 2008).

In a different approach to KBO detection, Bianco et al. (2009b) conducted an occultation survey in an attempt to discover sub-km-sized KBOs passing in front of stars using the continuous readout mode of Megacam at the *Monolithic Mirror Telescope* (*MMT*; formerly the *Multiple Mirror Telescope*). In 220 star hours, no occultations were detected. This places an upper limit on the surface density of KBOs larger than 1 km of 2.0×10^8 deg^{-2} and on the surface density of KBOs larger than 0.7 km of 4.8×10^8 deg^{-2}. As part of the Taiwanese-American Occultation Survey (TAOS), approximately 1,260,000 star hours were observed over 3 years without detecting any occultations (Bianco et al. 2009a).

Olber's Paradox places a limit on the number distribution of KBOs in conjunction with those limits determined by discovery and occultation surveys. Olber's Paradox states that a night sky full of stars and galaxies should be very bright. There must be a reason why it is not. The observed background sky brightness constrains the size distribution in R for reflected light from KBOs such that the distribution seen for R magnitudes of between 20 and 26 cannot perpetuate down to R magnitudes of between 45 and 55 or the background sky brightness would be too large (Kenyon and Windhorst 2001). Similarly, in the far-infrared, the number of grains and KBOs emitting thermal radiation is limited by the observed sky brightness. Kenyon and Windhorst (2001) found that for particles with radii between 1 μm and 1 km, the number of particles, *n*, with radius, *r*, can be estimated with the following relation:

$$n(r) \propto r^{-\alpha} \tag{1.4}$$

where α is approximately less than or equal to 3.4.

1.3 General TNO Properties

1.3.1 By Dynamical Class

Kuiper belt objects reflect sunlight in visible wavelengths. The magnitude can be measured in different filters to determine color indices (B-V, B-R, V-R). Some objects will appear the same color as the Sun. These objects are referred to as having solar, neutral, or gray colors. Some objects appear bluer than the Sun because they have a surface compound that absorbs red light. Other objects appear redder than the Sun because they have a surface compound that absorbs blue and/or visual light. The spectral gradient is the slope of the spectrum given as a percentage per unit wavelength. Objects with larger gradients are redder. Since TNOs are relatively faint, not many visual spectra have been observed. Color indices, or colors, can at least provide points for comparison and a good approximation of the continuum slope when spectra are unavailable. Figure 1.4 shows the distribution of V-R with semimajor axis for those objects with published colors.

Santos-Sanz et al. (2009) found that the average spectral gradient differs by dynamical class as follows: 19.6 ± 8.5 %/100 nm for hot Classicals, 27.4 ± 11.3 %/100 nm for cold Classicals, 18.6 ± 7.6 %/100 nm for SDOs, and 19.8 ± 6.7 %/100 nm for Centaurs. Among other correlations, they confirm an anticorrelation between color and inclination and between color and eccentricity for Classicals (cold Classicals are red). Santos-Sanz et al. (2009) found that in general for visual wavelengths, TNOs have featureless spectra with approximately constant slopes. Santos-Sanz et al. (2009) also determined that, based on their sample, more than 55% of TNOs may have small to medium magnitude variations. They expect that smaller objects have been distorted more by collisions than

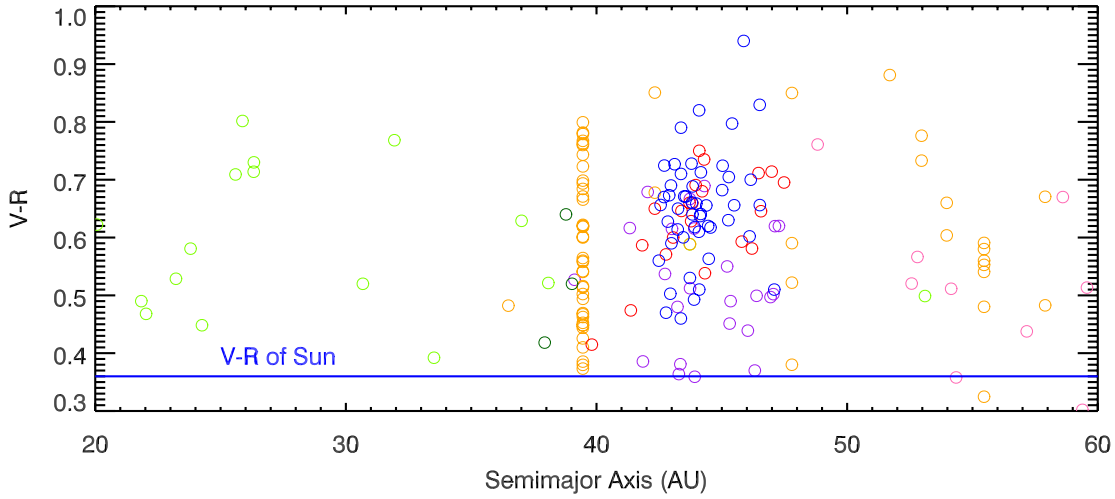

Figure 1.4. Plot of V-R color index with respect to semimajor axis for the majority of TNOs with well-defined orbits and published colors. Colors of symbols denote DES orbital types as in Figure 1.3. The blue line at V-R = 0.36 represents color of the Sun. Objects with V-R < 0.36 are blue. Objects with V-R > 0.36 are red. Note the accumulation of cold Classicals (blue symbols) near V-R = 0.65 illustrating that cold Classicals have red surfaces.

larger objects so their survey down to faint magnitudes would detect more objects with magnitude variations than other surveys.

Gulbis et al. (2006) found that Classical KBOs are red, Scattered-Near KBOs are gray, Scattered-Extended and 3:2 Resonant KBOs have a distribution of colors, 5:2 Resonant KBOs are gray, and other Resonant KBOs are red.

Jewitt et al. (2007) found that the U-B color index has the strongest correlation with the Tisserand parameter with respect to Neptune for Classical KBOs but not for non-Classicals. They also found that the U-B color is correlated with color indices B-V, V-R, R-I, and B-R but not absolute magnitude for Classicals and U-B is correlated with R-I for non-Classicals. Jewitt et al. (2007) found no evidence of a blue-absorbing mineral from the color indices of KBOs in their sample.

Romanishin et al. (2009) explored the colors of inner Classicals and found, unexpectedly, that they are not homogeneously red like cold Classicals. Inner Classicals

can be either red or gray. The color distribution for the 10 out of 19 inner Classicals measured is inconsistent to 99.9% probability with the color distribution of cold Classicals and is not inconsistent with the color distributions for Plutinos, Centaurs, and SDOs.

For KBOs of all classes combined, Peixinho et al. (2008) did not find a significant correlation between color and semimajor axis or between color and perihelion. They have reexamined the correlation between color and inclination for Classical KBOs and found that color appears homogeneously red for Classicals up to 12º to 13.5º in inclination instead of a color-inclination break between hot and cold Classicals at about 5º inclination.

Environmental effects may alter the surface color of KBOs. Radiolysis and photolysis can darken and redden surfaces which eventually become dark and neutral while ices below the surface may remain undamaged and if exposed may appear bright and neutral (Luu and Jewitt 1996, Strazzulla et al. 2003, Grundy et al. 2005).

Studies have implied that the red color observed among cold Classicals may be due to bulk composition instead of environmental effects. The red color of cold Classical KBOs is thought to derive from tholins (laboratory-produced complex compounds containing carbon, nitrogen, and hydrogen as solar system analogs for spectral features). However, tholins do not sublimate in the temperature range experienced by objects (Centaurs) traveling inward from the Kuiper belt (Grundy 2009). One possible explanation for a reduction in redness is the loss of water ice or other volatiles from a composite containing red tholins (Grundy 2009). According to Grundy (2009), water ice can enhance the observed redness of a TNO when part of a composite containing a red

complex compound. As the water ice sublimates, the redness decreases and the albedo also decreases.

Elliot et al. (2005) plotted an unbiased inclination distribution of the entire Kuiper belt in their Figure 20a and found that the distribution (including Resonant and Scattered KBOs) can be fit by the product of the sine of the inclination with the sum of two Gaussians of FWHM 4.57º ± 0.45º and 29.86º ± 1.51º. If one assumes that the bimodal distribution arises from the overlap of two distinct populations, then the probability of being in either population may be calculated for the low inclination region in which the Gaussians overlap. The Gaussian profiles intersect at about 5º which is the value for the population-inclination break adopted for this work. The Gaussian intersection would shift with the exclusion of Resonant and Scattered KBOs.

Barkume et al. (2008) surveyed the near-infrared spectra at low resolution of bright KBOs and found that when the Haumea collisional family is excluded from analysis, there is no clear trend in the fraction of water ice with color. They also did not find a correlation between water ice fraction and albedo or between water ice fraction and orbital elements.

Noll et al. (2008b) surveyed 101 Classical KBOs and found that the fraction of cold Classical KBOs that are binary is larger than the fraction of hot Classical KBOs that are binary. This may be due to different places of origin for the two populations. If the hot Classicals formed closer to the Sun than the cold Classicals, then they would experience more encounters with Neptune which may possibly affect binary companion retention. It remains to be seen if the different populations have experienced different amounts of collisional evolution.

Benecchi et al. (2009) found that for binary TNOs, the colors of the primary and the secondary are strongly correlated and are the same within measurement uncertainties. They find that the correlation between the color of the primary and the secondary is best explained by color from primordial composition and the early formation of binaries instead of being explained by color from environmental factors. The range of colors in their sample matches the range of colors seen among apparently single TNOs (binarity is not apparently correlated with color).

Of more than 1000 KBOs discovered so far, only one has been identified with a retrograde orbit (Gladman et al. 2009). Most surveys concentrate on the ecliptic plane, so it is not surprising that none have been discovered before. Gladman et al. (2009) suggest that, with the discovery of 2008 KV_{42}, there may possibly be a reservoir of objects with low perihelia and extremely high inclinations. 2008 KV_{42} and 2002 XU_{93}, with inclinations of 104º and 78º respectively, may be part of that reservoir which may be a source for Halley-type comets (Gladman et al. 2009). Other objects with extremely eccentric orbits are 2000 OO_{67}, 2006 SQ_{372}, 2000 CR_{105}, and Sedna.

1.3.2 By Size

The brighter objects (and thus larger) in the main Kuiper belt tend to have higher inclinations (Levison and Stern 2001) as seen below in Figure 1.5. The brightest hot Classical KBO in the figure below (red) has an absolute magnitude of 2.74 while the brightest cold Classical below (blue) only has an absolute magnitude of 5.18. The Scattered-Extended KBOs (purple) and the Scattered-Near KBOs (pink) have even higher inclinations. Their brightest members have absolute magnitudes of 0.00 and -1.15 respectively.

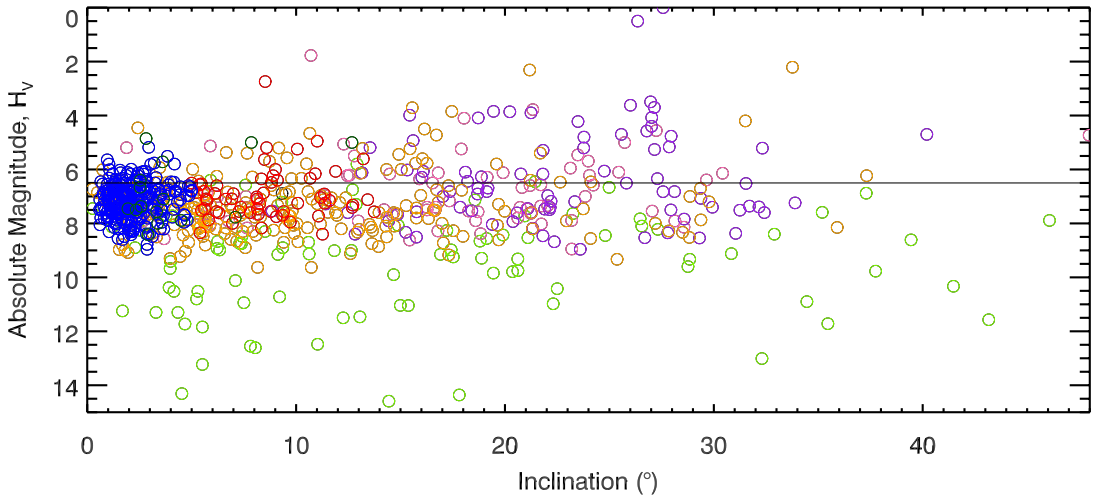

Figure 1.5. Plot of absolute magnitude with respect to inclination for the majority of TNOs with well-defined orbits. The horizontal line at magnitude 6.5 denotes the location of the break seen by Levison and Stern in 2001. Colors denote DES orbital types as in Figure 1.3.

Very large TNOs have enough self-gravity to maintain hydrostatic equilibrium, retain an increased amount of volatiles, have a differentiated internal structure, and possibly have atmospheres. Observations show that very large TNOs have high geometric albedos which may result from fresh icy grains and frost deposited on their surfaces during volatile outgassing and condensation (Lykawka and Mukai 2005). In general, small TNOs have much smaller albedos than very large TNOs, although I will

show that how much smaller depends on the object's orbital class. Size is not apparently correlated with color; however, appreciable differences are seen in near-infrared (NIR) spectra (Sheppard 2007). The compounds that remain on the surface that can be detected as NIR absorption features depend on the temperature, mass, and radius of the TNO.

Particles may escape a body through Jeans escape (like on Earth) or hydrodynamic escape (like on comets). The atmospheric structure of very large TNOs is not known nor is the fraction of escaping particles due to each escape method. However, the Jeans escape rate at the surface can be used as a reasonable lower limit on volatile loss rates (Schaller and Brown 2007a). Schaller and Brown (2007a) have calculated the minimum volatile loss of carbon monoxide, molecular nitrogen, and methane over the age of the solar system for KBOs as a function of radius and temperature. As expected, they find that most small KBOs have lost all their volatiles while Pluto, Triton, and Eris have retained volatiles of all three species. Quaoar, Haumea, and Makemake lie in the transition region where volatiles are mostly depleted (Schaller and Brown 2007a). These conclusions are supported by NIR spectra in which many small KBOs have featureless spectra or small water ice absorption features (Barkume et al. 2008). Quaoar, a moderately large KBO, has water ice and either ammonia or methane absorption features (see Chapter 5). For the very large TNOs, methane has been detected on Makemake; methane and possibly nitrogen have been detected on Eris; and methane, nitrogen, and carbon monoxide have been detected on Pluto (Schaller and Brown 2007a and references therein). Pluto currently is near perihelion and has an atmosphere. Eris, when it was closer to perihelion, most likely had an atmosphere that has now condensed into a uniform icy surface.

Brown et al. (2007) conducted a survey of NIR spectra of 30 KBOs. They found that (24835) 1995 SM_{55}, (19308) 1996 TO_{66}, (55636) 2002 TX_{300}, (120178) 2003 OP_{32}, (145453) 2005 RR_{43}, Haumea, and its satellite Hi'iaka have extremely large NIR water ice absorption features, neutral colors, and similar orbital elements. Of these, Haumea has an extremely fast rotation rate, a very elongated shape, a large density (2.7 g/cm^3; Schaller and Brown 2008), and a mass on the order of 100 times more massive than the others. Together, these objects form a collisional family with Haumea as the possible remnant of the progenitor and the other KBOs and Haumea's two satellites, Hi'iaka and Namaka, as possible remnants of the mantle of a differentiated body (Brown et al. 2007). Since many KBOs have neutral colors, NIR spectra are necessary to determine membership in the collisional family (Schaller and Brown 2008). Schaller and Brown (2008) observed 2003 UZ_{117}, 2005 CB_{79}, and (120347) 2004 SB_{60} which are dynamically close to the collisional family and found that the first two objects have the large water ice feature while the latter does not. They also note that Makemake is relatively dynamically close to the collisional family. The Haumea family is the only collisional family detected in the Kuiper belt as yet. Its components are much larger than asteroids in the approximately 35 main belt asteroid (MBA) collisional families (Morbidelli 2007). Morbidelli (2007) discusses the evolutionary implications of the Haumea family. For example, the tight orbital dispersion of its members places a narrow time constraint on the evolution of the Kuiper belt. The family-forming collision must occur early enough that there remains sufficient material near the proto-Haumea for the collision to have occurred yet late enough for Haumea to have already been dynamically excited with a low probability of further orbital perturbation from giant planets that would disperse the

remnant fragments after the collision. Also, the neutral colors of the remnant mantle fragments combined with the age of the collision suggest that red colors are not due to space weathering or accumulation of carbonaceous dust.

The ability of the large TNOs to retain more volatile ices than small TNOs should cause differences in linear polarization behavior. Bagnulo et al. (2008) found that the five small objects in their sample have negative polarizations that grow increasingly negative (from 0% to -1.5%) with increasing phase angle (from 0º to 2º) while Quaoar, a moderately large KBO, has a roughly constant negative polarization of -0.5% and Pluto, a very large KBO, has a roughly constant negative polarization of -0.3%. Eris, a very large KBO, also has a low negative polarization of -0.1% but their reported observations do not extend past 0.7º phase angle to support or contradict the apparent tendency of large TNOs to have constant linear polarization.

Planetary objects change apparent magnitude slightly when viewed from different phase angles. The slope of the phase curve at low phase angles is shallow for very large TNOs and steep for moderate-sized TNOs (Sheppard 2007). This is due to differences in the amount of coherent backscattering, shadow hiding, and regolith grain size.

The rotation rates of small TNOs are affected more by collisions and fragmentation than the rotation rates of large TNOs which should not have changed much since the formation of the Kuiper belt (Sheppard 2007). The rotation period and the amplitude of magnitude variations of an object can be used to constrain its density. An object that rotates with a period below its critical period (a function of density) will break apart. An object that rotates above but near its critical period will form a triaxial ellipsoid with a noticeably double-peaked amplitude unless viewed pole-on. An object that rotates

well above its critical period will form a Maclaurin spheroid without an obvious amplitude. Sheppard (2007) found that the mean period and amplitude of TNOs differs from that of MBAs. This is not surprising since TNOs are expected to be icier, less rocky, and thus less dense than MBAs. A trend in period or amplitude with radius for TNOs is not obvious from the data presented by Sheppard (2007). In addition, Eris has little to no variation in magnitude most likely due to global ice condensation or pole-on orientation.

1.4 Orbital Evolution Scenarios

As more TNOs have been discovered, knowledge of the dynamical structure of the region has evolved. Consequently, orbital evolutional models have evolved over time to explain newly discovered facets of the transneptunian region.

Transneptunian objects need to accrete from the planetesimal disk. Kenyon and Luu (1998) conducted accretion simulations to estimate the conditions necessary to form the objects found in the Kuiper belt *in situ*. They found that the timescale for runaway growth of planetesimal bodies depends on the initial mass of the proto-Kuiper belt annulus and on the initial velocity distribution and radii of the planetesimals. In order to produce a Pluto-sized object in the same amount of time that Neptune forms, the initial mass in a 6 AU planetesimal annulus centered about 35 AU should be from on the order of 10 Earth-masses to 100 Earth-masses. This estimate also agrees with observations of circumstellar disks about young stars available at the time (Kenyon and Luu 1998). The range of mass needed to form TNOs *in situ* is many orders of magnitude greater than the estimated current mass. Thus methods were devised for removing mass from the region or forming objects closer to the Sun and transporting them to their current positions.

In 1984, Fernandez and Ip showed that, when placed in a disk of planetesimals, the gas giants will migrate from the orbits in which they coalesced. Specifically, Jupiter will migrate inward and Saturn, Uranus, and Neptune will migrate outward. The planetesimals are scattered by the gas giants; angular momentum and energy are transferred between interacting bodies; and, as a result, the gas giants migrate.

After other Resonant KBOs besides Pluto were discovered, models needed to explain the capture of KBOs into Neptune's mean motion resonances (MMRs). During

Neptune's outward migration, its MMRs travel outward across the planetesimal disk, sweep up planetesimals from the disk, trap them, and carry them outward (Malhotra 1993, 1995).

Murray-Clay and Chiang (2006) conducted simulations that explore the role of stochasticity in Neptune's migration and the conditions necessary to retain Resonant objects. The outward orbital migration of a gas giant must be somewhat smooth in order to trap bodies in its MMRs. However, planetary migration cannot be completely smooth since it is caused by the discrete transfer of energy and angular momentum involved in the gravitational scattering of planetesimals. The migration of a large object is smoother when it scatters many small objects than when it scatters a few large objects. The smoothness of Neptune's actual migration is unknown; however, Murray-Clay and Chiang (2006) determined that the bulk of the planetesimal objects must have had sizes much smaller than on the order of 100 km and only a very small fraction of the mass must have been in objects larger than 1000 km in order to keep objects trapped in Neptune's MMRs. The small sizes of the bulk of planetesimal objects in their dynamical evolution model are consistent with the small sizes found for many of the objects in this work. Murray-Clay and Chiang (2006) conclude that the degree of stochasticity in Neptune's migration did not hinder its ability to capture and retain Resonant objects. In addition, they suggest that some cold Classical KBOs may be former low inclination 2:1 Resonant objects that have escaped or been released from the MMR.

Lykawka and Mukai (2007a) investigated the capture of objects in high-order resonances. They concluded that resonance sweeping was necessary for the long-term capture of objects from an excited disk near the current position of the Kuiper belt into

Neptune's 9:4, 5:2, and 8:3 MMRs. They ruled out the scattered disk as the source of long-term high order Resonant KBOs (high order resonances lay in the scattered disk region).

The population density of the Classical Kuiper belt drops off dramatically for semimajor axes greater than about 48 AU. According to Levison et al. (2004), one explanation for the outer edge of the main Kuiper belt is a close encounter with another star. If the edge is due to interactions with a passing star, it must have occurred while the Sun was still in its formation nebula when it was closer to other stars than it is now. Levison et al. (2004) determined that to satisfy observational constraints, a passing star would have to draw within about 200 AU before the formation of the Oort cloud. A star that close would strip away any material from the Oort cloud region and there must be enough time and material left in the planetesimal disk after the encounter to form the Oort cloud as it is observed today. From their simulations, Levison et al. (2004) determined that a passing star is not responsible for exciting the scattered disk to its current state; however, a passing star could excite subkilometer objects past the critical eccentricity of 0.06 at which point they may suffer a collisional cascade and grind each other to dust creating the observed outer edge of the disk. An encounter with a passing star may also account for the dramatically eccentric orbits of 148209 2000 CR_{105} (a = 223 AU, e = 0.800, i = 21.2º) and 90377 Sedna (a = 508 AU, e = 0.850, i = 10.7º) (Morbidelli and Levison 2004). In Figure 1.3, the sculpting of the Kuiper belt is evident by the dearth of low eccentricity objects with semimajor axes greater than 48 AU.

Ford and Chiang (2007) showed that more than two ice giants (Uranus and Neptune) could have formed in the region between 15 AU and 25 AU depending on the

surface density of the planetesimal disk and the amount of dynamical friction and viscous stirring within the disk. In their simulations, the resulting planetary systems were closest to conditions in the solar system when three ice giants formed (and the extra was ejected). However, the Kuiper belt population was not scattered enough under their conditions. They reproduce the solar system using a shear-dominated oligarchy in which the surface density of the planetesimal disk is less than the surface density of oligarchs (ice giants). Levison and Morbidelli (2007) used a disk surface density much greater than the surface density of oligarchs since oligarchs were rarely ejected in their simulations. Levison et al. (2008) used fictitious forces to precisely control the orbital evolution of Uranus and Neptune while populating the Kuiper belt. For both research groups, there are still details that need to be investigated further, CPU time allowing, before a consensus may be reached.

In the Nice model (Tsiganis et al. 2005), after nebulous gas in the circumstellar disk dissipated, the gas giants lay in a compact formation along with a primordial planetesimal disk extending from Neptune's initial position to about 30 AU to 35 AU (this edge halts the outward migration of Neptune). The planets scattered the planetesimals and transferred angular momentum causing the outer planets to drift outward and Jupiter to drift inward. When Jupiter and Saturn crossed their mutual 2:1 MMR, their eccentricities were kicked up. These excitations perturbed Uranus and Neptune so that they penetrated the planetesimal disk. Once they penetrated the disk, they scattered out most of the planetesimals. In their simulations, when Saturn encountered Uranus and/or Neptune, the observed semimajor axes, eccentricities, and inclinations of the gas giants were reproduced without losing regular satellites (Tsiganis

et al. 2005). The Late Heavy Bombardment, as observed in the Moon's cratering record, may be explained by the period of intense migration and scattering instigated by Neptune penetrating the planetesimal disk (Gomes et al. 2005). In the Nice model, the current location of the Kuiper belt is initially empty. In addition to explaining the halt of Neptune's migration, moving the primordial position of the planetesimal disk inward reduces the necessity for massively depleting the disk mass down to the current mass estimate (Levison and Morbidelli 2003). Levison et al. (2008) expanded upon the Nice model with simulations to populate the different TNO dynamical classes with a two phase migration. The cold KBOs arrive in place first from a region farther from Neptune than the hot Classicals, which starting closer to Neptune, interact with it more. Still, the fact that the outer edge of the Kuiper belt lies extremely close to the 2:1 MMR does support the transportation of objects via resonance sweeping (Gomes 2009). The clear differences between the hot and cold Classical populations imply that they had different origins before transport and probably different methods of transport (the hot Classicals being scattered out from closer to the Sun and the cold Classicals being pushed out from farther from the Sun; Levison and Morbidelli 2003, Levison et al. 2008). However, there is as yet no concrete explanation for why the hot and cold populations vary so much, particularly in color, as a function of primordial heliocentric distance.

The existence of a Kuiper belt was predicted long before the discovery of 1992 QB_1 (the first KBO discovered after Pluto). After its discovery, numerical orbital integrations showed that the Kuiper belt is the source of the Centaurs (Levison and Duncan 1997). Numerical simulations revealed that short period comets require a source population closer than the Oort cloud (Duncan et al. 1988). They showed that Centaurs

are the source of Jupiter family comets (JFCs) (the first Centaur, Chiron, was discovered in 1977). Since JFCs and Centaurs have short dynamical lifetimes, the Kuiper belt must be a current source for JFCs. In time, the Scattered Disk population of the Kuiper belt became accepted as the subpopulation source. Recent simulations by Volk and Malhotra (2008) show that the steady-state number of comet-sized SDOs necessary to supply the current observational estimate of JFCs is more than two orders of magnitude greater than the currently estimated number of comet-sized SDOs. One of their suggested possible solutions to the discrepancy is that other dynamical classes in the Kuiper belt, especially the Classical KBOs, in addition to SDOs may contribute to the JFCs.

Since JFCs originate in the Kuiper belt, valuable information on the composition, interior structure, tensile strength, and porosity of TNOs can be gained from observations and explorations of comets which are more easily accessible than TNOs.

1.5 Objective

Investigating the geometric albedos of TNOs is fascinating because space weathering can alter TNO surfaces from bright and neutral to darker and red and further to dark and neutral. In addition to this possible color-albedo ambiguity, there is a size-albedo ambiguity. For two objects of the same apparent visual magnitude and distance, one may be small and very reflective while the other may be large and not very reflective.

The geometric albedo is the ratio of a body's disk-integrated brightness at zero phase angle to the brightness of an equivalently-sized Lambertian disk with perpendicular illumination (Spencer 1987); that is, the ratio of the light reflected directly back towards the source to the light that would be reflected from an idealized, fully reflecting, flat, diffusely scattering disk of the same size. The bolometric Bond albedo is the ratio of the total reflected light to the total incident light for a surface (Spencer 1987).

The size of TNOs cannot be measured directly due to their small angular sizes when viewed from Earth. In addition, their thermal radiation peaks in the infrared at wavelengths that do not penetrate Earth's atmosphere. Thus to determine their radii and visual geometric albedos, it is necessary to model the flux measured with infrared space satellite observations. Accurate radii and albedos reduce the ambiguity in determining size-frequency distributions, densities, surface temperatures, escape velocities, and volatile loss rates and in interpreting composition from color photometry and spectra. The details we can glean about TNOs will tell us more about the formation and evolution of the solar system. What we learn about our solar system can be expanded to apply to T Tauri stars surrounded by protoplanetary disks and to main sequence stars with debris disks.

The goal of this research is to determine the radii and visual geometric albedos of Classical Kuiper belt objects (KBOs) and test the hypothesis that dynamically hot and cold Classical KBO populations have different albedo distributions. I will to determine if there exists a correlation between albedo and inclination. If the two populations do have different albedo distributions, then they are more likely to have formed in different distinct regions of the primordial disk and/or undergone different methods of transport to evolve dynamically into their current orbits. This is interesting because they have such similar orbits that it would be logical to assume that they are all drawn from a single parent population.

Preliminary analysis of thermal modeling showed that there is indeed a correlation between albedo and inclination for Classical KBOs. Therefore, a second campaign was begun to explore the boundaries of the cold Classical population. The second campaign was to determine if the cold Classical population was deposited from resonance zones as Neptune migrated outward by observing low inclination 2:1 Resonant and 3:2 Resonant KBOs. If current Resonant KBOs with low inclinations have high albedos similar to cold Classicals, then this transport scenario will hold.

Chapter 2

Facility and Observations

2.1 Facility

Infrared photometric images for this project were taken using the *Spitzer Space Telescope* (*SST*) which is an infrared observatory formerly named the *Space Infrared Telescope Facility* (*SIRTF*). It was launched in August 2003 as part of NASA's Great Observatories Program and named after astrophysicist Lyman Spitzer, Jr. The primary mirror of *SST* has a diameter of 0.85 m and its cryogenically cooled instruments covered wavelengths from 3 to 180 μm.

The science instrument used was the Multiband Imaging Photometer for *Spitzer* (MIPS) which had imaging bands at 24 μm, 70 μm, and 160 μm and a low resolution spectrometer at 70 μm. A detailed description of the instrument is given by Heim et al. (1998) and a general description is given by Rieke et al. (2004). We employed the 24 μm and 70 μm MIPS imaging bands to best sample the thermal emissions of the target TNOs. Objects in this region of the outer solar system have temperatures between 40 K and 70 K. A blackbody within this temperature range should have a peak wavelength between 72 μm and 41 μm according to Wien's Law. The MIPS bandwidths are illustrated in Figure 2.1 with blackbody radiation curves at TNO temperatures. The 24 μm band had a diffraction-limited resolution of 6 arcsec full width at half maximum (FWHM) and a bandwidth of about 5 μm. The 70 μm band had a diffraction-limited resolution of 18 arcsec FWHM and a bandwidth of about 19 μm (Rieke et al. 2004). One half of the 70 μm array plus a corner of the other half of the array were nonfunctional due to cable

failures. According to Rieke et al. (2004), the 5 σ detection limits for 500 s integrations of point sources under optimal conditions were 0.11 mJy, 6 mJy, and 15 mJy for the 24 μm, 70 μm, and 160 μm imaging bands respectively. This is an improvement by a factor of about 1.5 on the prelaunch sensitivity estimate at 24 μm for the silicon-arsenic impurity band conduction detectors (Rieke et al. 2004). The 70 μm and 160 μm germanium photoconductors are detectors made from germanium-gallium arrays. Their sensitivities were about a factor of three worse than prelaunch estimates due to an underestimated rate of large cosmic-ray hits (Rieke et al. 2004). The low sensitivity of the 70 μm imaging band adversely affected our observations resulting in the nondetection of several objects.

2.2 Observing Team

The proposal for observing time was submitted by Dr. William M. Grundy (Lowell Observatory), Dr. Marc W. Buie (formerly of Lowell Observatory), Dr. Eugene I. Chiang (University of California, Berkeley), Dr. Dale P. Cruikshank (NASA Ames Research Center), Dr. Robert L. Millis (Lowell Observatory), Dr. John R. Spencer (Southwest Research Institute, Boulder), Dr. John A. Stansberry (University of Arizona, Steward Observatory) and Dr. Lawrence H. Wasserman (Lowell Observatory). Dr. Buie has since moved to Southwest Research Institute, Boulder, and Dr. Millis has retired.

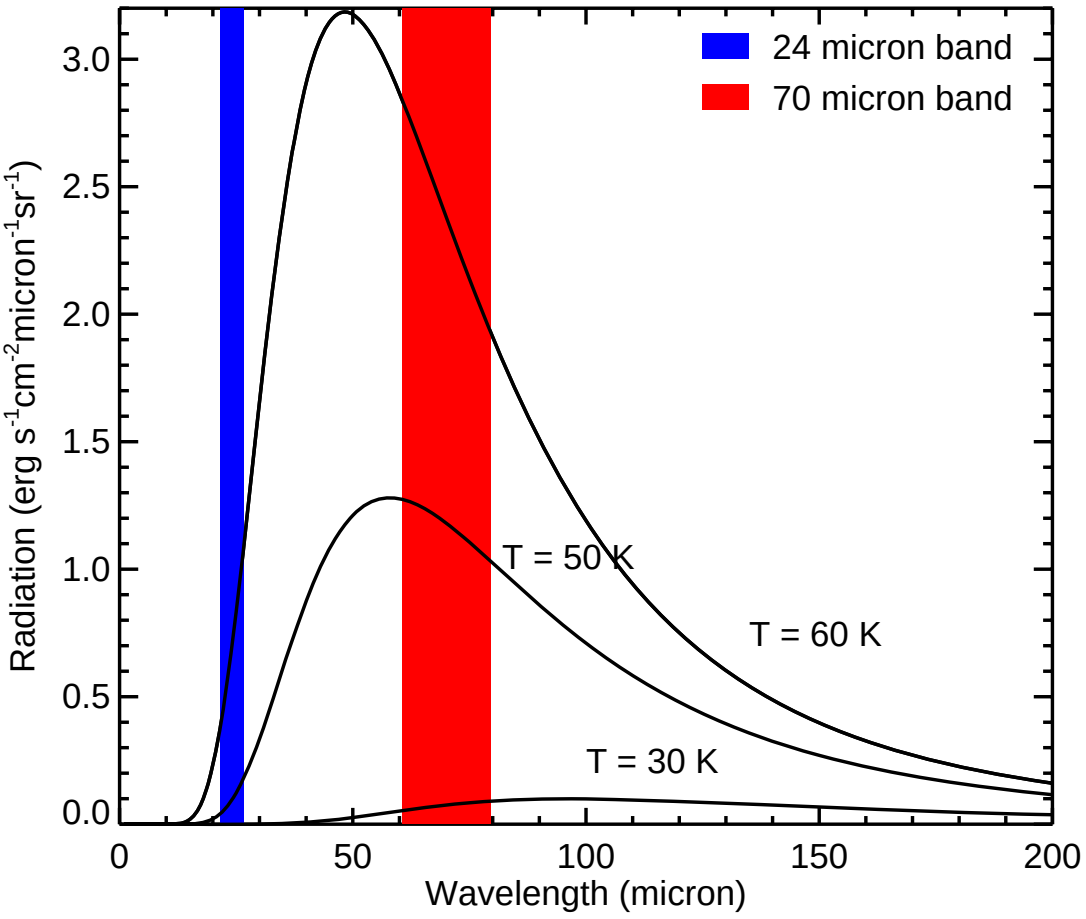

Figure 2.1. Blackbody radiation curves for objects at expected temperatures of TNOs: 30 K, 50 K, and 60 K overlaid by the MIPS/*SST* 24 μm and 70 μm imaging bands.

2.3 Program P3542 Observations

The observations were made as part of program P3542 in *SST* cycle one. Although *SST*'s observing cycle 1 ran from July 1, 2004 to May 31, 2005, the observations for P3542 continued from November 2, 2004 through April 7, 2006. The goals of this campaign were to determine accurately the radii and albedos of the target objects and to determine if there is a trend in albedo with inclination in the Classical Kuiper belt (to search for differences between dynamically hot and cold Classical KBOs).

With these goals in mind, my analysis will focus on objects that are considered to be Classicals under either of the two main classification systems. We observed sixteen of twenty TNOs requested with *SST*/MIPS. The four unobserved objects were the hot Classical (79983) 1999 DF_9, the hot Classical (DES Scattered-Near) (168703) 2000 GP_{183}, the cold Classical 2000 OU_{69}, and the 3:2 Resonant 2002 VU_{130}. The images for the cold Classical object 2001 QB_{298} were not analyzed due to a pointing error in which the target fell off the edge of the detector in the 70 μm images. The remaining fifteen objects include thirteen Classical KBOs. 2001 QT_{322} and 2002 KX_{14} are dynamically cold inner Classicals (having orbital inclinations less than 5˚ and semimajor axes less than 39.5 AU). 2002 VT_{130}, 2001 QD_{298}, 2001 RZ_{143}, and 2001 QS_{322} are dynamically cold main belt Classicals. 2000 OK_{67} lies within the transition zone for cold and hot Classicals and we arbitrarily place it in the cold category since its mean inclination is 4.9999˚. 2001 KA_{77}, 2002 GJ_{32}, 1996 TS_{66}, Quaoar, and Altjira are dynamically hot main belt Classicals (inclinations greater than 5˚). 2002 KW_{14} is a hot Classical according to Gladman et al. (2008) but a Scattered-Extended KBO according to the DES classification system (Elliot et al. 2005). Two of the fifteen objects are not Classical KBOs: 2001 QR_{322} and 2003 QX_{111}. 2001 QR_{322} is a Neptune Trojan and was chosen as a verification tool since it lies closer to the Earth and thus has a stronger signal (easier to detect) than most of our other objects. Also, it was previously thought to have a similar dynamical history to Classical KBOs (all being formed *in situ*). 2001 QX_{111} was chosen before its orbit was well-determined. Originally it was thought to be a Classical KBO but a better constrained orbit showed that it is a 3:2 Resonant KBO. Orbital properties for all fifteen objects may be found in Table 2.1 (Brucker et al. 2009, Table 1.). Figure 2.2

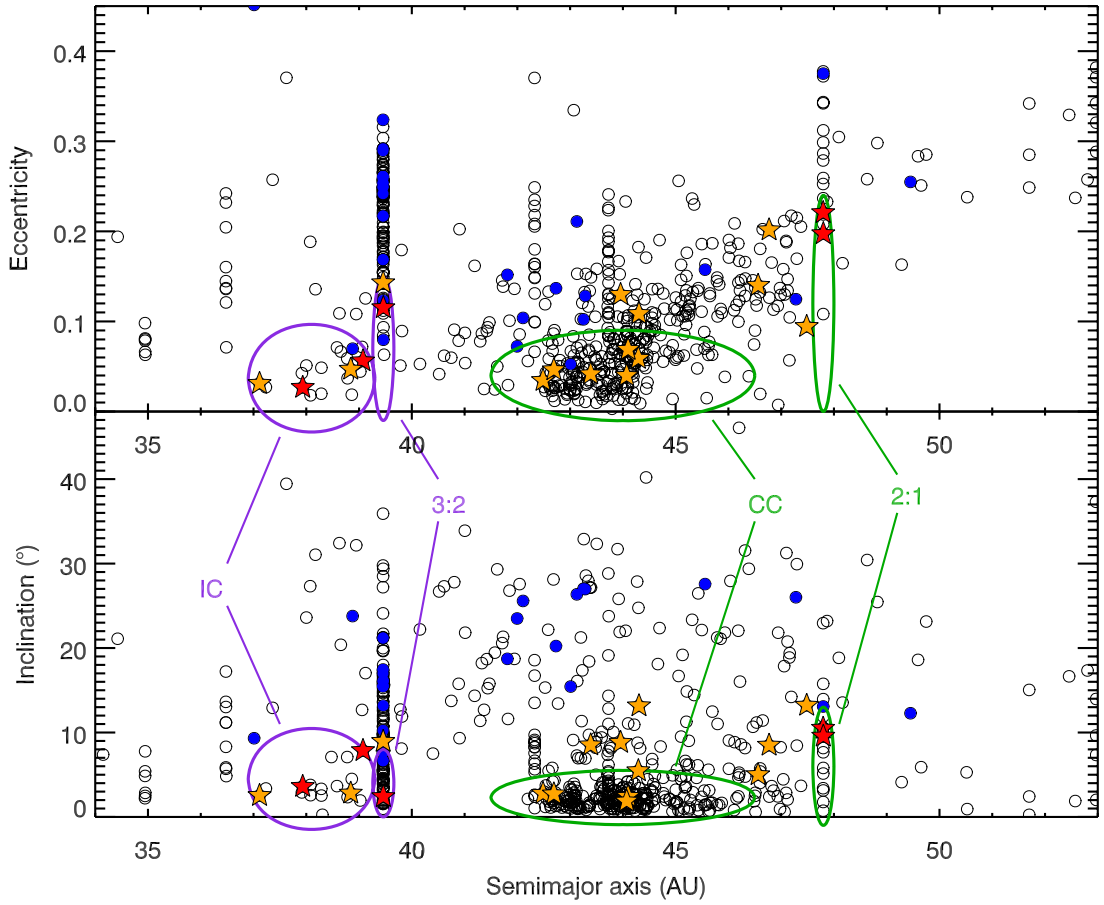

Figure 2.2. The eccentricities and inclinations versus the semimajor axes are plotted for TNOs with defined orbital classifications. Objects observed in P3542 are denoted with orange stars and objects proposed for P50540 are denoted with red stars. Objects previously observed with *SST* are denoted with blue filled circles. The purple circles highlight the regions containing inner Classicals and low inclination 3:2 Resonant KBOs. The green circles highlight the regions containing cold main belt Classicals and low inclination 2:1 Resonant KBOs.

illustrates how the semimajor axes, inclinations, and eccentricities of the successfully observed targets in P3542 relate to other TNOs.

Four or more observations of each object were conducted. Each observation is specified by an astronomical observation request (AOR) and designated by a numerical code (AORkey). As described by Brucker et al. (2009),

> Each AOR consisted of many short exposures or data collection events (DCEs) executed with dithering of the field of view (FOV). The DCEs were each 10 MIPS seconds long (about 10.49 s). The AORs were timed

> such that the target object had moved more than the width of a point-spread function (PSF) but less than the width of the FOV in between each visit in order to improve background subtraction. With this method, unlike shadow observations, no empty fields are observed. The position of the target object on the mosaic image was also dithered among the AORs in later observations.

John Stansberry, as a member of the MIPS instrument team, used the MIPS data analysis tools (Gordon et al. 2005) and other additional tools to process the DCEs and remove instrumental artifacts. He produced a final calibrated mosaic image from the DCEs for each visit in each wavelength band. Details of this processing can be found in Stansberry et al. (2008). The details of the AORs may be found in Tables 2.2 and 2.3 where the objects' provisional designations, image AORkeys, Modified Julian dates of observations, right ascensions, declinations, distances from the Sun, distances from *SST*, phase angles (the Sun-object-observer angle), exposure times, and rejection statuses are delineated. The individual 24 μm mosaic images cover a FOV of 7.53'x8.32' at a scale of 1.245 arcsec/pixel. The 70 μm mosaics cover a FOV of 2.96'x7.31' at a scale of 4.925 arcsec/pixel. If an asteroid passed through the target pathway (Figure 2.3), then the 24 μm mosaic image containing the asteroid was rejected. Other 24 μm images were rejected for poor background subtraction (Figure 2.4). None of the 70 μm images were rejected since sources could not be differentiated from the background noise in most cases. The instrumental artifacts as seen in Figure 2.3 never crossed target pathways and thus were ignored in all images in which they occurred.

Table 2.1 Orbital Properties of *Spitzer Space Telescope* Cycle 1 Program P3542 Targets
(Brucker et al. 2009 Table 1)

Provisional Designation[a]	a (AU)[b]	e[b]	i (°)[b,c]	T_N[r]	H_V[d]	V-R	DES Type[e]	Name and Number
Hot Classicals								
2001 KA_{77}	47.4830	0.0944	13.2174	3.07	5.608 ± 0.042[f,g]	0.695 ± 0.081[f,g,h]	C	
2002 GJ_{32}	44.2771	0.1061	13.1642	3.03	6.12 ± 0.13[g]	0.68 ± 0.08[g]	C	182934
1996 TS_{66}	43.9628	0.1298	8.8280	3.05	6.48 ± 0.16[i]	0.690 ± 0.048[j]	C	
2002 LM_{60}	43.3887	0.0417	8.5214	3.07	2.739 ± 0.011[k,l]	0.646 ± 0.012[k,l]	C	Quaoar 50000
2002 KW_{14}	46.7707	0.2016	8.4874	3.06	5.959 ± 0.060[m]	0.72 ± 0.07[m]	SE	
2001 UQ_{18}	44.3018	0.0581	5.4610	3.09	6.55 ± 0.21[g]	0.735 ± 0.078[g]	C	Altjira 148780
Cold Classicals								
2000 OK_{67}	46.5638	0.1401	4.9999	3.10	6.50 ± 0.10[f,n,o]	0.653 ± 0.048[f,n,o]	C	138537
2002 VT_{130}	42.4930	0.0334	2.7921	3.08	5.95 ± 0.5	--	C	
2001 QD_{298}	42.6911	0.0449	2.7769	3.08	6.68 ± 0.08[g]	0.67 ± 0.09[g]	C	
2001 RZ_{143}	44.0958	0.0687	2.4295	3.10	6.23 ± 0.5	--	C	
2001 QS_{322}	44.0890	0.0398	1.8803	3.10	6.22 ± 0.5	--	C	
Inner Classicals								
2001 QT_{322}	37.1091	0.0319	2.5185	3.03	6.4 ± 0.5	0.53 ± 0.12[p]	C	135182
2002 KX_{14}	38.8406	0.0469	2.8165	3.04	4.89 ±0.03[m,q]	0.621 ± 0.022[m,q]	C	119951
Resonant KBOs								
2001 QR_{322}	30.1106	0.0311	1.2645	3.00	8.11 ± 0.02[m]	0.46 ± 0.02[m]	1:1	
2003 QX_{111}	39.4566	0.1553	8.3295	3.00	6.76 ± 0.5	--	3:2	

[a]Objects are sorted by Gladman et al. (2008) orbital type and decreasing inclination with a break at 5° to separate the overlapping hot and cold Classical KBO populations.
[b]Values averaged over 10 Myr orbital integrations.
[c]Average inclinations are with respect to the invariable plane.
[d]Where published V magnitudes were available (as indicated by notes f-q), Hv was estimated by combining V magnitudes weighted according to their error bars, assuming G=0.15 in the Bowell et al. (1989) photometric system. The larger of the formal error and the scatter of the individual measurements was taken as the uncertainty. For the remaining objects with no published photometry, Hv was taken as a straight average of the crude photometry reported with the astrometric observations used to compute each object's orbit, subject to assumed colors and G=0.15 phase behavior. According to Romanishin and Tegler (2005), this procedure tends to overestimate the absolute brightness by about 0.3 mag, so we added 0.3 to the value and used conservative half-magnitude error bars. The linear phase function method of Sheppard and Jewitt (2002) produces similar absolute magnitudes thus the method used will not change the results.

[e]DES orbital type (Elliot et al. 2005): SE - Scattered-Extended, C - Classical, #:# - Resonant.
[f]Doressoundiram et al. (2002).
[g]Doressoundiram et al. (2005).
[h]Peixinho et al. (2004).
[i]Davies et al. (2000).
[j]Jewitt and Luu (2001).
[k]Fornasier et al. (2004).
[l]Tegler et al. (2003).
[m]The objects 2002 KW_{14}, 2002 KX_{14} and 2001 QR_{322} were observed in the V and R bands by S. Sheppard with filters based on the Johnson system. 2002 KW_{14} and 2002 KX_{14} were observed with four 300 s images in each filter for each object at the du Pont 2.5 m telescope on UT July 19, 2007 with the Tek5 CCD (0.259" $pixel^{-1}$). 2001 QR_{322} was observed with four 350 s images in each filter on the Magellan 6.5 m Clay telescope on UT Nov. 3, 2005 with the LDSS3 CCD (0.189" $pixel^{-1}$).
[n]Delsanti et al. (2001).
[o]Stephens et al. (2003).
[p]Stephen Tegler, personal communication, 2007.
[q]Romanishin et al. (2009).
[r]T_N is the Tisserand parameter with respect to Neptune where a_N is the semimajor axis of Neptune. T_N is a constant of the motion for a three-body problem. Objects with $T_N < 3$ are likely to be dynamically coupled to Neptune (Jewitt et al. 2007).

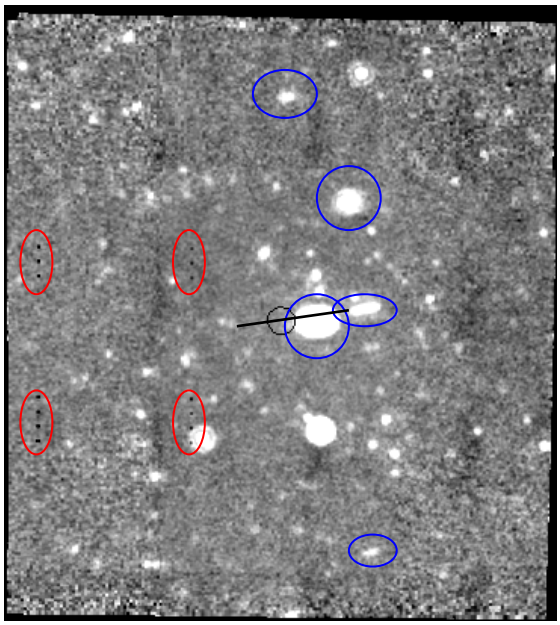

Figure 2.3. 24 μm image of (182934) 2002 GJ_{32} rejected for asteroids (AORkey 15482880). The black circle marks the target position, the black line marks the approximate target pathway, blue ovals mark asteroids (two are in the target pathway), and red ovals mark instrumental artifacts that were ignored.

Table 2.2 P3542 24 μm Observations

Object	AORKEY	MJD	RA (h)	Dec (˚)	r (AU)	Δ (AU)	α (˚)	t[a] (s)	Status[b]
2002 KW_{14}	15472128	53615.197	15.541	-18.589	40.045	40.090	1.464	374.22	
	15472896	53614.651	15.540	-18.587	40.045	40.081	1.464	374.22	
	15473664	53613.397	15.540	-18.584	40.045	40.059	1.465	374.22	
	15474176	53612.543	15.540	-18.582	40.044	40.045	1.466	374.22	
	15474688	53611.795	15.540	-18.580	40.044	40.032	1.466	374.22	
	15475200	53610.891	15.539	-18.578	40.043	40.016	1.466	374.22	
	15475712	53610.078	15.539	-18.576	40.043	40.002	1.465	374.22	
	15476224	53609.208	15.539	-18.574	40.043	39.987	1.464	374.22	
	15476736	53608.605	15.539	-18.573	40.042	39.977	1.463	374.22	
2001 KA_{77}	15466752	53832.511	16.893	-19.574	48.556	48.295	1.149	1496.9	
	15467008	53831.942	16.893	-19.575	48.556	48.304	1.152	1496.9	
	15476992	53831.049	16.893	-19.577	48.556	48.319	1.156	1496.9	
	15477504	53830.510	16.894	-19.578	48.556	48.329	1.158	1496.9	
	15477760	53829.989	16.894	-19.580	48.556	48.337	1.160	1496.9	
	15478016	53829.007	16.894	-19.582	48.556	48.354	1.164	1496.9	
	15478272	53828.469	16.894	-19.583	48.556	48.363	1.166	1496.9	
	15478528	53827.615	16.894	-19.584	48.557	48.378	1.169	1496.9	
	15478784	53826.964	16.894	-19.586	48.557	48.389	1.171	1496.9	
	15479040	53826.634	16.894	-19.586	48.557	48.395	1.172	1496.9	
	15479296	53825.636	16.894	-19.588	48.557	48.412	1.175	1496.9	
2002 GJ_{32}	15481856	53789.163	14.660	-20.245	43.154	43.101	1.332	1247.4	
	15482368	53787.398	14.659	-20.242	43.153	43.131	1.333	1247.4	
	15483136	53784.881	14.659	-20.238	43.153	43.173	1.332	1247.4	
	15483392	53784.091	14.659	-20.236	43.152	43.187	1.331	1247.4	
	15483648	53783.218	14.658	-20.234	43.152	43.201	1.330	1247.4	
	15483904	53782.588	14.658	-20.233	43.152	43.212	1.329	1247.4	
	15482112	53788.334	14.660	-20.244	43.154	43.115	1.332	1247.4	Rejected
	15482624	53786.763	14.659	-20.241	43.153	43.142	1.333	1247.4	Rejected
	15482880	53785.721	14.659	-20.239	43.153	43.159	1.332	1247.4	Rejected
1996 TS_{66}	11096320	53396.644	2.874	23.010	38.529	38.161	1.392	997.92	
	11096576	53397.865	2.874	23.005	38.529	38.180	1.403	997.92	
	11096832	53399.139	2.874	23.001	38.528	38.201	1.413	997.92	
	11097088	53400.328	2.873	22.997	38.528	38.220	1.423	997.92	
	11097344	53401.814	2.873	22.992	38.528	38.244	1.433	997.92	
	11097600	53402.731	2.873	22.989	38.528	38.259	1.440	997.92	

Table 2.2 P3542 24 μm Observations, cont'd.

Object	AORKEY	MJD	RA (h)	Dec (°)	r (AU)	Δ (AU)	α (°)	t[a] (s)	Status[b]
Quaoar	15475968	53832.498	17.066	-15.406	43.311	43.086	1.299	249.48	
	15476480	53831.929	17.066	-15.408	43.311	43.096	1.302	249.48	
	15477248	53831.097	17.066	-15.411	43.311	43.110	1.305	249.48	
	15479552	53830.537	17.066	-15.413	43.312	43.119	1.308	249.48	
	15479808	53830.037	17.066	-15.415	43.312	43.127	1.310	249.48	
	15480064	53829.506	17.066	-15.417	43.312	43.136	1.311	249.48	
	15480320	53828.517	17.066	-15.420	43.312	43.153	1.315	249.48	
	15480576	53827.930	17.066	-15.422	43.312	43.163	1.316	249.48	
	15480832	53827.230	17.066	-15.424	43.312	43.175	1.318	249.48	
	15481088	53826.615	17.066	-15.426	43.312	43.185	1.320	249.48	
	15481344	53826.038	17.066	-15.428	43.312	43.195	1.321	249.48	
	15481600	53825.623	17.066	-15.430	43.312	43.202	1.322	249.48	
2001 UQ_{18}	15465472	53789.270	3.555	23.639	45.333	45.141	1.245	1496.9	
	15465728	53788.453	3.555	23.640	45.333	45.127	1.241	1496.9	
	15467264	53787.842	3.555	23.641	45.333	45.117	1.239	1496.9	
	15467520	53787.248	3.555	23.641	45.333	45.106	1.236	1496.9	
	15467776	53786.583	3.555	23.642	45.333	45.095	1.233	1496.9	
	15468032	53785.779	3.555	23.643	45.333	45.082	1.229	1496.9	
	15468544	53785.168	3.555	23.644	45.333	45.071	1.225	1496.9	
	15469056	53784.483	3.555	23.645	45.332	45.060	1.222	1496.9	
	15469568	53783.916	3.555	23.646	45.332	45.050	1.218	1496.9	
	15470080	53783.154	3.555	23.648	45.332	45.038	1.214	1496.9	
	15470592	53782.483	3.555	23.649	45.332	45.027	1.209	1496.9	
2000 OK_{67}	11112192	53313.585	22.523	-11.822	40.575	40.068	1.250	873.18	
	11112448	53315.652	22.522	-11.826	40.575	40.099	1.274	873.18	
	11112704	53317.819	22.521	-11.828	40.574	40.132	1.297	873.18	
	11112960	53319.629	22.520	-11.830	40.574	40.160	1.314	873.18	
2002 VT_{130}	15466240	53789.221	4.035	21.872	42.751	42.453	1.286	1496.9	
	15466496	53788.529	4.035	21.872	42.751	42.442	1.281	1496.9	
	15470848	53787.891	4.035	21.873	42.751	42.431	1.276	1496.9	
	15471360	53787.275	4.035	21.873	42.751	42.421	1.272	1496.9	
	15471872	53786.796	4.036	21.874	42.751	42.413	1.268	1496.9	
	15474432	53783.969	4.036	21.876	42.75	42.367	1.245	1496.9	
	15474944	53783.182	4.037	21.877	42.75	42.355	1.238	1496.9	
	15475456	53782.532	4.037	21.878	42.75	42.344	1.232	1496.9	
	15472640	53785.859	4.036	21.874	42.751	42.398	1.261	1496.9	Rejected
	15473408	53785.216	4.036	21.875	42.751	42.388	1.256	1496.9	Rejected
	15473920	53784.511	4.036	21.876	42.75	42.376	1.250	1496.9	Rejected

Table 2.2 P3542 24 μm Observations, cont'd.

Object	AORKEY	MJD	RA (h)	Dec (˚)	r (AU)	Δ (AU)	α (˚)	t[a] (s)	Status[b]
2001 QD_{298}	11104000	53311.954	21.795	-18.498	41.185	40.851	1.341	997.92	
	11104256	53314.004	21.794	-18.497	41.185	40.884	1.355	997.92	
	11104512	53316.126	21.794	-18.495	41.185	40.919	1.368	997.92	
	11104768	53318.131	21.793	-18.493	41.185	40.953	1.379	997.92	
2001 RZ_{143}	11107072	53365.364	1.324	8.942	41.376	40.927	1.253	997.92	
	11107328	53367.583	1.323	8.938	41.376	40.962	1.275	997.92	
	11107584	53369.410	1.323	8.935	41.376	40.991	1.292	997.92	
	11107840	53371.412	1.322	8.932	41.376	41.023	1.309	997.92	
2001 QS_{322}	15465984	53711.336	23.559	-2.865	42.345	41.943	1.263	1247.4	
	15468800	53709.940	23.559	-2.862	42.345	41.921	1.250	1247.4	
	15469824	53708.294	23.560	-2.858	42.345	41.895	1.234	1247.4	
	15470336	53707.609	23.560	-2.857	42.345	41.885	1.227	1247.4	
	15471104	53706.785	23.560	-2.854	42.345	41.872	1.219	1247.4	
	15471616	53706.095	23.560	-2.853	42.345	41.862	1.211	1247.4	
	15472384	53705.355	23.561	-2.851	42.345	41.850	1.203	1247.4	
	15468288	53710.605	23.559	-2.863	42.345	41.931	1.256	1247.4	Rejected
	15469312	53709.105	23.559	-2.860	42.345	41.908	1.242	1247.4	Rejected
	15473152	53704.699	23.561	-2.849	42.345	41.841	1.196	1247.4	Rejected
2001 QT_{322}	11093248	53363.190	23.644	-0.848	36.921	36.890	1.564	623.7	
	11093504	53364.599	23.645	-0.846	36.921	36.914	1.564	623.7	
	11093760	53365.520	23.645	-0.844	36.921	36.930	1.563	623.7	
	11094016	53367.183	23.645	-0.841	36.921	36.958	1.561	623.7	
	11094272	53368.638	23.646	-0.838	36.921	36.983	1.559	623.7	
	11094528	53369.706	23.646	-0.835	36.921	37.001	1.556	623.7	
2002 KX_{14}	15463168	53615.177	15.749	-20.126	39.607	39.594	1.482	374.22	
	15463424	53614.662	15.748	-20.126	39.607	39.585	1.482	374.22	
	15463680	53613.428	15.748	-20.124	39.607	39.565	1.481	374.22	
	15463936	53612.553	15.748	-20.123	39.607	39.550	1.480	374.22	
	15464192	53611.756	15.748	-20.123	39.607	39.537	1.479	374.22	
	15464448	53610.902	15.748	-20.122	39.607	39.522	1.478	374.22	
	15464704	53610.385	15.748	-20.122	39.607	39.514	1.477	374.22	
	15465216	53608.636	15.747	-20.120	39.607	39.485	1.473	374.22	
	15464960	53609.221	15.748	-20.121	39.607	39.494	1.474	374.22	Rejected
2001 QR_{322}	11090176	53364.977	0.180	0.350	29.708	29.567	1.928	249.48	
	11090432	53367.358	0.180	0.355	29.709	29.608	1.936	249.48	
	11090688	53369.365	0.181	0.360	29.709	29.642	1.939	249.48	
	11090944	53371.367	0.182	0.365	29.709	29.676	1.941	249.48	

Table 2.2 P3542 24 μm Observations, cont'd.

Object	AORKEY	MJD	RA (h)	Dec (˚)	r (AU)	Δ (AU)	α (˚)	t[a] (s)	Status[b]
2003 QX_{111}	11099392	53362.707	23.851	-4.599	39.485	39.424	1.461	873.18	
	11099904	53365.228	23.851	-4.593	39.486	39.468	1.462	873.18	
	11100160	53367.233	23.851	-4.587	39.487	39.503	1.461	873.18	
	11100416	53368.174	23.852	-4.584	39.487	39.519	1.460	873.18	
	11100672	53368.934	23.852	-4.582	39.488	39.533	1.459	873.18	
	11099648	53364.161	23.851	-4.596	39.486	39.449	1.462	873.18	Rejected

[a]Total integrated exposure time.
[b]AORs discarded due to asteroids or improper background.

Table 2.3 P3542 70 μm Observations

Object	AORKEY	MJD	RA (h)	Dec (˚)	r (AU)	Δ (AU)	α (˚)	t[a] (s)
2002 KW_{14}	15472128	53615.203	15.541	-18.589	40.045	40.091	1.464	1017.5
	15473664	53613.403	15.540	-18.584	40.045	40.060	1.465	1017.5
	15474688	53611.801	15.540	-18.580	40.044	40.032	1.466	1017.5
	15475712	53610.084	15.539	-18.576	40.043	40.002	1.465	1017.5
	15476736	53608.611	15.539	-18.573	40.042	39.977	1.463	1017.5
2001 KA_{77}	15466752	53832.534	16.893	-19.574	48.556	48.294	1.149	1017.5
	15476992	53831.072	16.893	-19.577	48.556	48.319	1.156	1017.5
	15477760	53830.012	16.894	-19.579	48.556	48.337	1.160	1017.5
	15478272	53828.492	16.894	-19.583	48.556	48.363	1.166	1017.5
	15478784	53826.987	16.894	-19.586	48.557	48.389	1.171	1017.5
	15479296	53825.659	16.894	-19.588	48.557	48.412	1.174	1017.5
2002 GJ_{32}	15481856	53789.183	14.660	-20.245	43.154	43.101	1.332	1017.5
	15482368	53787.418	14.659	-20.242	43.153	43.130	1.333	1017.5
	15482880	53785.741	14.659	-20.239	43.153	43.159	1.332	1017.5
	15483392	53784.111	14.659	-20.236	43.153	43.186	1.331	1017.5
	15483904	53782.608	14.658	-20.233	43.152	43.212	1.329	1017.5
1996 TS_{66}	11096320	53396.660	2.874	23.009	38.529	38.161	1.392	1688.9
	11096576	53397.881	2.874	23.005	38.529	38.180	1.403	1688.9
	11096832	53399.155	2.874	23.001	38.528	38.201	1.414	1688.9
	11097088	53400.343	2.873	22.997	38.528	38.220	1.423	1688.9
	11097344	53401.830	2.873	22.992	38.528	38.245	1.433	1688.9
	11097600	53402.746	2.873	22.989	38.528	38.260	1.440	1688.9

Table 2.3 P3542 70 μm Observations, cont'd.

Object	AORKEY	MJD	RA (h)	Dec (˚)	r (AU)	Δ (AU)	α (˚)	t[a] (s)
Quaoar	15475968	53832.502	17.066	-15.406	43.311	43.086	1.299	178.33
	15476480	53831.933	17.066	-15.408	43.311	43.096	1.302	178.33
	15477248	53831.102	17.066	-15.411	43.311	43.110	1.305	178.33
	15479552	53830.542	17.066	-15.413	43.312	43.119	1.308	178.33
	15479808	53830.042	17.066	-15.415	43.312	43.127	1.310	178.33
	15480064	53829.510	17.066	-15.416	43.312	43.136	1.311	178.33
	15480320	53828.522	17.066	-15.420	43.312	43.153	1.315	178.33
	15480576	53827.934	17.066	-15.422	43.312	43.163	1.316	178.33
	15480832	53827.234	17.066	-15.424	43.312	43.175	1.318	178.33
	15481088	53826.620	17.066	-15.426	43.312	43.185	1.320	178.33
	15481344	53826.043	17.066	-15.428	43.312	43.195	1.321	178.33
	15481600	53825.627	17.066	-15.430	43.312	43.202	1.322	178.33
2001 UQ_{18}	15465472	53789.293	3.555	23.639	45.333	45.141	1.245	1017.5
	15467264	53787.865	3.555	23.641	45.333	45.117	1.239	1017.5
	15467776	53786.606	3.555	23.642	45.333	45.096	1.233	1017.5
	15468544	53785.191	3.555	23.644	45.333	45.072	1.225	1017.5
	15469568	53783.939	3.555	23.646	45.332	45.051	1.218	1017.5
	15470592	53782.506	3.555	23.649	45.332	45.027	1.210	1017.5
2000 OK_{67}	11112192	53313.598	22.523	-11.822	40.575	40.069	1.251	1353.2
	11112448	53315.665	22.521	-11.826	40.575	40.099	1.274	1353.2
	11112704	53317.833	22.521	-11.828	40.574	40.132	1.297	1353.2
	11112960	53319.642	22.520	-11.830	40.574	40.160	1.315	1353.2
2002 VT_{130}	15466240	53789.244	4.035	21.872	42.751	42.454	1.286	1017.5
	15470848	53787.914	4.035	21.873	42.751	42.432	1.276	1017.5
	15471872	53786.819	4.036	21.874	42.751	42.414	1.268	1017.5
	15473408	53785.239	4.036	21.875	42.751	42.388	1.256	1017.5
	15474432	53783.992	4.036	21.876	42.750	42.368	1.245	1017.5
	15475456	53782.555	4.037	21.878	42.750	42.345	1.233	1017.5
2001 QD_{298}	11104000	53311.970	21.795	-18.498	41.185	40.851	1.341	1521.1
	11104256	53314.020	21.794	-18.497	41.185	40.885	1.355	1521.1
	11104512	53316.141	21.794	-18.495	41.185	40.920	1.368	1521.1
	11104768	53318.147	21.793	-18.493	41.185	40.953	1.379	1521.1
2001 RZ_{143}	11107072	53365.380	1.324	8.942	41.376	40.927	1.253	1353.2
	11107328	53367.599	1.323	8.938	41.376	40.962	1.275	1353.2
	11107584	53369.426	1.323	8.935	41.376	40.991	1.292	1353.2
	11107840	53371.428	1.322	8.932	41.376	41.023	1.309	1353.2

Table 2.3 P3542 70 μm Observations, cont'd.

Object	AORKEY	MJD	RA (h)	Dec (˚)	r (AU)	Δ (AU)	α (˚)	t[a] (s)
2001 QS_{322}	15465984	53711.355	23.559	-2.865	42.345	41.943	1.263	1017.5
	15468800	53709.959	23.559	-2.862	42.345	41.921	1.250	1017.5
	15469824	53708.313	23.560	-2.858	42.345	41.896	1.234	1017.5
	15471616	53706.114	23.560	-2.853	42.345	41.862	1.212	1017.5
	15473152	53704.719	23.561	-2.849	42.345	41.841	1.196	1017.5
2001 QT_{322}	11093248	53363.199	23.644	-0.848	36.921	36.890	1.564	1688.9
	11093504	53364.609	23.645	-0.846	36.921	36.914	1.564	1688.9
	11093760	53365.530	23.645	-0.844	36.921	36.930	1.563	1688.9
	11094016	53367.193	23.645	-0.841	36.921	36.958	1.561	1688.9
	11094272	53368.648	23.646	-0.838	36.921	36.983	1.559	1688.9
	11094528	53369.716	23.646	-0.835	36.921	37.001	1.556	1688.9
2002 KX_{14}	15463168	53615.183	15.749	-20.126	39.607	39.594	1.482	430.09
	15463680	53613.435	15.748	-20.124	39.607	39.565	1.481	430.09
	15464192	53611.763	15.748	-20.123	39.607	39.537	1.479	430.09
	15464704	53610.391	15.748	-20.122	39.607	39.514	1.477	430.09
	15465216	53608.642	15.747	-20.120	39.607	39.485	1.473	430.09
2001 QR_{322}	11090176	53364.982	0.180	0.350	29.708	29.567	1.928	1688.9
	11090432	53367.362	0.180	0.355	29.709	29.608	1.936	1688.9
	11090688	53369.370	0.181	0.360	29.709	29.642	1.939	1688.9
	11090944	53371.371	0.182	0.365	29.709	29.677	1.941	1688.9
2003 QX_{111}	11099392	53362.720	23.851	-4.599	39.485	39.424	1.461	1688.9
	11099648	53364.174	23.851	-4.596	39.486	39.450	1.462	1688.9
	11099904	53365.242	23.851	-4.593	39.486	39.468	1.462	1688.9
	11100160	53367.246	23.851	-4.587	39.487	39.503	1.461	1688.9
	11100416	53368.187	23.852	-4.584	39.487	39.520	1.460	1688.9
	11100672	53368.947	23.852	-4.582	39.488	39.533	1.459	1688.9

[a]Total integrated exposure time.

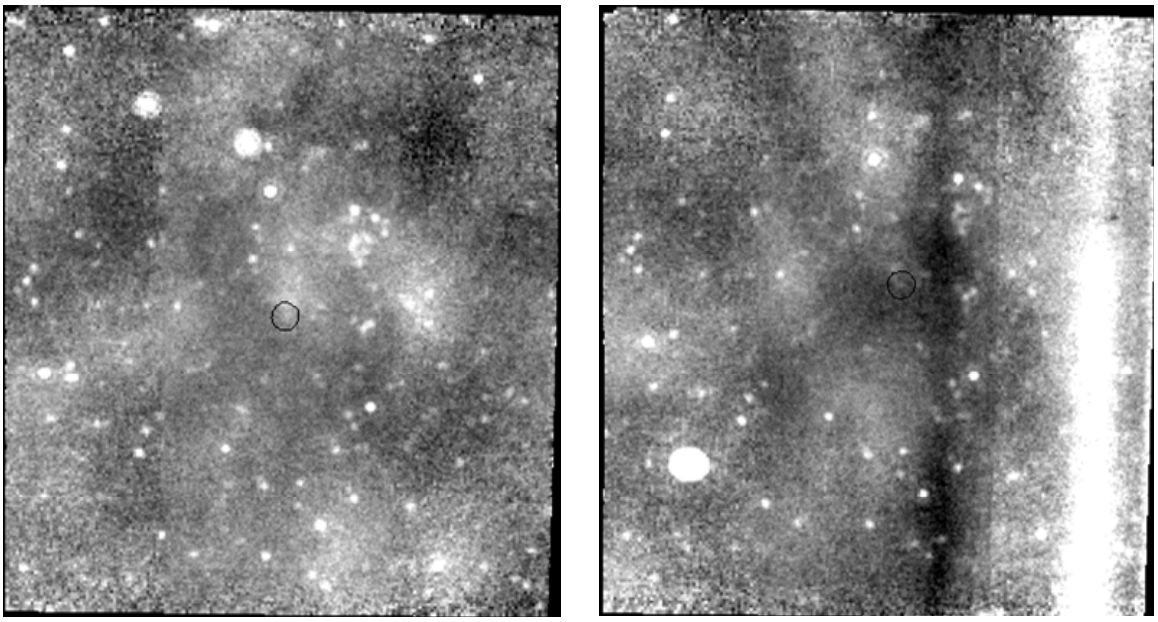

Figure 2.4. 24 μm images of 2002 VT_{130} rejected due to the background. The black circle marks the target position. Left: AORkey 15472640. Right: AORkey 15473408.

2.4 Program P50540 Observations

We observed 2001 KD_{77} as part of cycle 5 program P50540. *SST*'s cycle 5 observations ran from July 1, 2008 through April 2009. The observations for P50450 were conducted October 20, 2008 through October 25, 2008. The investigating team consisted of Dr. William M. Grundy (Lowell Observatory), Dr. John A. Stansberry (Steward Observatory), Dr. Keith S. Noll (Space Telescope Science Institute), Dr. Michael Müller (formerly of Steward Observatory), Melissa J. Brucker (Lowell Observatory and University of Oklahoma), Dr. Stephen C. Tegler (Northern Arizona University), Dr. David J. Osip (Las Campanas Observatory, OCIW, Chile), and Dr. Harold F. Levison (Southwest Research Institute). The goal of this investigation was to explore the boundaries of the cold Classical Kuiper belt population. The inner and cold Classical KBOs may have formed closer to the Sun than their current orbits, been picked up and transported outward by Neptune's migrating mean motion resonances, and subsequently released. If so, then we would expect low inclination 3:2 Resonant KBOs

to be similar to inner Classicals (former residents of that resonance) and low inclination 2:1 Resonant KBOs to be similar to cold Classicals. As a 3:2 Resonant KBO with low inclination and eccentricity, observations of 2001 KD_{77} will inform us if it is more like the inner and cold Classicals or if it is more like dynamically hot 3:2 Resonant KBOs.

Besides observing 2001 KD_{77}, time was requested to observe the 2:1 Resonant KBOs 2005 CA_{79} and 2005 RS_{43} and the inner Classical objects (144897) 2004 UX_{10} and (35671) 1998 SN_{165}. Figure 2.2 illustrates how these objects relate to other KBOs that have been discovered. For greater insight into the dynamical evolution of cold Classical KBOs, it would have been extremely useful to observe one or both of the 2:1 Resonant KBOs (even though they have inclinations greater than 5º) and determine whether or not they have high albedos. We were only granted observing time for 2001 KD_{77} in this final cycle of observations taken by *SST* before it ran out of its cooling cryogens.

Table 2.4 Orbital Properties of *SST* Cycle 5 Program P50540 Target

Provisional Designation	a (AU)[a]	e[a]	i (°)[a,b]	H_V[c,d]	V-R[d]	DES Type
2001 KD_{77}	39.4596	0.1152	2.4062	6.341±0.017	0.619±0.025	3:2

[a]Values averaged over 10 Myr orbital integrations.
[b]Average inclination is with respect to the invariable plane.
[c]Hv was estimated by combining V magnitudes weighted according to their error bars, assuming G=0.15 in the Bowell et al. (1989) photometric system. The larger of the formal error and the scatter of the individual measurements was taken as the uncertainty.
[d]Doressoundiram et al. (2002), Doressoundiram et al. (2007), and Peixinho et al. (2004).

Table 2.5 P50540 24 μm Observations

Object	AORKEY	MJD	RA (h)	Dec (˚)	r (AU)	Δ (AU)	α (˚)	t[a] (s)
2001 KD_{77}	26376448	54759.683	260.121	-21.262	35.658	35.674	1.646	65.94
	26376704	54760.967	260.129	-21.264	35.658	35.696	1.644	65.94
	26376960	54762.259	260.138	-21.267	35.658	35.718	1.642	65.94
	26377216	54763.604	260.148	-21.269	35.659	35.741	1.639	65.94
	26377472	54764.920	260.159	-21.272	35.659	35.763	1.635	65.94

[a]Total integrated exposure time.

Table 2.6 P50540 70 μm Observations

Object	AORKEY	MJD	RA (h)	Dec (˚)	r (AU)	Δ (AU)	α (˚)	t[a] (s)
2001 KD_{77}	26376448	54759.685	260.121	-21.262	35.658	35.675	1.646	765.77
	26376704	54760.969	260.129	-21.264	35.658	35.696	1.644	765.77
	26376960	54762.260	260.138	-21.267	35.658	35.718	1.642	765.77
	26377216	54763.605	260.148	-21.269	35.659	35.741	1.639	765.77
	26377472	54764.921	260.16	-21.272	35.659	35.763	1.635	765.77

[a]Total integrated exposure time.

Chapter 3

Data Reduction

After the observing campaign for P3542 was complete, the MIPS images needed to be processed and combined to produce thermal flux measurements for analysis. These images do not need bias subtraction or flat-fielding since they come preprocessed by J. Stansberry and the Spitzer team who combine individual DCEs into a .fits file format mosaic image and remove instrumental artifacts. After I joined this project in the fall of 2006, I requested that J. Stansberry reprocess the images using the most recent version of the data pipeline.

I used the separate 24 μm and 70 μm MIPS reduction programs of W. Grundy in IDL (Interactive Data Language) as a starting point for developing an image reduction routine. From these programs, I constructed one program that processes and measures the target KBO flux for images taken in either the 24 μm or 70 μm wavelength channel. In the summer of 2007, I downloaded updated Spitzer ephemeredes for our objects from the JPL Horizons ephemeris service (http://ssd.jpl.nasa.gov/?horizons). To measure the flux of the object from the observations, the program begins by reading the ephemeris into IDL. Next, the user is prompted to enter the wavelength channel of the observations to be analyzed. This initializes all of the wavelength-specific calibration factors and viewing scale factors and selects the correct wavelength-specific PSF image.

Once the wavelength-specific factors are defined, the chronologically middle mosaic image is designated as the reference image. Then the mosaic images and their headers are read and stored. The size of the reference image is measured and used to determine the size required to create a padded super-sky image. Once the images are

shifted into sidereal alignment, the padding keeps image edges from falling outside the boundary (recall that the FOV is shifted in between AORs).

Using the information from the ephemeris file and the Julian dates in the .fits headers, the right ascension (RA), declination (Dec), distance from the Sun (r), distance from *SST* (Δ), and the phase angle (α) at the time of exposure are interpolated. The phase angle is the angle between the Sun, the object, and the observer. The images are shifted into sidereal alignment with the reference image and any empty spaces along the edges are set equal to i ($\sqrt{-1}$) so that they are not mistaken for regions of data. The x,y pixel position of the target is determined by using the .fits header to convert the RA and Dec previously interpolated from the ephemeris into pixel coordinates (Figures 3.1a, 3.2a, 3.3a, and 3.4a). After the target regions are marked in all the images, the image sequence is reviewed by eye. If an asteroid passes through the target pathway, then the image containing the asteroid is rejected (see Figure 2.3).

The median pixel value is found for the region surrounding the target excluding the brightest 20% and dimmest 10% of the pixels. This is tuned to exclude the outlying values and asteroids à la J. Stansberry. The mean is calculated of the median pixel values from the set of images. The difference between the mean of medians and the median value for an individual image is added to that image resulting in all images having the same median value in the area of interest. This compensates for drifts in sky brightness between observations.

A disk with a radius of four pixels is masked about the object's target position in each image. The masked images are averaged together pixel by pixel to create a super-sky image. If less than four pixels overlap, then the mean is taken. If four or five pixels

overlap, then the mean is taken after rejecting the maximum and minimum values. If six or more pixels overlap, then a robust mean is taken (cf. Buie and Bus 1992). Once the super-sky image is constructed (illustrated by Figures 3.1b, 3.2b, 3.3b, and 3.4b) from the masked images, it is subtracted from the unmasked sidereally-aligned images.

After the background sky has been subtracted, the images are shifted into alignment on the target position. Then the images are averaged together pixel by pixel following the same rules as when creating the super-sky. If the object is readily detectible by eye, the centroid function is used to find the object's exact center and that central point is set as the new target position instead of the position denoted by the ephemeris. The target position was realigned for the 24 μm average images of Quaoar, 2001 QR_{322}, 1996 TS_{66}, and 2002 VT_{130} and the 70 μm average image of Quaoar. See Table 3.1 for the offset amounts. Examples of final average images in both wavelengths are illustrated in Figures 3.1c, 3.2c, 3.3c, and 3.4c.

After the average image is created, the flux of the target object needs to be measured. I employed PSF fitting photometry to measure the flux of the target TNOs after comparing the flux measurements and uncertainties found using aperture photometry to those found using PSF fitting photometry.

The PSF images used to fit to the target objects were provided by J. Stansberry and the Spitzer team (Engelbracht et al. 2007, Gordon et al. 2007). psf24_80K_s5_sm9.fits (Figure 3.5) and psf70_80K_s5_sm7.fits (Figure 3.6) are smoothed point-spread functions, generated with the Spitzer TinyTim software (Krist 2002), designed to represent point sources at 80 K as viewed by MIPS in the 24 μm channel and the 70 μm channel respectively. The PSF image is normalized so that its

integral is unity by dividing each pixel value by the sum of all pixel values. Next, the PSF is rescaled to match the pixel scale of the average object image (the 24 μm plate scale is 1.245 arcsec/pixel and the 70 μm plate scale is 4.925 arcsec/pixel). Taking a small excerpt of the average object image, the PSF image is shifted so that the center of the PSF has the same *x,y* pixel coordinates as the target position in the excerpt of the average object image. The IDL function amoeba locates the values for the PSF brightness and background brightness that fit the target with the lowest χ^2. The flux measurement is the product of the best-fitting PSF brightness, the square of the plate scale, and the calibration factor. The 24 μm calibration factor is 0.001067 mJy/arcsec^2/DN or 0.0454 MJy/sr (Engelbracht et al. 2007). The 70 μm calibration factor is 16.5 mJy/arcsec^2/DN or 702 MJy/sr (Gordon et al. 2007).

The uncertainty in the flux measurements is calculated by fitting the PSF to regions of sky surrounding the target (24 regions for the 24 μm images and 20 regions for the 70 μm images) as illustrated in Figures 3.1c, 3.2c, 3.3c, and 3.4c. The uncertainty is the product of the calibration factor, the square of the plate scale, and the standard deviation of the set of PSF brightnesses with the lowest χ^2.

Color corrections are necessary to convert the flux measurements and uncertainties from the 24 μm and 70 μm MIPS bandpasses (the instrumental reflections, transmissions, and detector response; Hansen 1977) to monochromatic flux densities at 23.68 μm and 71.42 μm. They were determined using the correction table provided by Stansberry et al. (2007). Quaoar and 2001 QR_{322} have strong signals in both wavelengths thus the color corrections for these objects were calculated iteratively with the temperature until the temperature converged. The surface temperatures for the other

bodies were approximated from the temperatures found for Quaoar and 2001 QR_{322} assuming that temperature is inversely proportional to the square root of an object's distance from the Sun. This comes from Equation 4.4 where the absorbed visible light is equated to the emitted thermal light: $1/r^2 \propto T^4$.

The color corrections for the other bodies were interpolated while keeping the approximate temperature constant (Table 3.2). Lastly, the color-corrected flux measurements were modeled with the Standard Thermal Model to constrain the KBO radii and albedos using a Monte Carlo simulation as described in section 4.4.

Table 3.1 Centroid Offsets from Ephemerides

Provisional Designation	λ (μm)	Δx (pix)	Δy (pix)	Δx (“)	Δy (“)
Quaoar	70	0.589	-0.177	2.901	-0.872
Quaoar	24	0.631	0.148	0.786	0.184
2001 QR_{322}	24	0.774	0.289	0.964	0.360
1996 TS_{66}	24	-0.431	0.247	-0.537	0.308
2002 VT_{130}	24	-0.290	0.322	-0.361	0.401

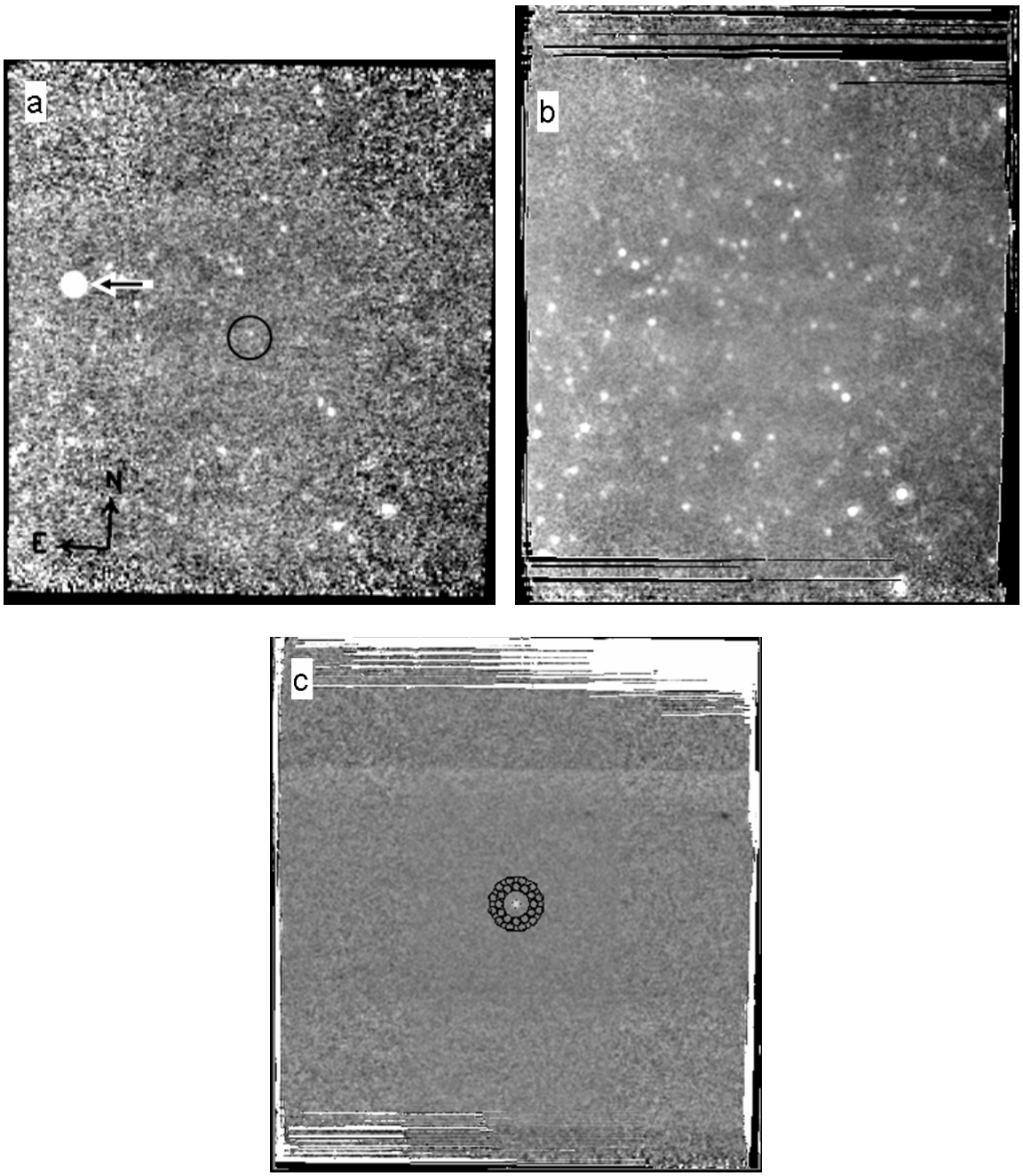

Figure 3.1. (Brucker et al. 2009, Fig. 2) "(a) A single mosaic image of Quaoar at 24 μm. The [black] circle marks the position of Quaoar and the arrow points to a foreground asteroid passing through the FOV. Black lines around the edges are undefined pixels. (b) This super-sky image is the average of twelve mosaic images to facilitate background subtraction. It is larger than (a) since the composite images have slightly different FOVs due to dithering. (c) The final image is an average of twelve sky-subtracted mosaic images. 24 circles in a double ring around Quaoar mark the centers of regions used to measure the background noise. The scale is 1.245 arcsec pixel^{-1} giving (c) a FOV of 7.57'x8.36'."

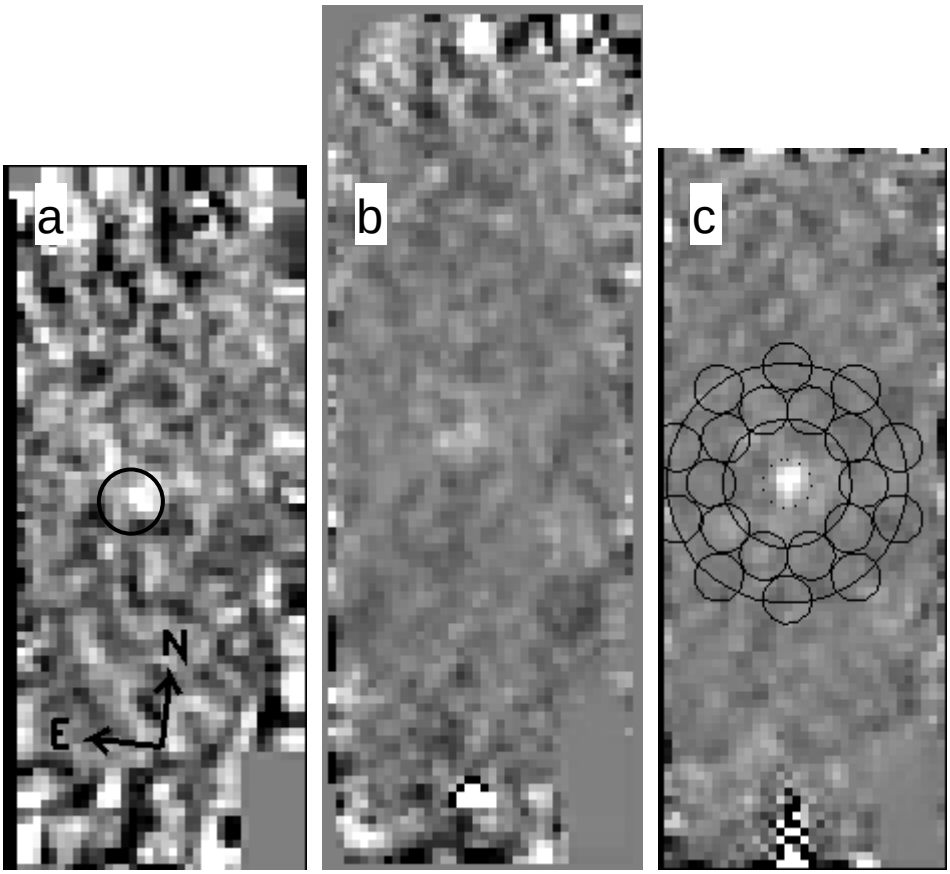

Figure 3.2. (Brucker et al. 2009, Fig. 3) "Similar to [Figure 3.1] for Quaoar at 70 μm with a scale of 4.925 arcsec pixel^{-1} giving (c) a FOV of 2.87'x7.39'. 20 circles mark the measured background noise regions. The 70 μm images have half the FOV of the 24 μm images due to an external cable failure that disabled half of the array and the gray box in the lower right corner of each image contains no data due to an additional cable failure (Rieke et al. 2004, Gordon et al. 2005)."

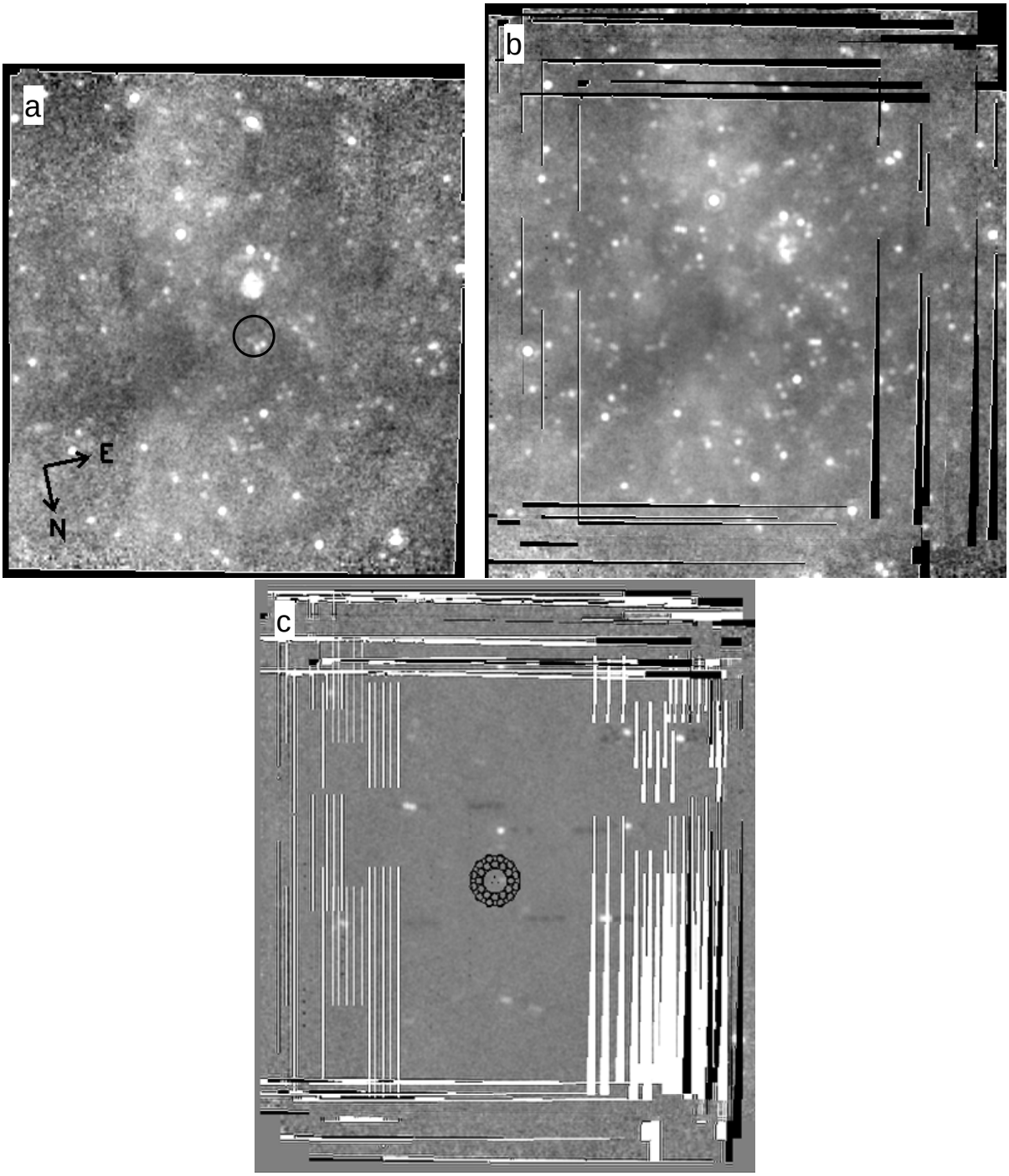

Figure 3.3. Similar to Figure 3.1 for the KBO 2002 VT_{130}.

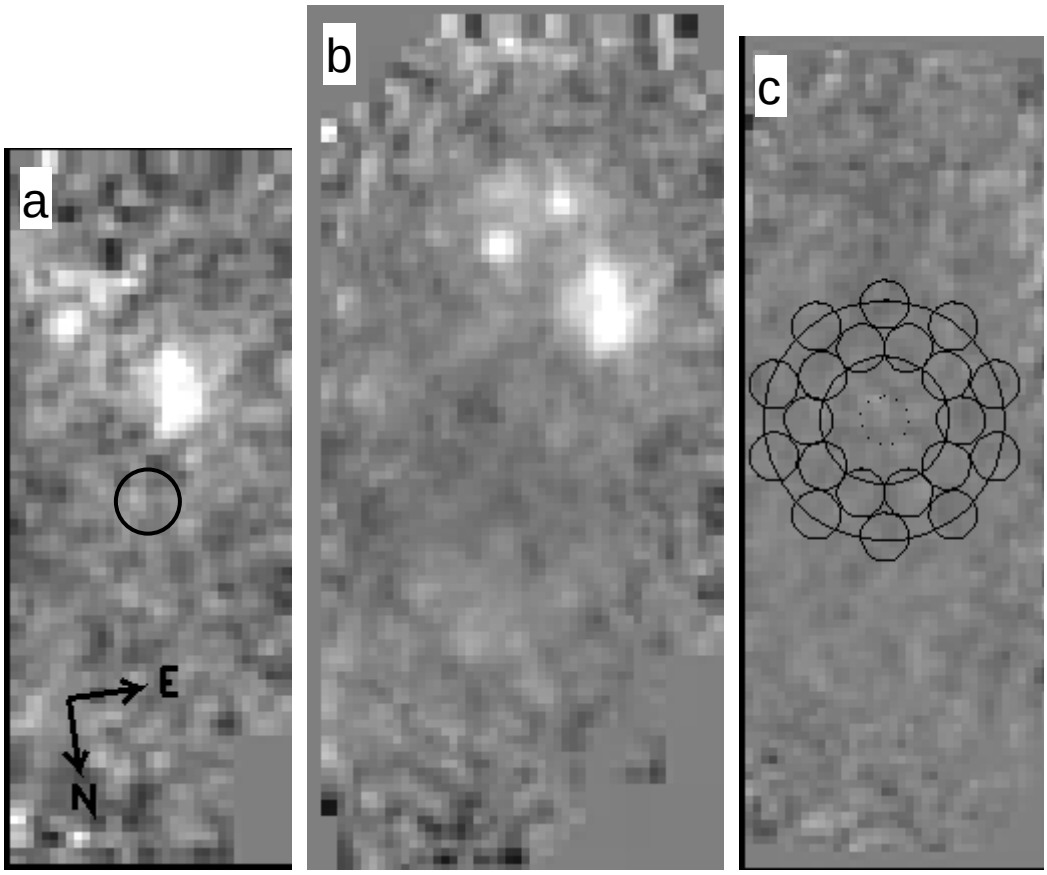

Figure 3.4. Similar to Figure 3.2 for the KBO 2002 VT_{130}.

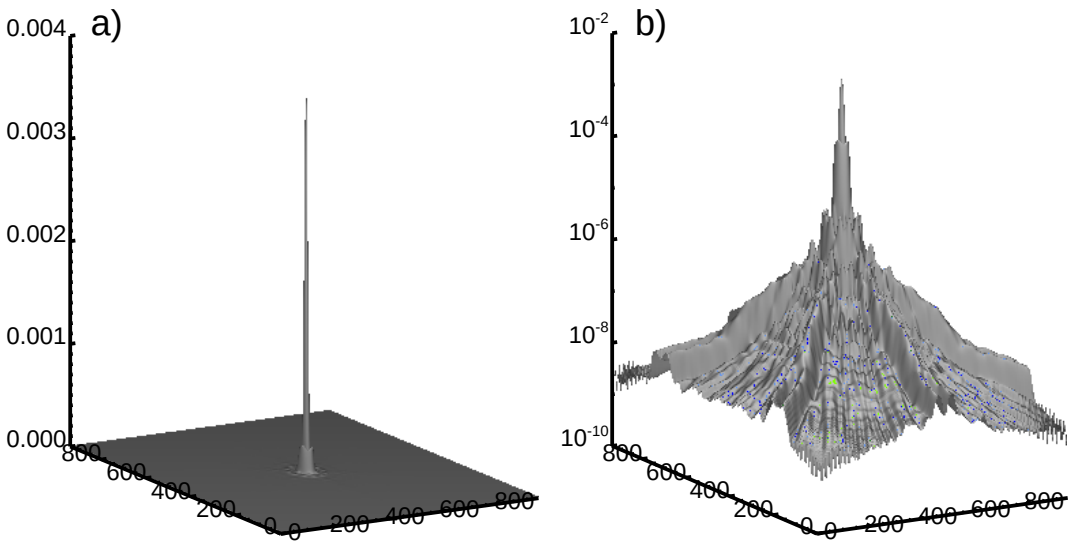

Figure 3.5. This PSF represents a point source of temperature 80 K viewed through the 24 μm channel of MIPS. a) The normalized brightness where the x-axis and y-axis are labeled in pixel coordinates. b) The log of the normalized brightness. The log plot clearly shows the model of the interference patterns.

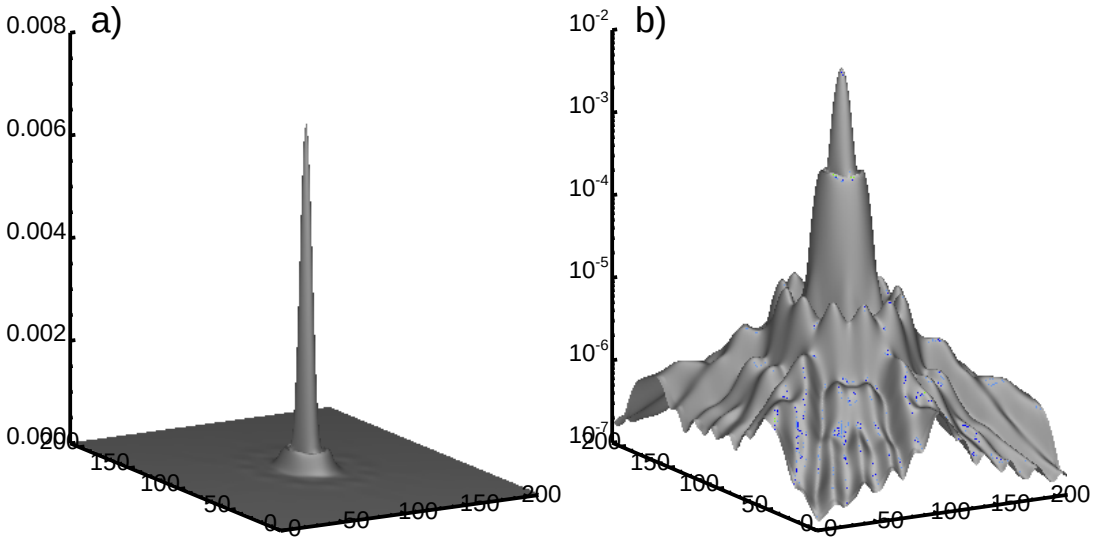

Figure 3.6. Similar to Fig. 3.5 for the 70 μm channel of MIPS.

Table 3.2 Color Corrections

		Measured:				Corrected:			
		24 μm:		70 μm:		24 μm:		70 μm:	
Object	T[a] (K)	Flux (mJy)	σ[b] (mJy)	Flux (mJy)	σ[b] (mJy)	Flux (mJy)	σ (mJy)	Flux (mJy)	σ (mJy)
2001 KA_{77}	47	0.0092	0.0029	3.63	0.70	0.0772	0.0024	4.07	0.79
2002 GJ_{32}	51	0.0113	0.0069	1.28	0.79	0.0101	0.0061	1.43	0.89
1996 TS_{66}	55	0.1003	0.0046	2.65	0.81	0.0936	0.0043	2.95	0.91
Quaoar	51	0.2520	0.0063	21.99	1.98	0.2243	0.0056	24.61	2.22
2002 KW_{14}	54	0.0031	0.0066	2.92	0.93	0.0029	0.0061	3.26	1.03
Altjira	49	0.0191	0.0032	-2.24	0.69	0.0167	0.0028	-2.52	0.77
2000 OK_{67}	53	0.0334	0.0074	-0.33	0.79	0.0305	0.0068	-0.37	0.88
2002 VT_{130}	51	0.0888	0.0051	0.35	0.87	0.0794	0.0045	0.39	0.98
2001 QD_{298}	53	0.0536	0.0065	1.41	0.89	0.0487	0.0059	1.57	0.99
2001 RZ_{143}	53	0.0508	0.0075	-0.71	0.60	0.0461	0.0068	-0.80	0.67
2001 QS_{322}	52	0.0010	0.0041	-1.27	0.90	0.0009	0.0037	-1.42	1.01
2001 QT_{322}	57	0.0429	0.0059	-0.21	0.94	0.0406	0.0056	-0.24	1.05
2002 KX_{14}	54	0.0852	0.0094	1.97	1.28	0.0787	0.0086	2.20	1.43
2001 QR_{322}	66	0.1680	0.0102	2.70	0.51	0.1685	0.0102	2.98	0.56
2003 QX_{111}	54	0.0205	0.0075	3.92	1.14	0.0190	0.0069	4.37	1.27
2001 KD_{77}	58	0.0777	0.0196	-2.22	1.90	0.0713	0.0180	-2.74	2.33

[a]Temperatures are approximations only and are not for use in thermal modeling.
[b]Uncertainties are the standard deviations of the background flux in regions surrounding the target.

Chapter 4

Thermal Modeling

Small icy TNOs appear in images as unresolved point sources. How can the radius of an unresolved point source be measured? For a given visual magnitude, a minor planet could be small and bright or large and dark. The absolute visual magnitude, H_V, of a TNO corresponds to the amount of sunlight reflected off the TNO's surface. The thermal emission (which peaks in the infrared for objects at temperatures found in the outer solar system) corresponds to the amount of sunlight absorbed by the TNO. A large dark object is warmer and radiates more than a small bright object since it absorbs more incident sunlight than the small bright object. Hence thermal modeling can constrain the radius and albedo of an object from its infrared flux measurements in conjunction with its absolute visual magnitude.

Three main thermal models, to be described below, are the Thermophysical Model, the Standard Thermal Model, and the Isothermal Latitude Model. For all three thermal models that I investigated, I assumed a linear function for the phase integral, q, based upon visual data from icy satellites of gas giants.

$$q = 0.336 * p_V + 0.497 \tag{4.1}$$

where p_V is the visual geometric albedo. The phase integral is a function that is empirically determined from observations at phase angles from 0º to 180º. Since the New Horizons spacecraft has not yet reached the Kuiper belt, no direct data are available for TNOs. Icy satellites are the closest accessible substitutes for TNOs for phase integrals and other surface properties. Equation 4.1 does not include data from Europa and Phoebe as those data points are apparent outliers (Figure 4.1). Morrison (1973) used

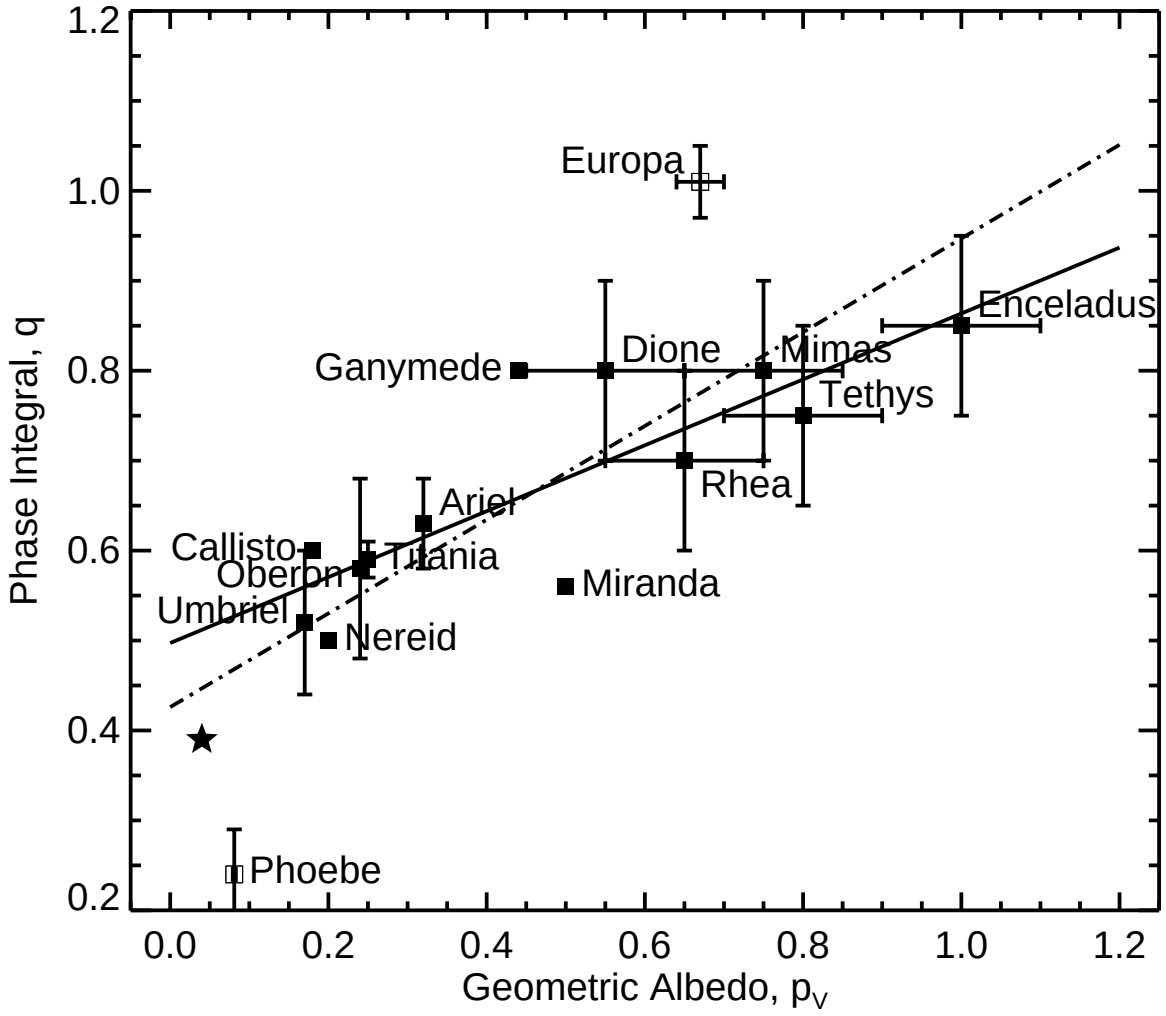

Figure 4.1. (Brucker et al. 2009, Fig. 1.) "The visual geometric albedo, p_V, is plotted versus the phase integral, q, for icy satellites of gas giants. The solid line is the adopted best linear fit to the satellite data without including Phoebe and Europa: $q=0.336*p_V+0.497$. The dot-dashed line is the best linear fit to the data including Phoebe and Europa: $q=0.521*p_V+0.426$. Since not all of the data points had published error bars, the points were not weighted according to their errors when determining the linear fit. The data come from Buratti et al. (1990), Cruikshank and Brown (1986), Grundy et al. (2007), Morrison et al. (1986), Simonelli et al. (1999), Thomas et al. (1996), and Veverka et al. (1986)." The star is placed at the intersection of the traditionally assumed values of 0.39 for the phase integral and 0.04 for the visual geometric albedo.

phase integral values of 1.0 and 0.6 to evaluate the radii and albedos of Galilean satellites. However, these high phase integrals appear not to have become commonplace when interpreting data from icy satellites. The standard phase integral for dark asteroids is 0.39 (Bowell et al. 1989) and has been adopted for TNOs in other studies (e.g.

Stansberry et al. 2008). We do not claim that a linear fit to the data is the only approach; rather, that it is more appropriate for use with TNOs than assuming that $q = 0.39$ since all of the satellites in Figure 4.1 (presumably similar to TNOs) have phase integrals greater than or equal to 0.5.

Changing the phase integral results in a negligible difference in the modeling results; however, the Bond albedo, A_B, increases dramatically when the linear function for q is employed instead of 0.39; A_B is directly proportional to q:

$$A_B = p_V * q \tag{4.2}$$

This dependence appears in the Thermophysical Model given that the thermal flux is a function of the Bond albedo and the radius (the visual absolute magnitude is a function of the geometric albedo and the radius). The geometric albedo is the ratio of a body's disk-integrated brightness at zero phase angle to the brightness of an equivalently-sized Lambertian disk with perpendicular illumination (Spencer 1987). The bolometric Bond albedo is the ratio of the total reflected light to the total incident light for a surface (Spencer 1987). Thus the light absorbed by the object is proportional to $(1-A_B)$.

In addition to assuming a linear function for the phase integral, I assumed that the visual geometric albedo, p_V, is equivalent to the bolometric geometric albedo, p. This is practical since solar radiation peaks in V. I also assumed that all objects were observed at a phase angle, α, of 0º (α is the Sun-object-observer angle). All the objects were observed at phase angles between 1º and 2º which are close enough to zero since thermal emissions do not produce narrow opposition surges like reflected light does (the visible light observed from TNOs).

I assumed that thermal radiation from TNOs may be approximated as blackbody radiation from a spherical object. In order to determine the blackbody radiation, the temperature must be determined. The visible light absorbed by the object is equated to the light emitted thermally by the object:

$$\pi R^2 (1 - A_B) S / r^2 = \eta \varepsilon \sigma R^2 \int_{-\pi}^{\pi} \int_{-\pi/2}^{\pi/2} T^4(\theta, \phi) \cos\phi d\phi d\theta \qquad (4.3)$$

where R is the radius, A_B is the bolometric Bond albedo, S is the solar constant (1.373×10^6 erg/cm^{2}s, the flux per unit area per unit time at 1 AU integrated over wavelength), r is the heliocentric distance of the object, η is the beaming factor (discussed in section 4.2), ε is the bolometric emissivity, σ is the Stefan-Boltzmann constant, and $T(\theta,\phi)$ is the temperature at latitude and longitude (θ,ϕ) (Lebofsky and Spencer 1989). The right-hand side of Equation 4.3 is tailored to whichever thermal model is being employed. Then the equation is solved for the temperature at which to evaluate the thermal radiation.

4.1 The Thermophysical Model

The Thermophysical Model (TPM) is the most physically realistic of the three models. It uses one-dimensional conduction below the surface to model an object's surface temperature. To do so, the thermal conductivity, specific heat capacity, and density must be designated; they are assumed to be constant over time and with respect to temperature. The model does allow for substrates of different thermal properties as long as they remain constant.

The thermal inertia describes a surface's resistance to change temperature as follows:

$$\Gamma = \sqrt{\kappa c \rho} \tag{4.4}$$

where κ is the thermal conductivity, c is the specific heat capacity, and ρ is the density. The thermal parameter, Θ, is a dimensionless parameter that expresses the surface reaction time to changes in insolation such that an object with a high thermal parameter does not change temperature much.

$$\Theta = \Gamma \sqrt{\omega} / \varepsilon \sigma T_{SS}^3 \tag{4.5}$$

where ω is the rotational angular velocity, ε is the emissivity, σ is the Stefan-Boltzmann constant, and T_{SS} is the subsolar temperature (Spencer et al. 1989). An object with a larger thermal parameter than another object will radiate more energy from its night side. The subsolar temperature is a construct representing the temperature needed to produce the radiation from a single point equivalent to the radiation from the entire disk. The subsolar point is the point on the smooth spherical surface whose normal vector points directly towards the Sun.

As an object rotates, sunlight shines upon the surface. For the TPM, if the solid-state greenhouse effect is inactive, all of the incident sunlight is absorbed at the surface. If the solid-state greenhouse effect is active, the insolation penetrates the surface with exponential decay (the accuracy of exponential decay depends heavily on albedo and other surface particle properties according to Antarctic snow studies and Hapke extinction coefficient calculations (Brown and Matson 1987)). The temperature is calculated down to the characteristic skin depth. According to Spencer et al. (1989), the skin depth, l_s, is given by:

$$l_s = \sqrt{\kappa / \rho c \omega} \tag{4.6}$$

The mantle down to the skin depth is divided into a specified number of plane parallel layers or slabs of equal thickness. For the first time step, the starting temperature of each slab is calculated from an initial temperature estimate beginning with the surface slab. The temperature estimate is adjusted by the amount lost due to emission (only for the surface slab), the amount gained from absorption of sunlight, and the amounts gained from conduction from the slabs above (except for the surface slab) and below (except for the lowest slab). Conduction from below into the lowest slab is not considered. The insulating lower boundary condition assumes that the object has no internal heat source. This is logical since the objects to be modeled are small and should not generate much radiogenic heating. After the initial time step, the temperature estimate before adjustments for each slab is set equal to its temperature from the preceding time step. The temperature calculations for all the slabs are repeated for each time step of a complete rotational period. The surface temperature is recorded for a point on the surface as a function of time (the insolation at that point changes as the body rotates). Once the

surface temperatures have been calculated over time, the thermal emission is calculated via the Planck function. For isotropic radiation, the monochromatic flux, F_λ, is given by:

$$F_\lambda d\lambda = \frac{2\pi R^2 hc^2 / r^2 \lambda^5}{e^{hc/\lambda kT} - 1} d\lambda \tag{4.7}$$

where R is the radius, h is Planck's constant, c is the speed of light, r is the distance to the object, λ is the wavelength, k is Boltzmann's constant, and T is the temperature.

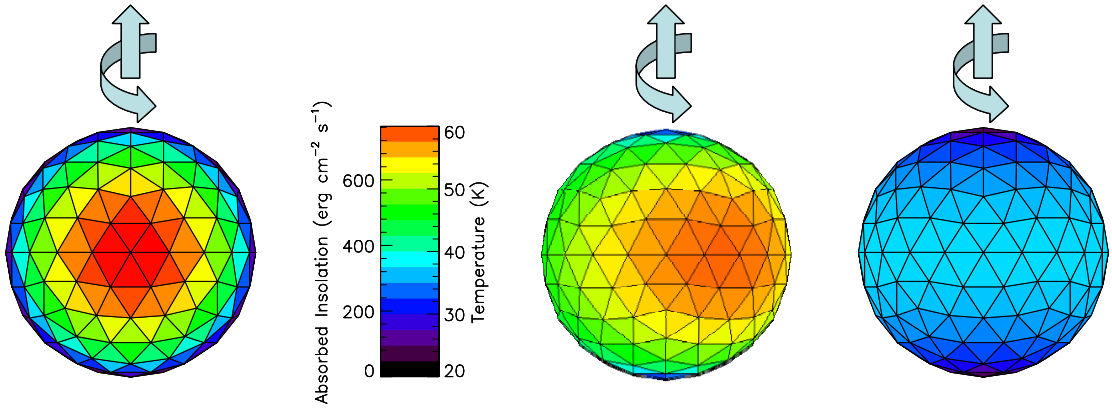

Figure 4.2. Illustrations for the Thermophysical Model where the Sun is in the same direction as the observer and the rotational axis points upward. Left: The incident sunlight absorbed by the object. Middle: The temperature of the object for $\Gamma = 4500$ erg/cm^{2}s$^{1/2}$K. Note that the temperature lags behind the insolation. This object with a lower thermal inertia cools off at night. Right: The temperature of the object for $\Gamma = 10^5$ erg/cm^{2}s$^{1/2}$K. The object remains warm throughout the night but the maximum temperature is not as high for this object with its higher thermal inertia.

4.2 The Standard Thermal Model

The Standard Thermal Model (STM) determines the thermal emissions from a spherical object with a smooth surface in instantaneous equilibrium with the insolation. This requires a non-rotating object or an object whose surface has a thermal inertia, Γ, of zero. The STM is often referred to as the slow rotator STM for the assumption of non-rotation.

When a surface is in instantaneous equilibrium, the amount of radiation absorbed is equivalent to the amount of radiation emitted. Equation 4.3 can be simplified to the following:

$$(1 - A_B)\, S / r^2 = \eta \varepsilon \sigma T_{SS}^4 \tag{4.8}$$

where A_B is the Bond albedo, S is the solar constant at 1 AU, r is the heliocentric distance of the object, η is a beaming factor, ε is the bolometric emissivity, σ is the Stefan-Boltzmann constant, and T_{SS} is the subsolar temperature (Spencer et al. 1989). To determine the subsolar temperature, one needs only to solve Equation 4.8 for T_{SS}. Once the subsolar temperature is calculated, the temperature, T, at any location may be found with the following equation:

$$\begin{aligned} T &= T_{SS} \cos^{1/4} i, \quad i \le \pi/2 \\ T &= 0, \qquad\qquad\quad i > \pi/2 \end{aligned} \tag{4.9}$$

where i is the solar incidence angle (the angular distance from the subsolar point) (Spencer et al. 1989). After the temperature is evaluated for all the regions on the surface, the thermal emission is determined via the Planck function. The observed thermal flux is the product of the sum of the flux contributions from those regions visible

to the observer, the emissivity, and the inverse square of the distance from the object to the observer.

The STM assumes a smooth surface, a thermal inertia of zero, and no rotation. However, real asteroids and TNOs have rough surfaces, nonzero thermal inertias, and rotation. Thus the STM requires a beaming factor, η, to compensate for increased sunward emission (a decrease in η) caused by surface roughness. The beaming factor derives its name from this increased sunward thermal emission. The beaming factor also adjusts for nonzero thermal inertias and nonzero rotation rates (an increase in η) since thermal radiation is emitted from the night side of asteroids and TNOs (Spencer et al. 1989). In addition, η compensates for more complex physical situations that are neglected in the STM such as limb-darkening, incidence angle effects, crater effects (the centers of craters are warmer due to radiation from the walls; Lebofsky and Spencer 1989), conduction, and phase integral accuracy.

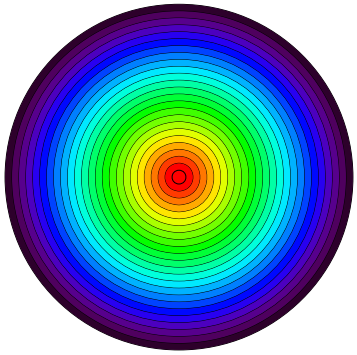

Figure 4.3. With the Standard Thermal Model, an object is warmest at the subsolar point and the temperature decreases with increasing angular distance from the subsolar point. This is illustrated here for a nonrotating object whose subsolar point lies on the equator where red represents the warmest area and violet represents the coolest area visible.

4.3 The Isothermal Latitude Model

The Isothermal Latitude Model (ILM) determines the thermal emissions from a spherical object whose surface is not in instantaneous equilibrium with the incident sunlight. For objects with rotational axes perpendicular to the incident sunlight, the temperature at any point on the surface can be determined from the following equation:

$$\begin{aligned} T &= T_{SS} \cos^{1/4} \phi, \quad \phi \le \pi/2 \\ T &= 0, \qquad\qquad\quad \phi > \pi/2 \end{aligned} \tag{4.10}$$

where ϕ is the latitude (Lebofsky and Spencer 1989; for the STM, the angle i was the angular distance from the subsolar point). This formula describes latitudinal bands of constant temperature. Isothermal latitudes occur for objects rotating rapidly, objects with high thermal inertias ($\Gamma \to \infty$; rocky surfaces), and objects that are very cold. The ILM is sometimes referred to as the fast rotator STM.

Our version of the ILM allows for rotational axes of different orientations. This is advantageous as it is statistically unlikely that all TNOs have axes aligned perpendicular (ILM) or parallel (STM) to the line of sight. In fact, the average expected viewing angle is a subsolar latitude of 30º (Sheppard et al. 2008, Spencer et al. 1989).

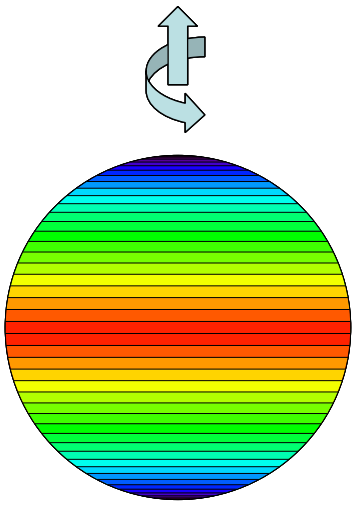

Figure 4.4. With the Isothermal Latitude Model, an object whose rotational axis points upward is warmest along the equator and the temperature decreases with increasing latitude. This is illustrated here where red represents the warmest area and violet represents the coolest area visible.

4.4 Comparing Thermal Models

Modeling radii and albedos of small TNOs with the TPM requires knowledge of surface properties which as yet are unknown. Since we lack the correct input parameters and the computer run time of the TPM is longer than that of the STM and ILM, the TPM was deemed inefficient for our use. I conducted comparisons in order to determine which model, the STM, the ILM at 0º subsolar latitude, or the ILM at 30º subsolar latitude, fits the TPM results the best. The comparison process was conducted with input parameters representing plausible ranges of acceptable dynamic and thermal properties (Table 4.1).

Table 4.1 Thermal Model Comparison Variables and Quantities
(Brucker et al. 2009, Table 3)

Quantity	Symbol	Units	Values
Subsolar Latitude	θ	$^\circ$	0, 15, 30, 45, 60, 75, 90
Bond Albedo	A_B	--	0.01, 0.1, 0.5
Wavelength	λ	μm	23.68, 71.42
Thermal conductivity[a]	κ	erg cm^{-1} s^{-1} K^{-1}	225, 111112
Solar distance	r	AU	30, 50
Observer distance	Δ	AU	29, 49
Rotational Period	P	h	5, 15
Radius	R	km	100
Heat capacity[a]	c	erg g^{-1} K^{-1}	10^5
Density	ρ	g cm^{-3}	0.9
Emissivity	ε	--	0.9

[a]These values were chosen such that the thermal inertia, Γ, is 4500 and 10^5 erg cm^{-2} s$^{-1/2}$ K^{-1}.

Before comparing the STM and ILM to the TPM, we constructed the thermal flux that would be observed from Earth according to the TPM as determined from the parameter sets in Table 4.1. The shape of a TNO was approximated with a nearly spherical triangularly-faceted shape (see Figure 4.2). The normal unit vector for each facet was calculated from the Cartesian coordinates of its vertices. The latitude and longitude of the facet midpoint was also determined. These coordinates were used to evaluate a rotation matrix denoting the position angle of the Sun (incidence angle) and of

the Earth (emission angle) with respect to each facet as the object rotates. With this matrix, the incident solar flux (insolation) on each facet was computed for each time step over a complete rotation period. Next, the TPM was used to model the temperature of each facet as the object rotated. I employed an adjusted beaming factor (as per Spencer 1990) as a substitute for a rough surface algorithm. The flux emitted from each facet was determined from the TPM temperature by assuming that facets radiate as blackbodies. The flux observed from each facet is given by:

$$\frac{fA\varepsilon \cdot \cos(e)}{\pi\Delta^2} \tag{4.11}$$

where f is the emitted flux per unit area, A is the facet area, ε is the emissivity, e is the emission angle (the angle between the facet's normal vector and the direction of the observer), and Δ is the distance between the object and the observer (A and Δ^2 must have the same units). The observed flux is then summed over all the facets, averaged over time (one rotation period), and converted to milliJanskeys (mJy).

The observed flux output from the TPM is fit with the STM, the ILM at 0º, and the ILM at 30º to find the radius, geometric albedo, and beaming factor necessary for each of these models to reproduce the TPM flux. The fitting algorithm iteratively fits the radius and beaming factor using the thermal flux then adjusts the albedo and phase integral after each iteration to correspond with the visual absolute magnitude and the new radius. After the best fitting radius and albedo are found for each model, the percent error is determined when compared to the input radius and albedo for the TPM.

Both the STM and the ILM at 30º reasonably approximate the behavior of the TPM under small TNO-like conditions while the ILM at 0º does not match as well. The

STM has a maximum $^{+3.9}_{-8.3}$% difference and average -0.4% difference in radius and maximum $^{+14.8}_{-8.2}$% difference and average +0.5% difference in albedo when compared to the TPM for the cases tested. The ILM at 30˚ has a maximum $^{+6.4}_{-5.0}$% difference and average +1.6% difference in radius and maximum $^{+9.3}_{-14.2}$% difference and average -3.6% difference in albedo. The ILM at 0˚ has a maximum $^{+10.1}_{0}$% difference and average +4.5% difference in radius and maximum $^{0}_{-23.7}$% difference and average -10.0% difference in albedo. I chose to use the STM in the Monte Carlo simulations as it has smaller average differences from the TPM and is more widely used than the ILM at 30˚ (e.g. Stansberry et al. 2008).

4.5 Applying the STM to *SST* Flux Measurements

The STM is used to model the thermal flux measurements from our observations to determine or constrain radii and albedos. If an object has a flux measurement of signal-to-noise ratio (S/N) less than one (a non-detection) in either wavelength, 23.68 μm or 71.42 μm, then a lower limit on the object's albedo and an upper limit on its radius were derived. For all other objects, flux measurements were input into a Monte Carlo simulation in order to determine the object's albedo, radius, and 1 σ uncertainties. The simulation, designed by W. Grundy, requires the absolute visual magnitude, H_V, and its error; the color-corrected fluxes at 23.68 μm and 71.42 μm and their uncertainties; the distance from the object to the Sun, r, and from the object to the *SST*, Δ; and the number of trials to simulate, n.

Before running the simulation, the total measurement uncertainty must be evaluated. The uncertainties in the absolute calibration of the MIPS channels are 2% and 5% for the 24 μm and 70 μm bandpasses respectively (Engelbracht et al. 2007, Gordon et al. 2007). This does not include a separate color correction term since the color correction does not significantly contribute to the calibration uncertainty (Stansberry et al. 2007). The absolute calibration uncertainties were not determined using faint cold point sources like TNOs. Since KBO targets have lower flux levels and cooler temperatures than the calibration targets and KBO images undergo more processing than the calibration images, I have adopted larger calibration uncertainties of 4% and 8% for the 24 μm and 70 μm channels respectively.

For strong detections, the total measurement uncertainties are given by the rms of the measurement uncertainty and the calibration uncertainty (24 μm equation shown):

$$\sigma_{total} = \sqrt{(\sigma_f)^2 + (0.04 * f)^2} \tag{4.12}$$

where σ_f is the measurement uncertainty and f is the flux measurement. If this flux measurement is near zero, the formula above cannot adequately account for the calibration uncertainty. Thus I chose conservatively to use the greater of the rms uncertainty and $1.04*\sigma_f$ (for 24 μm).

Objects that were detected in both wavelengths are modeled with a Monte Carlo simulation to assess uncertainties in the radius and albedo determinations. The preliminary Monte Carlo simulation begins by adding a random amount of Gaussian error to the observed flux and magnitude values. The random error produces values such that they are consistent with their respective uncertainties, both fluxes generated are greater than zero, and the 70 μm flux is greater than the 24 μm flux. The STM is fit to these randomly generated flux and magnitude values to determine model values for the albedo, radius, and beaming factor. This process is repeated *n* times. Once the *n* trials are completed, the medians and 1 σ uncertainties are found from the resultant sets of albedos, radii, and beaming factors. If the S/N is greater than or equal to four in both wavelengths, then the modeling process is now complete for that object. If the S/N is greater than one and less than four in either wavelength, then an additional round of Monte Carlo simulations is conducted to compensate for biases inherent in the simulation process such as rejecting any randomly generated fluxes which are negative (negative fluxes are unrealistic and cause a fatal error in the STM fitting routine).

For the extended simulations, after the steps described above, an additional *n* baseline sets of flux and magnitude values are constructed by adding to the observed fluxes and magnitude randomly generated amounts of noise consistent with the

observational uncertainties. These *n* sets are fit with the STM to compile *n* trial albedos, radii, and beaming factors.

Next, additional noise is randomly added to each set of baseline flux and magnitude values to simulate the error incurred between the emission and measurement of light, referred to as the 'measured' flux and magnitude. For *n* trials, the 'measured' set of values has a randomized amount of error added to it. The resultant values are fit with the STM to find the albedo, radius, and beaming factor. Once each 'measured' flux and magnitude set has been fit *n* times, the medians and 1 σ uncertainties are calculated as the model values. After all *n* 'measured' sets have been modeled *n* times, we have *n* sets of modeled median albedos, radii, and beaming factors and their 1 σ uncertainties corresponding to *n* sets of trial albedos, radii, and beaming factors. The trial albedos, radii, and beaming factors are divided by the model albedos, radii, and beaming factors. The quotients for like values are sorted to find the median value, upper 1 σ uncertainty, and lower 1 σ uncertainty. These quotients are adjustment factors for the preliminary simulation values. For example, the final radius is the preliminary modeled radius multiplied by the median of the ratios of trial radii to model radii. The upper 1 σ uncertainty in radius is the preliminary radius multiplied by the upper 1 σ uncertainty of the ratios of trial radii to model radii then subtracted by the final radius; similarly for the lower 1 σ uncertainty in radius. For my simulations, *n* was fixed at 10,000 and the correction factors for those objects with S/N less than four but greater than one can be found in Table 4.2.

Table 4.2 Monte Carlo Correction Factors for Marginal Detections
(Brucker et al. 2009, Table 5)

Provisional Designation	R[a]	p_V[a]	η[a]
2001 KA_{77}	1.001	0.9921	1.0112
2002 GJ_{32}	0.8933	1.2421	0.9615
1996 TS_{66}	0.9699	1.0459	0.9732
2001 QD_{298}	0.8552	1.3658	0.8620
2002 KX_{14}	0.8497	1.3756	0.7790
2003 QX_{111}	1.012	0.9234	1.0375

[a]Preliminary radii, geometric albedos, and η values are multiplied by these correction factors. The products are the final values stated in [Table 5.1].

The preliminary simulation does well modeling the radius and albedo of an object when the observations have S/N greater than four. The extended simulation does well modeling the radius and albedo of an object for S/N between four and one; however, the simulations are insufficient for objects with S/N less than one. Instead, upper limits on the radii and lower limits on the albedos were determined from plots of flux vs. radius (see Figure 4.5 for an example). For each object, the absolute magnitude and a series of radii were used to calculate albedos from the following formula:

$$p_V = (R_0/R)^2 10^{-2H_V/5} \tag{4.13}$$

where R_0=664.4. This formula is derived by considering a Lambertian disk located 1 AU from the Sun and 1 AU from an observer at a phase angle of 0º. The observed flux due to Lambertian scattering is $p_V \cos\alpha * S\pi R^2 / \pi\Delta^2$ where p_V is the geometric albedo, α is the phase angle, *S* is the solar constant, *R* is the radius in km, and Δ is the distance from the object to the observer in km. Since α is 0º and Δ is 1 AU, the ratio of the observed flux to the incident flux can be reduced to $p_V SR^2 * \left(\frac{1}{149598000\,km}\right)^2 / S$. From the definition of magnitude, the ratio of the flux scattered off the disk to the flux incident on

the disk can also be expressed by $10^{-2(H_V - V_S)/5}$ where H_V is the object's visual absolute magnitude and V_S is the visual solar magnitude at 1 AU. For V_S = -26.76, we can equate the two statements as follows:

$$10^{-2(-26.76)/5} * 10^{-2(H_V)/5} = p_V S R^2 * \left(\frac{1}{149598000\,km} \right)^2 / S \qquad \text{or}$$

$$10^{-0.4H_V} = p_V R^2 / (664.4)^2 \tag{4.14}$$

After the completion of the Monte Carlo simulations, the solar magnitude used among my collaborators was revised to V_S = -26.74 (M. Müller, personal communication, August 7, 2008), leading to a geometric albedo of:

$$p_V = (671.3/R)^2 * 10^{-0.4H_V} \tag{4.15}$$

Any new work should use the revised constant of 671.3.

Once a set of radii and albedos consistent with the absolute magnitude were constructed, they were input into the STM along with the distance from the Sun to the object and the distance from the object to the *SST*, a thermal emissivity of 0.9, the observed wavelengths (23.68 μm and 71.42 μm), and a fixed beaming factor, η, of 1.94. This value for η is the upper 1 σ value of the combined set of η values from detected Classical KBOs (not including inner Classicals) in P3542 and the η values from Classical KBOs directly from Stansberry et al. (2008) (not the recalculated values determined in Brucker et al. 2009). For each radius-albedo pair, the STM yields the flux one would expect to observe in each wavelength under the conditions provided. The reported upper limit on the radius is the radius at which the STM flux at 70 μm exceeds the upper 1 σ detection level of the observed flux. The reported lower limit on the albedo is the albedo that corresponds to that radius as determined via Equation 4.13.

The STM was used either to constrain or determine the radius and albedo for each of the TNOs in the P3542 and P50540 samples. The results of the thermal modeling can be found in the next chapter.

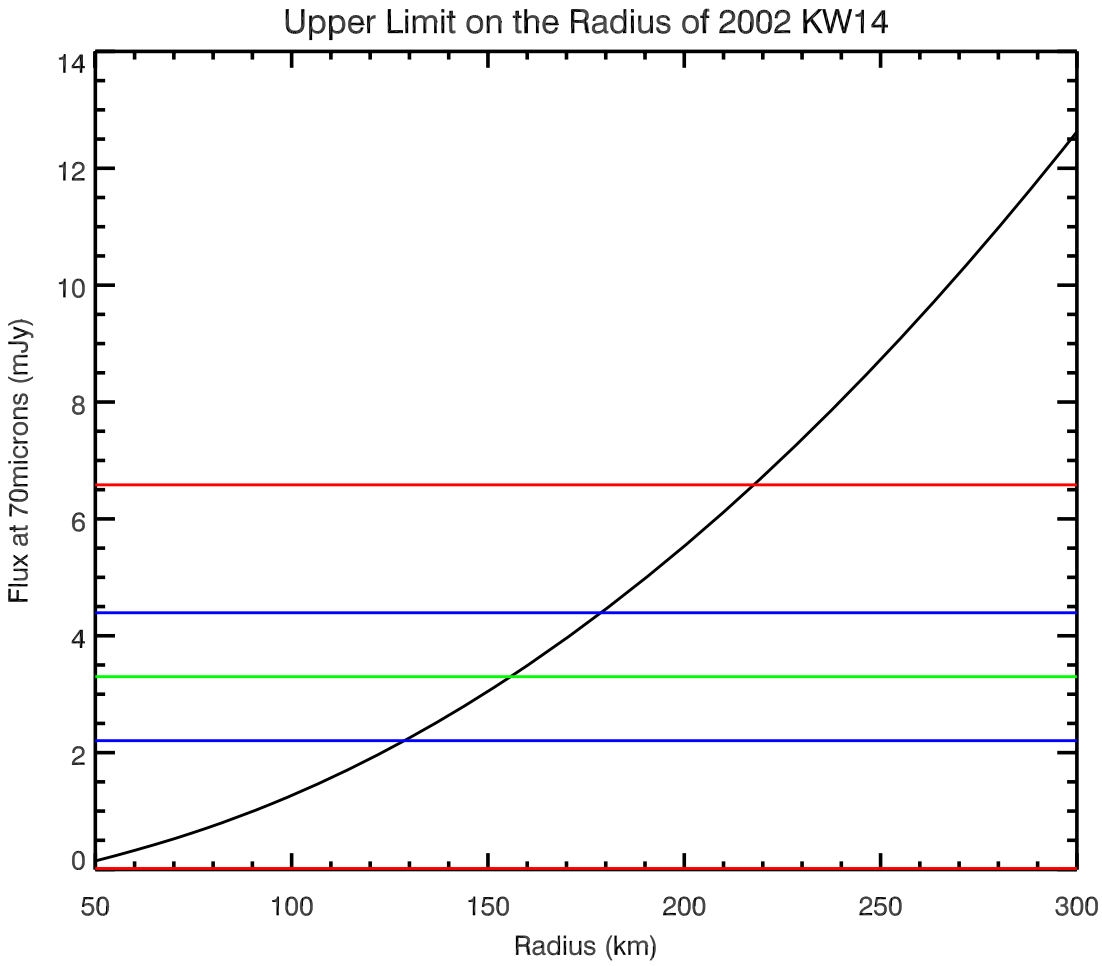

Figure 4.5. The upper limit on the radius for 2002 KW_{14} occurs at the point where the black line crosses the upper blue line. The black line represents the modeled flux from the STM at a series of radii. The green line represents the observed flux at 70 μm, the blue lines represent the flux at the upper and lower 1 σ uncertainty, and the red lines represent the flux at the upper and lower 3 σ uncertainty.

Chapter 5

Results and Trends

5.1 Results for P3542 and Comparison to other Classical KBO Data

All fifteen TNOs successfully observed for P3542 were modeled with the STM to derive geometric albedos and radii from their thermal emissions (Table 5.1). The Neptune Trojan, 2001 QR_{322}, and the 3:2 Resonant KBO, 2003 QX_{111}, both have low albedos. The six hot Classicals in the sample have low to moderate albedos. 2001 KA_{77}, 2002 GJ_{32}, and 1996 TS_{66} have geometric albedos less than 0.15. The albedo of Quaoar is higher at 0.17. For the four detected hot Classicals, the mean albedo is 0.11, the median albedo is 0.12, and the standard deviation is 0.06. 2002 KW_{14} was not detected in the 24 μm final image and Altjira was not detected in the 70 μm final image. 2002 KW_{14} may have a low albedo. It is unique as the only TNO in P3542 detected at 70 μm but not at 24 μm. Altjira, having the lowest inclination of the hot Classicals (5.5º), may have a high albedo and may actually belong to the cold Classical population. Recall that the hot and cold Classical populations overlap in inclination space so the preliminary classifications that we have assigned are not necessarily accurate and individual membership should be evaluated probabilistically. Four of the five cold Classicals were not detected at 70 μm. All five have albedos greater than 0.13. The only cold Classical object with a dual wavelength detection was 2001 QD_{298} with a moderate albedo of $0.18 \pm^{0.17}_{0.08}$. The inner Classicals in the sample both have high albedos. 2002 KX_{14} has an albedo of $0.60 \pm^{0.36}_{0.23}$ and 2001 QT_{322} was not detected at 70 μm and has an albedo greater than 0.21.

Table 5.1 Results for *Spitzer Space Telescope* Cycle 1 Program 3542 Targets (Brucker et al. 2009, Table 4)

Designation	24 μm: Flux[a] (mJy)	70 μm: Flux[a] (mJy)	T[b] (K)	p_V[c]	Radius[c] (km)	η[c]
Hot Classicals						
2001 KA_{77}	0.0077 ± 0.0023	4.12 ± 0.77	47	$0.0250 \pm^{0.0095}_{0.0080}$	$317 \pm^{67}_{46}$	$2.80 \pm^{0.51}_{0.39}$
2002 GJ_{32}	0.0101 ± 0.0060	1.45 ± 0.86	51	$0.12 \pm^{0.14}_{0.06}$	$112 \pm^{44}_{35}$	$1.78 \pm^{0.74}_{0.60}$
1996 TS_{66}	0.0935 ± 0.0048	2.99 ± 0.90	55	$0.120 \pm^{0.072}_{0.047}$	$97 \pm^{27}_{19}$	$0.96 \pm^{0.27}_{0.18}$
Quaoar[d,e]	0.2241 ± 0.0056	24.91 ± 2.14	51	$0.172 \pm^{0.055}_{0.036}$	$454 \pm^{56}_{59}$	$1.51 \pm^{0.18}_{0.20}$
2002 KW_{14}	< 0.0060	3.30 ± 1.09	54	> 0.05	< 180	--
Altjira[d]	0.0167 ± 0.0025	< 0.85	49	> 0.10	< 100	--
Cold Classicals						
2000 OK_{67}	0.0305 ± 0.0066	< 0.82	53	> 0.16	< 80	--
2002 VT_{130}	0.0793 ± 0.0052	< 0.98	51	> 0.13	< 120	--
2001 QD_{298}	0.0487 ± 0.0059	1.59 ± 0.95	53	$0.18 \pm^{0.17}_{0.08}$	$73 \pm^{27}_{21}$	$0.79 \pm^{0.28}_{0.26}$
2001 RZ_{143}[d]	0.0460 ± 0.0074	< 0.66	52	> 0.23	< 80	--
2001 QS_{322}	< 0.0035	< 0.97	52	> 0.15	< 100	--
Inner Classicals						
2001 QT_{322}	0.0405 ± 0.0052	< 0.98	57	> 0.21	< 80	--
2002 KX_{14}	0.0786 ± 0.0079	2.22 ± 1.44	54	$0.60 \pm^{0.36}_{0.23}$	$90 \pm^{25}_{19}$	$0.61 \pm^{0.28}_{0.28}$
Resonant KBOs						
2001 QR_{322}	0.1684 ± 0.0099	3.01 ± 0.53	66	$0.058 \pm^{0.029}_{0.016}$	$66 \pm^{12}_{12}$	$1.16 \pm^{0.21}_{0.22}$
2003 QX_{111}	0.0189 ± 0.0070	4.43 ± 1.25	54	$0.018 \pm^{0.017}_{0.009}$	$217 \pm^{66}_{43}$	$2.97 \pm^{0.74}_{0.54}$

[a]Color-corrected fluxes, uncertainties, and limits. Uncertainties and limits stated are the 1σ measurement uncertainties and do not include the MIPS calibration uncertainty here.
[b]These approximate interpolated temperatures are a tool for calculating the color correction and are not to be used for thermal modeling.
[c]1 σ uncertainties and limits from the STM modeling. In this paper, η encompasses physical complexities not included in the STM.
[d]Known binary objects (Noll et al. 2008a). The radii presented are effective radii such that the projected area is the same as that given by the object and its companion assuming they have equal albedos.
[e]Known presence of rotational lightcurve (Ortiz et al. 2003, Sheppard et al. 2008). The radius presented is an effective radius assuming a spherical body.

Many of the low inclination Classical KBOs were not detected in the 70 μm channel. Their infrared thermal emissions were fainter than expected. Consequently, the allotted exposure times were not long enough to detect their flux. In other words, for

their given visual absolute magnitudes, they have higher albedos and smaller radii than expected. With a higher albedo, an object absorbs less light to reradiate thermally. With a smaller radius, there is also less surface area to absorb light and from which thermal emission radiates. If the low inclination cold Classicals had albedos comparable to the hot Classicals, then MIPS would have detected them with the allocated exposure times.

The results from the P3542 sample support the hypothesis that small dynamically cold Classical KBOs have higher albedos than small dynamically hot Classical KBOs (Figure 5.1). This hypothesis was drawn from the results of Grundy et al. (2005) and strengthened by Stansberry et al. (2008) as detailed in Table 5.2.

Statistical analysis shows whether or not a correlation actually exists for our sample and for the combined sample of hot and cold Classicals from our study and the literature. The inner Classicals are not included in this analysis because a new study of colors by Romanishin et al. (2008, 2009) suggests that inner and cold Classicals have less than a 0.1% likelihood of being drawn from the same parent distribution of color indices (Romanishin et al. 2009). The inner Classical population in their sample contains both red and gray objects unlike the cold Classical population which is red.

Statistical analysis was performed to assess the null hypothesis that albedo is unrelated to inclination. Since the functional form of any dependence that might be found was not known *a priori*, the rank correlation tests Kendall's tau test and the Spearman rank-order test were employed (Press et al. 1992). The Kendall's tau test is attractive because it is non-parametric and does not assume a functional form for correlations. For the purpose of the statistical tests, the lower limit was designated as the albedo for those objects with only a lower limit.

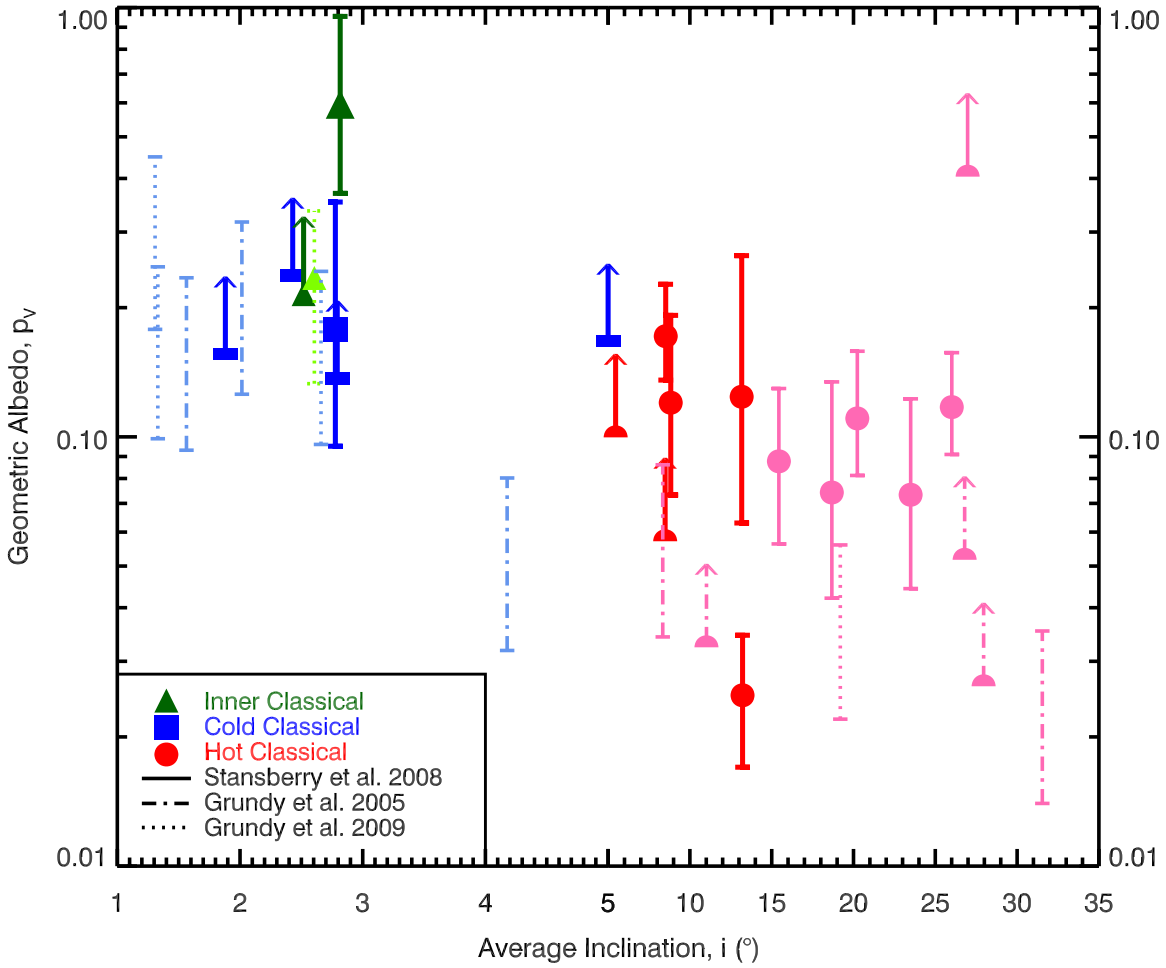

Figure 5.1. The visual geometric albedo, p_V, is plotted versus the 10 Myr mean inclination, i, with respect to the invariable plane. The x-axis changes scale below 5° to magnify the low inclination region. All included objects are Classical according to Gladman et al. (2008). Our thirteen Classical objects are plotted in red, blue, and green. Objects with 70 μm non-detections are represented by arrows with bars (or a triangle) located at lower limits. Comparison objects from other studies are plotted in pink, light blue, and light green. Pastel-colored objects with solid error bars are from Stansberry et al. (2008). The dot-dashed lines are constraints from Grundy et al. (2005) converted to V albedos using colors found in the literature. The dotted lines are constraints from Grundy et al. (2009). Objects with only a lower limit are represented by an arrow with a half-symbol at the lower limit.

The null hypothesis was rejected for the combined sample of non-inner Classical KBOs as listed in Tables 5.1 and 5.2. Albedo is correlated with inclination. The Spearman rank correlation coefficient is -0.608 with a probability of 0.000465 that the albedo and inclination are unrelated and a 3.50 σ confidence that they are related (Brucker et al. 2009). The Kendall's tau is -0.471 with a probability of 0.000334 that the

albedo and inclination are unrelated and a 3.59 σ confidence that they are related (Brucker et al. 2009). The results of the rank correlation tests from P3542 alone and the results of the rank correlation tests on data from the literature alone were not significant enough to reach the 3 σ confidence threshold.

The Spearman rank-order test and the Kendall's tau test show that there exists a correlation between albedo and inclination for non-inner Classical KBOs. A two-tailed Kolmogorov-Smirnov test (K-S test; Press et al. 1992) was used to explore the dependence between albedo and inclination by distinguishing whether or not the two subsamples are drawn from the same parent distribution. We set an inclination boundary such that all objects in one subsample have inclinations less than the inclinations of the objects in the other subsample. We shifted the inclination boundary to assess many sets of subsamples. For inclination boundaries between 2.4º and 8.8º, the two subsamples do not come from the same parent distribution with a confidence at or above 3 σ. In other words, the inclination at which an object has equal probability of belonging to either sample resides somewhere between 2.4º and 8.8º. This supports our initial adoption of 5º as an arbitrary break between dynamically hot and cold KBOs. Others have reached similar conclusions based on color indices (Gulbis et al. 2006) and binarity rates (Noll et al. 2008a). In contradiction, Peixinho et al. (2008) assert a break in inclination at 12º for color indices. However, the relationship between albedo and color may differ from the relationship between albedo and inclination. It is important to note that all of the Classical KBOs with reported V-R colors in the P3542 sample are red. Most of the blue objects in Figure 5.11 are classified as Scattered-Near in the DES system.

Table 5.2 Other Small Classical KBOs with Albedo and Radius Constraints (Brucker et al. 2009, Table 6)

Number[a]	Provisional Designation	DES type[b]	i[c] (°)	V-R	p_V	Radius (km)	Ref.	Name
Hot Classicals								
55636	2002 TX_{300}[z]	SN	26.98	0.363±0.018[i,j,k]	> 0.41	< 210	f	
55565	2002 AW_{197}	SN	26.01	0.62±0.03[l]	$0.115 \pm^{0.041}_{0.025}$	$371 \pm^{49}_{52}$	f	
90568	2004 GV_9	SN	23.49	0.52±0.03[m]	$0.073 \pm^{0.049}_{0.029}$	$342 \pm^{34}_{37}$	f	
55637	2002 UX_{25}[d]	SN	20.23	0.56±0.02[m]	$0.111 \pm^{0.049}_{0.030}$	$340 \pm^{53}_{54}$	f	
	2002 MS_4	SN	18.68	0.38±0.02[m]	$0.073 \pm^{0.058}_{0.032}$	$365 \pm^{59}_{60}$	f	
20000	2000 WR_{106}	C	15.44	0.615±0.014[n]	$0.088 \pm^{0.042}_{0.031}$	$357 \pm^{89}_{64}$	f	Varuna
50000	2002 LM_{60}[d]	C	8.52	0.646±0.012[k,l]	$0.206 \pm^{0.093}_{0.066}$	$415 \pm^{89}_{71}$	f	Quaoar
Inner Classicals								
119951	2002 KX_{14}	C	2.82	0.621±0.022[o,p]	> 0.10	< 220	f	

[a]Objects are sorted by Gladman et al. (2008) orbital type and decreasing inclination with a break at 5° to separate the overlapping hot and cold Classical KBO populations. Makemake and Haumea were not included as they are dwarf planets (larger, icier, and distinct).
[b]SN – Scattered-Near, C – Classical, UN – Unclassified in Gladman et al. (2008).
[c]Average inclinations are with respect to the invariable plane.
[d]Known binary objects (Noll et al. 2008a).
[e]For binary objects, the minimum and maximum radius stated are for the brighter component assuming that the primary and secondary have equal albedos.
[f]Albedo and radius results from Stansberry et al. (2008) have been remodeled from their Spitzer flux measurements using our method.
[g]Albedo and radius results from Grundy et al. (2005) converted from p_R to p_V. If the object is designated binary, then its albedo and radius were determined from the binary system mass. If the object is not designated binary, then its albedo and radius were determined from thermal radiometry.
[h]Albedo and radius results from Grundy et al. (2009) as determined from the binary system mass.
[i]Doressoundiram et al. (2005).
[j]Ortiz et al. (2004).
[k]Tegler et al. (2003).
[l]Fornasier et al. (2004).
[m]Tegler et al. http://www.physics.nau.edu/~tegler/research/survey.htm
[n]Doressoundiram et al. (2002).

Table 5.2 Other Small Classical KBOs with Albedo and Radius Constraints, cont'd. (Brucker et al. 2009, Table 6)

Number[a]	Provisional Designation	DES type[b]	i[c] (°)	V-R	p_V		Radius (km)		Ref.	Name
					Min.	Max.	Min.[e]	Max.[e]		
Hot Classicals										
	2001 QC_{298}[d]	SN	31.54	--	0.014	0.035	94	150	g	
19308	1996 TO_{66}[z]	SN	27.95	0.397±0.028[q,r,s,t]	0.027	1	0	449	g	
24835	1995 SM_{55}[z]	SN	26.79	0.395±0.026[n,r,s,u]	0.053	1	0	350	g	
	2004 PB_{108}[d]	SN (UN)	19.19	--	0.02	0.06	99	160	h	
19521	1998 WH_{24}	C	11.01	0.623±0.032[n,r,u,v]	0.033	1	0	372	g	Chaos
	1998 WW_{31}[d]	C	8.34	--	0.034	0.086	59	93	g	
Cold Classicals										
88611	2001 QT_{297}[d]	C	4.18	0.61±0.04[w]	0.032	0.080	65	103	g	Teharonhiawako
	2001 XR_{254}[d]	C	2.66	--	0.10	0.24	68	110	h	
58534	1997 CQ_{29}[d]	C	2.02	0.667±0.094[r,s,t,x]	0.126	0.317	30	47	g	Logos
66652	1999 RZ_{253}[d]	C	1.56	0.688±0.094[u]	0.093	0.235	66	104	g	Borasisi
134860	2000 OJ_{67}[d]	C	1.33	0.673±0.046[n]	0.10	0.25	57	90	h	
	2003 TJ_{58}[d]	C (UN)	1.31	--	0.18	0.45	26	42	h	
Inner Classicals										
	1999 OJ_4[d]	C	2.61	0.668±0.072[y]	0.13	0.34	29	47	h	

[o]The object 2002 KX_{14} was observed in the V and R bands by S. Sheppard using filters based on the Johnson system with four 300 second images in each filter at the du Pont 2.5 meter telescope on UT July 19, 2007 with the Tek5 CCD (0.259" $pixel^{-1}$).
[p]Romanishin et al. (2009).
[q]Barucci et al. (1999).
[r]Boehnhardt et al. (2001).
[s]Gil-Hutton and Licandro (2001).
[t]Jewitt and Luu (2001).
[u]Delsanti et al. (2001).
[v]Barucci et al. (2000).
[w]Osip et al. (2003).
[x]Stephens et al. (2003).
[y]Hainaut and Delsanti (2002).
[z]Member of the Haumea collisional family (Brown et al. 2007).

Jewitt et al. (2007) have detected a correlation between color and Tisserand parameter with respect to Neptune. This was discussed by Peixinho (2008) and related to a proposed inclination-color break at 12º (Peixinho et al. 2008). I did not test whether or not a correlation exists between the geometric albedo and the Tisserand parameter since our sample covers only a very narrow range of Tisserand parameters (Table 2.1) which may not be representative of the population distribution.

A more appropriate method for conducting correlation statistics involving lower limits is to apply survival analysis. I employed the generalized Kendall's Tau function of ASURV from the Pennsylvania State University Center for Astrostatistics software archive (Feigelson and Nelson 1985, Isobe et al. 1986, LaValley et al. 1990). ASURV computes statistics on censored data (data with upper and/or lower limits). I did not use the Spearman's Rho function because it is not accurate for sample sizes less than 30.

For our sample of hot and cold Classicals, with the generalized Kendall's Tau function, the probability that albedo and inclination are correlated is 0.9925, a 2.674 σ confidence. Excluding Quaoar from this sample (since it is a moderately large KBO), the probability becomes 0.9845, a 2.420 σ confidence. For the sample of hot and cold Classicals from the literature (excluding Quaoar), the probability that albedo and inclination are correlated is 0.7456 with only a 1.140 σ confidence. For the combined sample of our objects and the objects from the literature, the probability that albedo and inclination are correlated is 0.0.9967 at a 2.938 σ confidence. For the combined sample excluding Quaoar, the probability is 0.9957 at a 2.855 σ confidence.

The KBOs that are members of the Haumea collisional family appear to be distinct from other KBOs. By excluding those objects, (24835) 1995 SM_{55}, (19308) 1996

TO_{66}, and (55636) 2002 TX_{300}, the probability that albedo and inclination are correlated for the literature sample becomes 0.9456 at a 1.924 σ confidence. The probability for the combined sample becomes 0.9997 at a 3.616 σ confidence and the probability for the combined sample excluding Quaoar becomes 0.9996 at a 3.540 σ confidence.

Two of the Classical KBOs in our sample have been previously studied in the infrared. The first, Quaoar, is a moderately large bright hot Classical. Stansberry et al. (2008) also observed Quaoar using MIPS. Our results, using a similar modeling strategy, agree with their results (Tables 5.1 and 5.2). This shows that the results from *SST* observations and our procedures are repeatable for TNOs at moderate S/N.

Brown and Trujillo (2004) also observed Quaoar with the *Hubble Space Telescope* (*HST*) High Resolution Camera (HRC). They concluded that the radius is $630 \pm^{95}_{95}$ km compared to our effective radius of $454 \pm^{56}_{59}$ km. They determined $p_R = 0.092 \pm^{0.036}_{0.023}$ and $p_B = 0.101 \pm^{0.039}_{0.024}$ whereas our value for p_V is $0.172 \pm^{0.055}_{0.036}$. The differences between our results and the results of Brown and Trujillo have several possible explanations. One possible explanation is a magnitude effect from the lightcurve. Our twelve observations were spaced out in time such that, together, they sample Quaoar's period phase space both for the single-peaked period of 8.8 h and the double-peaked period of 17.7 h (Ortiz et al. 2003). Our final flux measurements average over the changes in magnitude of the lightcurve. Brown and Trujillo's *HST* observations all occurred within a single *HST* orbit and hence they did not sample the lightcurve well; although, we do not know at which phase their observations occurred. In addition to lightcurve effects, our results may be affected by the use of the STM instead of a more realistic thermal model. Brown and Trujillo's results may be affected by the center-to-limb profile used in their modeling.

An independent third measurement, for example via a stellar occultation, could resolve the discrepancies.

It is reasonable that Quaoar has a higher albedo than the other detected hot Classicals. With its larger size, Quaoar is expected to be icier than smaller KBOs. With a radius of 454 km, its photometric and spectroscopic properties appear to lie in a transition zone between those of dwarf planets and small KBOs. According to Schaller and Brown (2007a), who used the diameter calculated by Brown and Trujillo (2004), Quaoar is large enough to have retained some volatile ices over the age of the solar system, specifically methane and carbon monoxide. In fact, Jewitt and Luu (2004) detected NIR spectral absorption features which they attributed to crystalline water ice and ammonia hydrate. Cook (2007) also identified water ice, ammonia hydrate, and additional unidentified substance(s). Schaller and Brown (2007b) concluded that the surface contains water ice, methane, and ethane from their observations (they attributed the ammonia hydrate feature of Jewitt and Luu to one of several methane features). Guilbert et al. (2009) also attributed observed absorption features to water ice and methane.

The second Classical KBO that has been previously observed with *SST* is the inner Classical 2002 KX_{14}. Stansberry et al. (2008) observed 2002 KX_{14} with MIPS but did not detect it in either wavelength. From P3542, we determined an albedo of $0.60 \pm^{0.36}_{0.23}$ and a radius of $90 \pm^{25}_{19}$ km (Brucker et al. 2009) which is consistent with the lax constraints determined by Stansberry et al. (2008) of a lower limit on the albedo of 0.088

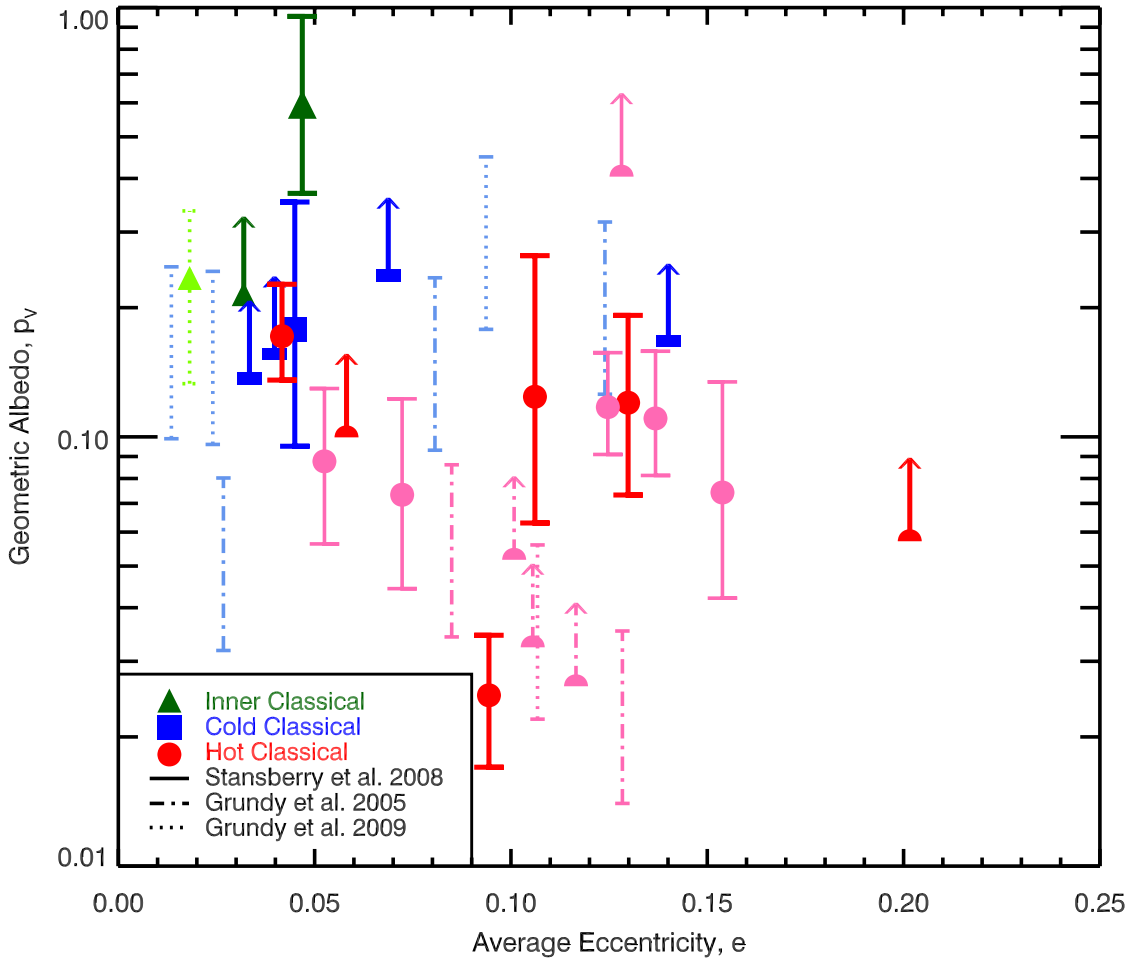

Figure 5.2. The visual geometric albedo, p_V, is plotted versus the 10 Myr mean eccentricity, e. The symbols are as in Figure 5.1.

and an upper limit on the radius of 232 km.

Similarly to Figure 5.1, most of the objects with low eccentricity have high albedos. Eccentricity and inclination are the parameters that determine whether a Classical KBO is considered dynamically hot or dynamically cold. The behavior of albedo with respect to eccentricity conforms to our expectations.

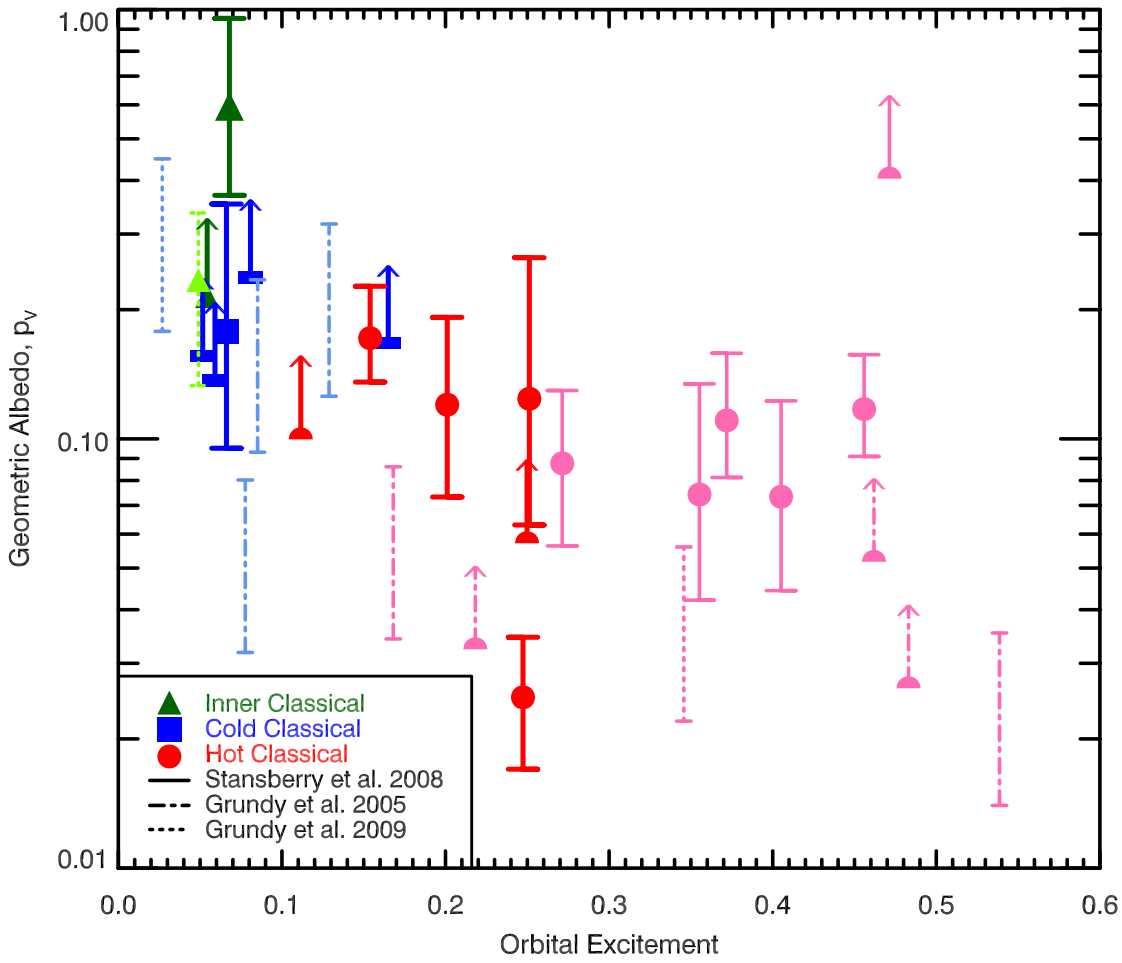

Figure 5.3. The visual geometric albedo, p_V, is plotted versus the 10 Myr mean orbital excitation given by $\sqrt{\sin(i)^2 + e^2}$. The symbols are as in Figure 5.1.

The orbital excitation is another way to express the degree to which an object has been dynamically excited (a numerical expression of overall dynamical hot- and coldness). The increase in albedo with decreasing orbital excitation is patently obvious. This plot neatly sorts the objects by DES orbital classification (Elliot et al. 2005) where the cold Classicals are blue, the hot Classicals are red, and the Scattered-Near KBOs are pink.

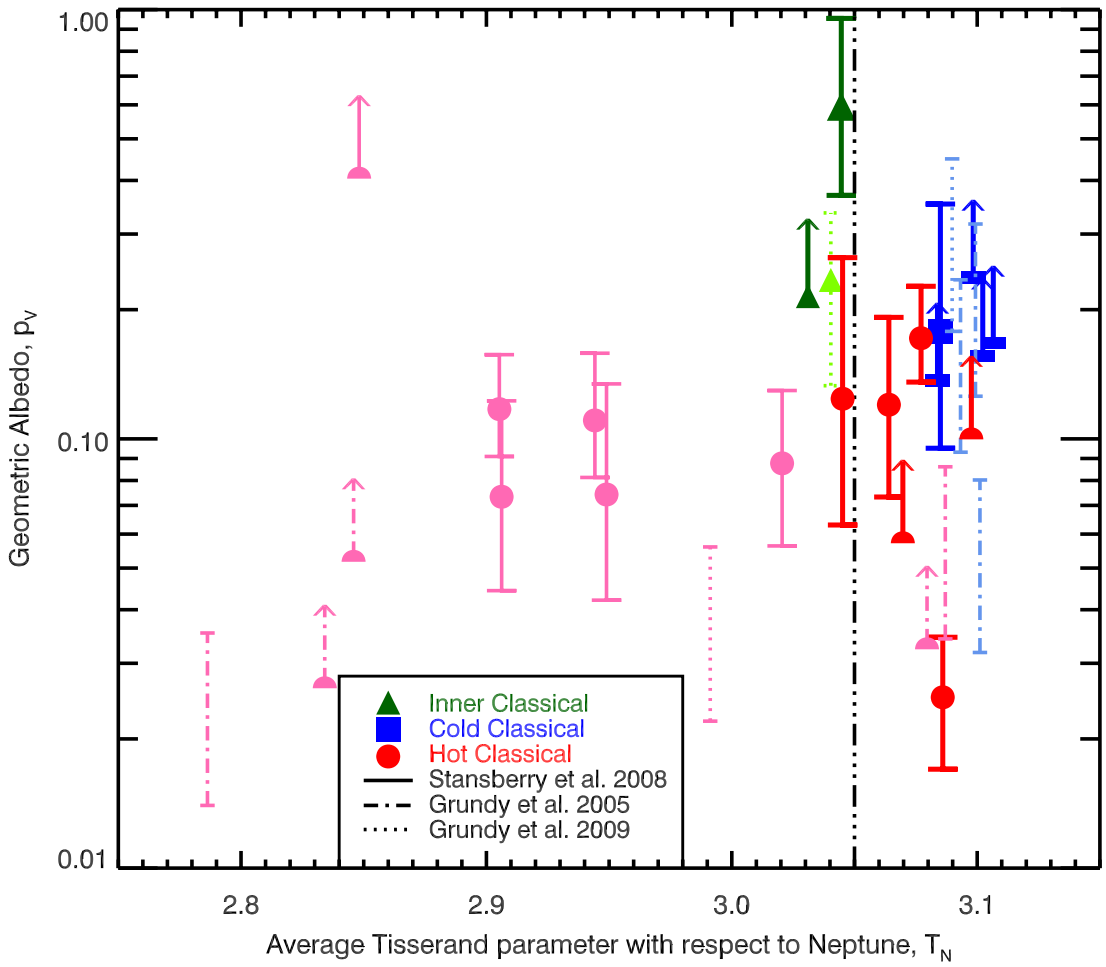

Figure 5.4. The visual geometric albedo, p_V, is plotted versus the 10 Myr mean Tisserand parameter with respect to Neptune, T_N. The symbols are as in Figure 5.1. The black vertical dot-dot-dashed line is placed at T_N =3.05, the inclination-Tisserand parameter break noted by Peixinho (2008). The outlying hot Classical from P3542 is 2001 KA_{77} which has the largest inclination in that sample.

The Tisserand parameter with respect to Neptune describes an object's interaction or lack thereof with said planet. Peixinho (2008) has explored the relationship between the Tisserand parameter and color and found a slight correlation. There may be a correlation between albedo and T_N with the albedo increasing with increasing T_N; but, it is not obvious from our data as shown in Figure 5.4.

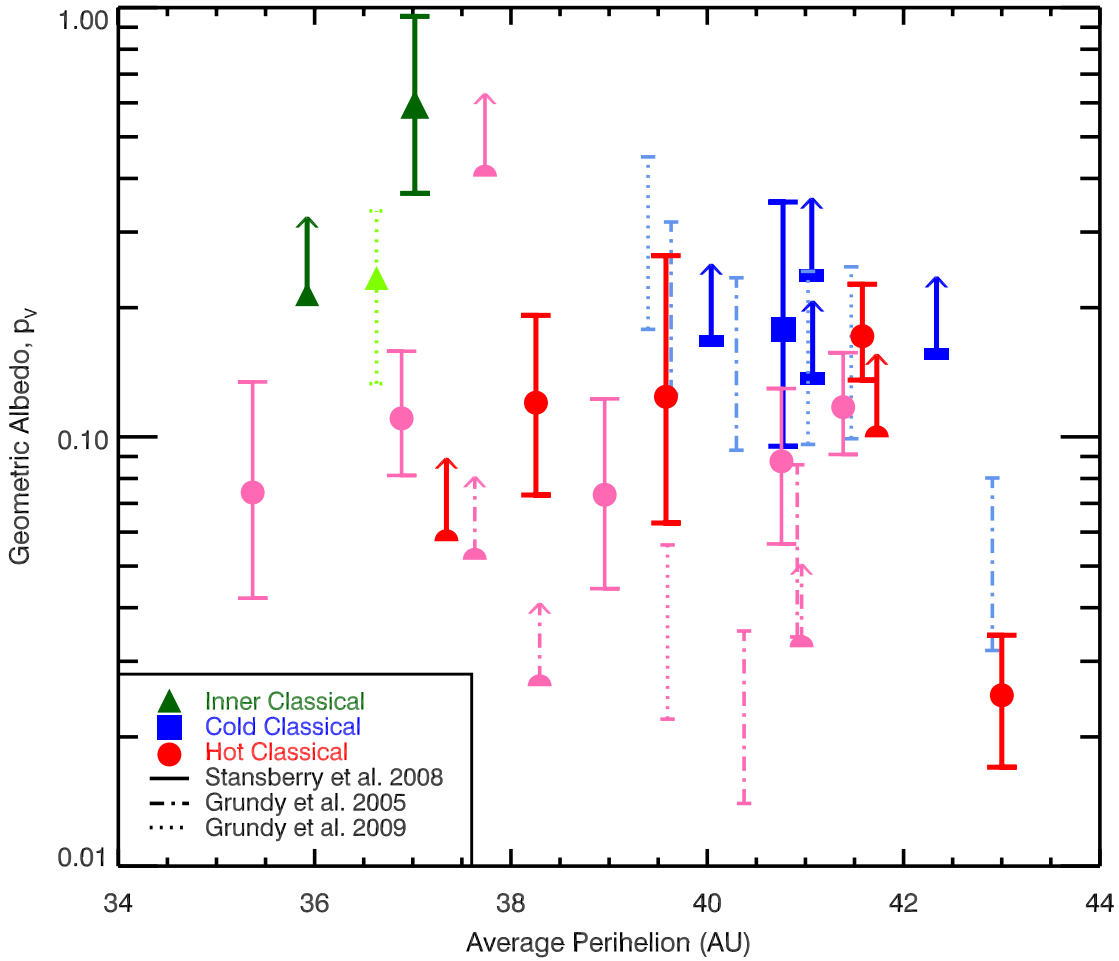

Figure 5.5. The visual geometric albedo, p_V, is plotted versus the 10 Myr mean perihelion, q. The symbols are as in Figure 5.1.

As illustrated in Figure 5.5, there is no obvious trend in albedo with perihelion (a possible slight increase in albedo with increasing perihelion could be caused by increased retention of surface ices). The cold Classicals have a small range of perihelia as opposed to the hot Classicals which have a variety of perihelia. This is partly due to the inclusion of DES Scattered-Near KBOs.

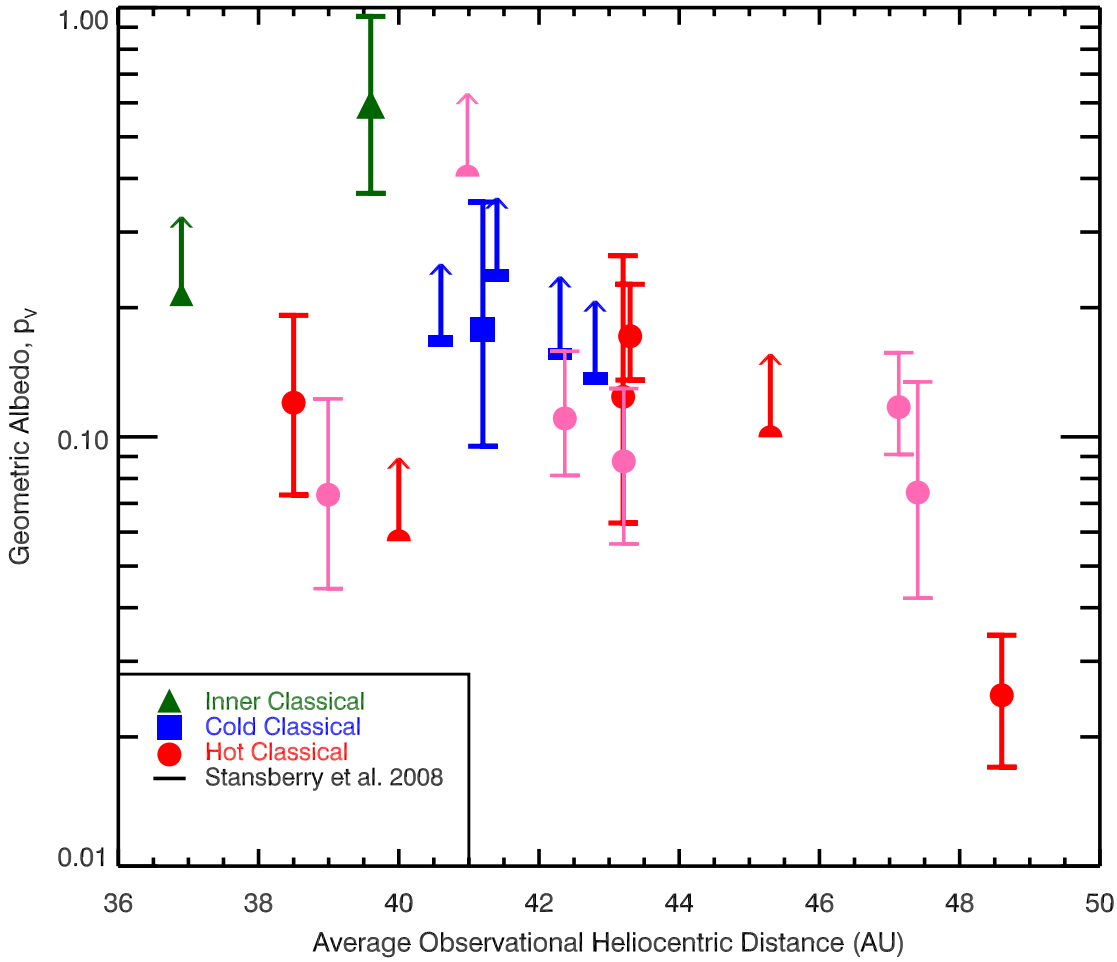

Figure 5.6. The visual geometric albedo, p_V, is plotted versus the average heliocentric distance, r, at the time of the observations. The symbols are as in Figure 5.1.

The objects in our sample were chosen based on their magnitude to allow for reasonable exposure times since TNOs were at the faint end of *SST*'s sensitivity range. This created an observational bias apparent in Figures 5.6 – 5.9. It appears that albedo decreases with increasing distance from the Sun (heliocentric distance, semimajor axis, and aphelion) and with increasing radius. The observed relationship between albedo and solar distance may include a real component; however, the cause is yet unknown.

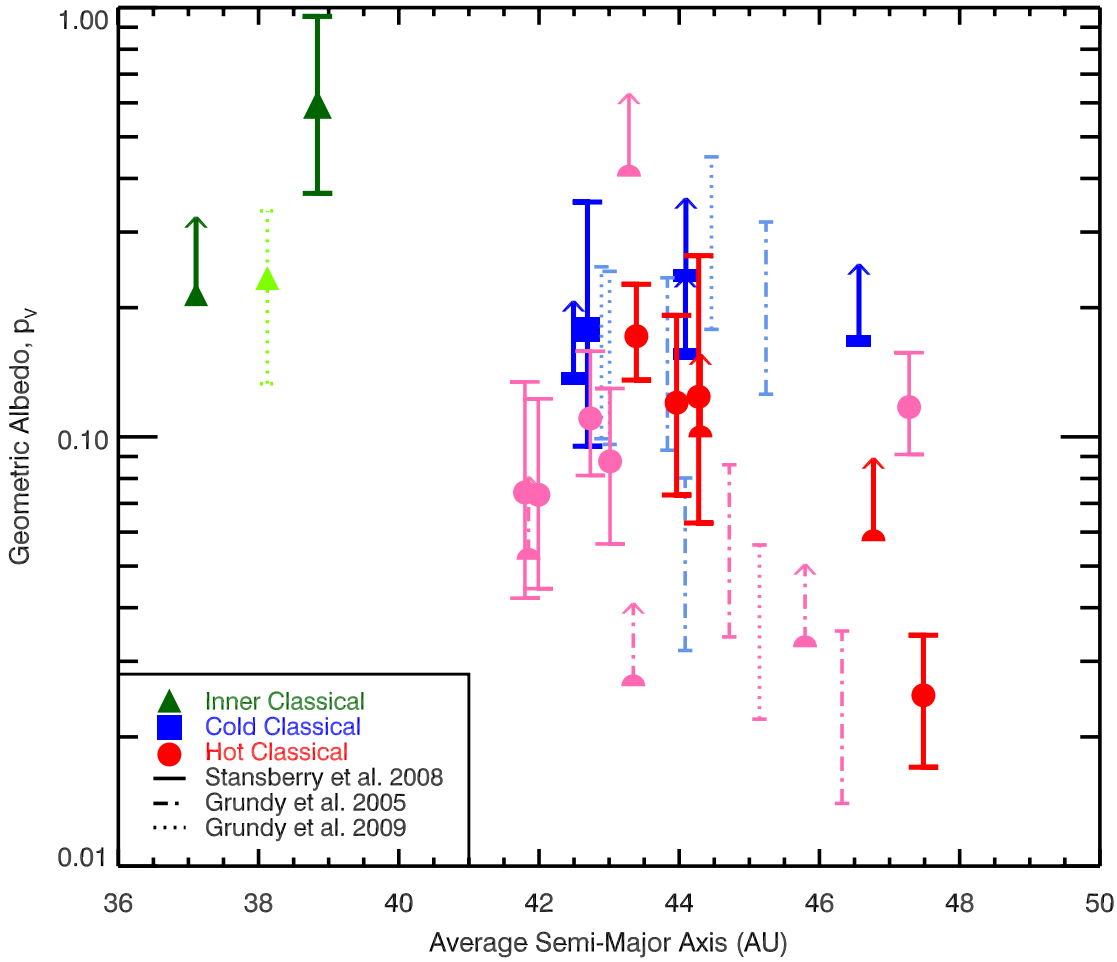

Figure 5.7. The visual geometric albedo, p_V, is plotted versus the 10 Myr mean semimajor axis, a. The symbols are as in Figure 5.1.

In general, for two objects of similar magnitude, the object that is farther away is larger and/or more reflective. If an object is larger, then it may still be detectible with a lower albedo. As seen in Figure 5.7, the objects with smaller semimajor axes have higher albedos. They are closer, more reflective, and smaller.

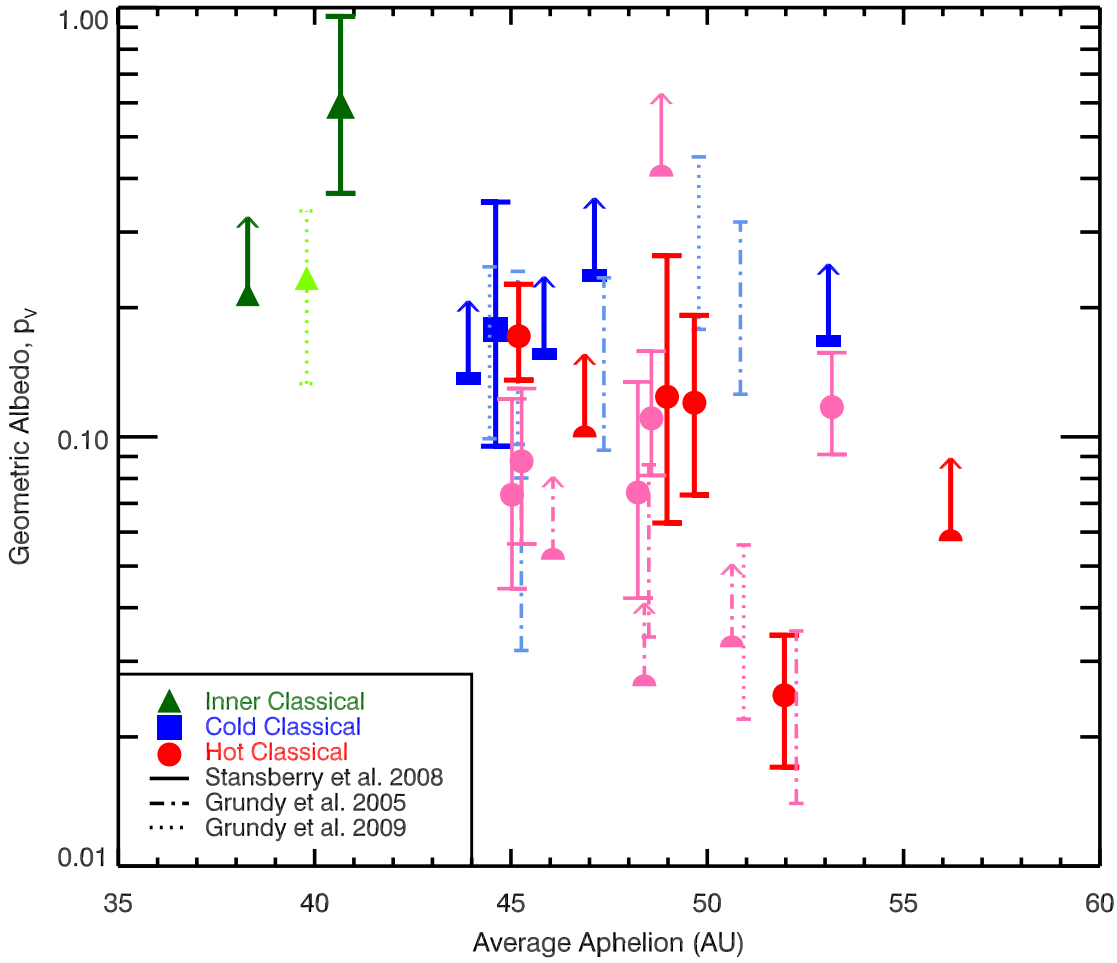

Figure 5.8. The visual geometric albedo, p_V, is plotted versus the 10 Myr mean aphelion, Q. The symbols are as in Figure 5.1.

There may be a correlation between albedo and aphelion in addition to the selection bias and discovery bias. Objects that travel farther out in the solar system are exposed to more cosmic rays and pickup ions from the Very Local Interstellar Medium than objects with smaller aphelia (Cooper 2003). Energetic particles alter complex organic compounds near the surface. The surface becomes redder and less reflective and eventually gray with very low albedo. This alteration competes with impact gardening and sputtering which draw forth pristine material from below the surface (Cooper 2003).

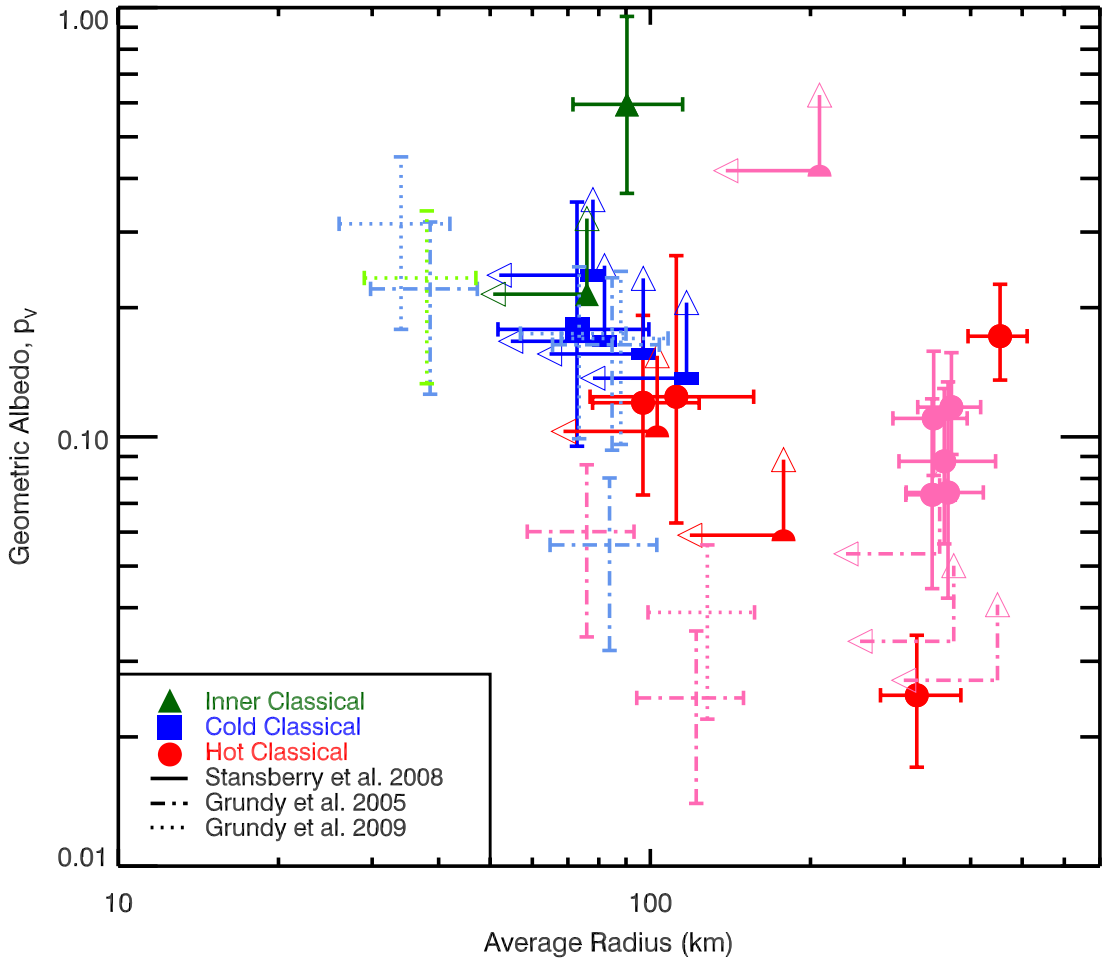

Figure 5.9. The visual geometric albedo, p_V, is plotted versus the radius, R. The symbols are as in Figure 5.1.

The selection bias for objects with similar absolute magnitudes is most clearly illustrated by Figure 5.9 in which the objects from our sample with high albedos have smaller radii than the objects with low albedos. Quaoar (the hot Classical KBO in Figure 5.9 with the largest radius) does not fit this pattern since it was selected for method validation as opposed to investigation and its radius can be independently verified through the *HST* observations conducted by Brown and Trujillo (2004).

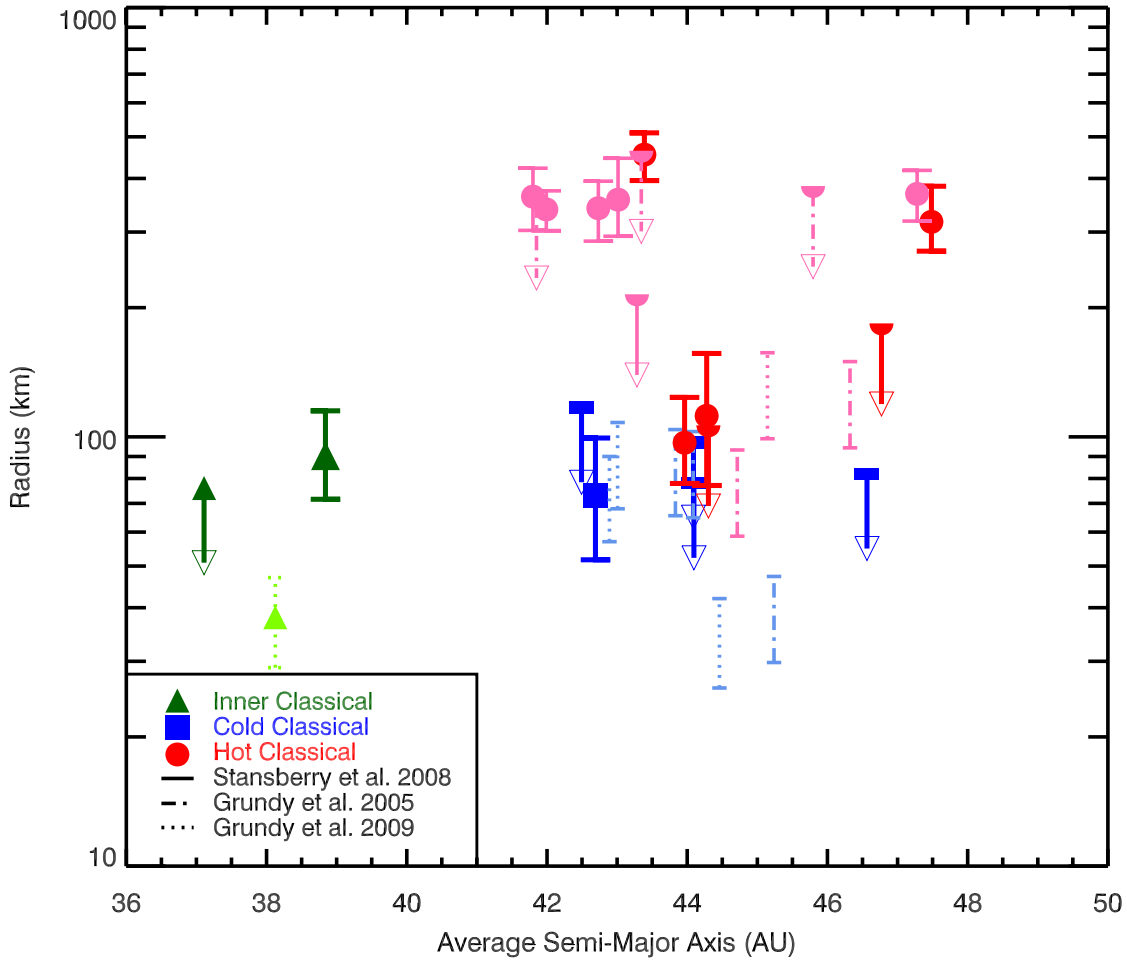

Figure 5.10. The radius, *R*, is plotted versus the 10 Myr mean semimajor axis, *a*. The symbols are as in Figure 5.1.

There is no obvious trend in radius with semimajor axis. Again, most of the cold Classicals have similarly-sized radii while the hot Classicals have a range of radii. In Figure 5.10, there almost appear to be two distinct groups by radius at 100 km and 300 km. However, this is most probably due to selection bias and small sample size. The sample was drawn from the brightest dynamically hot and cold objects. As seen in Figure 1.5, the brightest cold Classicals are fainter than the brightest hot Classicals so one may extrapolate that the largest cold Classicals are smaller than the largest hot Classicals.

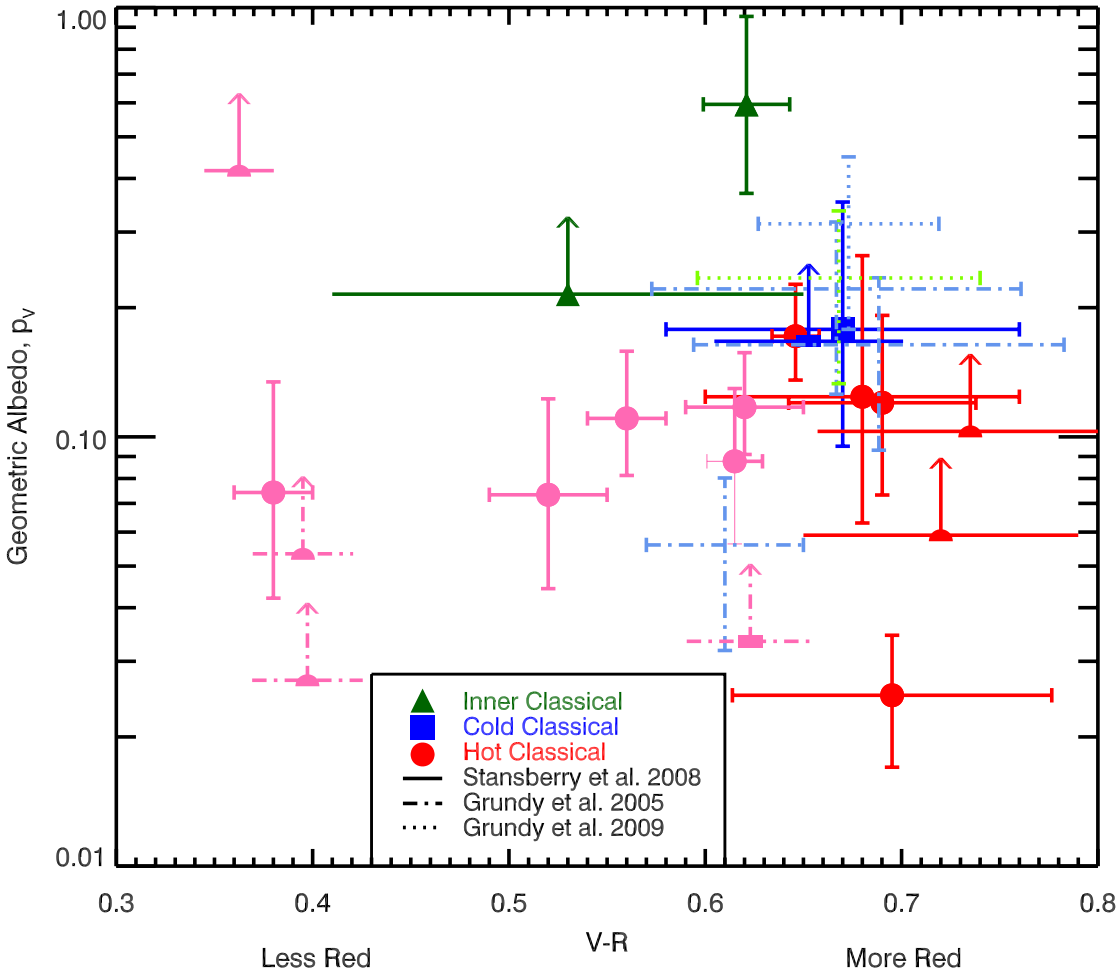

Figure 5.11. The visual geometric albedo, p_V, is plotted versus the V-R color index. The symbols are as in Figure 5.1.

The cold Classicals are red in V-R and the cold Classicals also have high albedos. Thus Figure 5.11 expectedly illustrates that cold Classical KBOs with high albedos are red. All of the Classicals in our sample with V-R colors (the red, dark green, and royal blue points with solid error bars) happen to be red in V-R. Hence red Classical KBOs may have low or high albedos. The objects in Figure 5.11 that are less red in V-R (pink points from Stansberry et al. (2008) and Grundy et al. (2005)) are mainly Scattered-Near KBOs in the DES system. This may be a function of space weathering or composition.

5.2 Results for P50540 and Comparison to other KBO Data

2001 KD_{77} is a 3:2 Resonant KBO chosen to explore the boundaries of the cold Classical Kuiper belt population. As previously discussed, it is the only object that was observed for P50540. Since it was not detected at 70 μm (Table 5.3), we cannot verify whether it has a high albedo like the cold Classicals or a moderate albedo like hot Classicals with lower inclinations. 2001 KD_{77} has a low inclination of 2.4º; this, in conjunction with its 70 μm non-detection, lends credence to the supposition that it has a high albedo.

Table 5.3 Results for *Spitzer Space Telescope* Cycle 5 Program P50540 Target

Designation	24 μm: Flux[a] (mJy)	70 μm: Flux[a] (mJy)	T[b] (K)	p_V[c]	Radius[c] (km)	η
Resonant KBO						
2001 KD_{77}	0.0713 ± 0.0180	< 2.33	58	> 0.11	< 106	--

[a]Color-corrected fluxes, uncertainties, and limits. Uncertainties and limits stated are the 1 σ measurement uncertainties and do not include the MIPS calibration uncertainty here.
[b]This approximate interpolated temperature is a tool for calculating the color correction and is not to be used for thermal modeling.
[c]Limits from the STM modeling.

In Section 5.1, the focus was on Classical KBOs. To put the Classical KBOs in context with other objects in the Kuiper belt, Figures 5.1 and 5.7 have been expanded (Figures 5.12 and 5.13) to include objects of other orbital types from P50540 (Table 5.3), from P3542 in Brucker et al. (2009) (Table 5.1), and in Stansberry et al. (2008), Grundy et al. (2005), and Grundy et al. (2009) (Tables 5.2 and 5.4).

Table 5.4 Other Small KBOs with Albedo and Radius Constraints

Number[a]	Provisional Designation	DES type[b]	i[c] (°)	V-R	p_V	Radius (km)	Ref.	Name
Scattering Disk								
15874	1996 TL_{66}[e]	SN	24.03	0.406±0.031[j,k,l]	$0.035 \pm^{0.018}_{0.014}$	$285 \pm^{80}_{52}$	f	
Resonant								
90482	2004 DW[d,e]	3:2	21.17	0.373±0.035[m]	$0.235 \pm^{0.047}_{0.049}$	$473 \pm^{41}_{41}$	f	Orcus
28978	2001 KX_{76}[e]	3:2	17.40	0.604±0.024[n,o,p]	$0.164 \pm^{0.084}_{0.061}$	$279 \pm^{73}_{52}$	f	Ixion
15820	1994 TB[e]	3:2	16.99	0.735±0.058[j,l,q,r,s]	> 0.0055	< 450	f	
84922	2003 VS_2[e]	3:2	16.14	0.59±0.02[t]	$0.054 \pm^{0.050}_{0.027}$	$353 \pm^{101}_{68}$	f	
208996	2003 AZ_{84}[d,e]	3:2	15.57	0.39±0.03[p,u]	$0.123 \pm^{0.042}_{0.027}$	$343 \pm^{45}_{47}$	f	
38628	2000 EB_{173}[e]	3:2	15.45	0.542±0.036[l,v,w]	$0.052 \pm^{0.011}_{0.009}$	$262 \pm^{18}_{18}$	f	Huya
47932	2000 GN_{171}[e]	3:2	10.26	0.622±0.038[p,w]	$0.053 \pm^{0.041}_{0.023}$	$161 \pm^{24}_{25}$	f	
47171	1999 TC_{36}[d,e]	3:2	6.66	0.688±0.010[k,p,r,v,x,y]	$0.072 \pm^{0.017}_{0.013}$	$207 \pm^{21}_{21}$	f	
26308	1998 SM_{165}[d]	2:1	13.08	0.603±0.032[r,z]	$0.079 \pm^{0.022}_{0.015}$	$140 \pm^{15}_{15}$	f	
84522	2002 TC_{302}	5:2	31.51	0.67±0.02[t]	$0.030 \pm^{0.029}_{0.015}$	$555 \pm^{174}_{120}$	f	
26375	1999 DE_9[e]	5:2	9.17	0.587±0.016[l,n,p,r,x]	$0.069 \pm^{0.018}_{0.012}$	$230 \pm^{23}_{25}$	f	
					Min. Max.	Min.[g] Max.[g]		
Resonant								
15875	1996 TP_{66}[d,e]	3:2	7.65	0.676±0.03111[j,k,l]	0.008 0.015	173 203	h	
15789	1993 SC[d,e]	3:2	5.89	0.731±0.080[j,l,q,s,aa]	0.008 0.041	112 252	h	
	2000 QL_{251}[d]	2:1	5.83	--	0.058 0.121	88 128	i	

[a]Objects are sorted by Gladman et al. (2008) orbital type and decreasing inclination. Makemake, Haumea, Eris, Sedna and Pluto were not included as they are dwarf planets (larger, icier, and differentiated; Sedna does not currently have dwarf planet status but may be similar in size).
[b]SN – Scattered-Near, #:# – Resonant.
[c]Average inclinations are with respect to the invariable plane.
[d]Known binary objects (Noll et al. 2008a, Grundy et al. 2009).
[e]Known presence of rotational lightcurve (Ortiz et al. 2003, Sheppard et al. 2008). The radius presented is an effective radius assuming a spherical body.
[f]Albedo and radius results from Stansberry et al. (2008) have been remodeled from their Spitzer flux measurements using our method.
[g]For binary objects, the minimum and maximum radius stated are for the brighter component assuming that the primary and secondary have equal albedos.
[h]Albedos and radii from Grundy et al. (2005). If the object is designated binary, then its albedo and radius were determined from the binary system mass assuming a range for the bulk density of 0.5 to 2.0 g/cm^3.
[i]Albedos and radii from binary system mass (Grundy et al. 2009).
[j]Davies et al. (2000).
[k]Boehnhardt et al. (2001).
[l]Jewitt and Luu (2001).
[m]de Bergh et al. (2005).
[n]Doressoundiram et al. (2002).
[o]Boehnhardt et al. (2004).
[p]DeMeo et al. (2009).
[q]Tegler et al. (1997).
[r]Delsanti et al. (2001).
[s]Luu and Jewitt (1996).
[t]Tegler et al. http://www.physics.nau.edu/~tegler/research/survey.htm
[u]Fornasier et al. (2004).
[v]Doressoundiram et al. (2001).
[w]Boehnhardt et al. (2002).
[x]Tegler et al. (2003).
[y]Dotto et al. (2003).
[z]Doressoundiram et al. (2007).
[aa]Stephens et al. (2003).

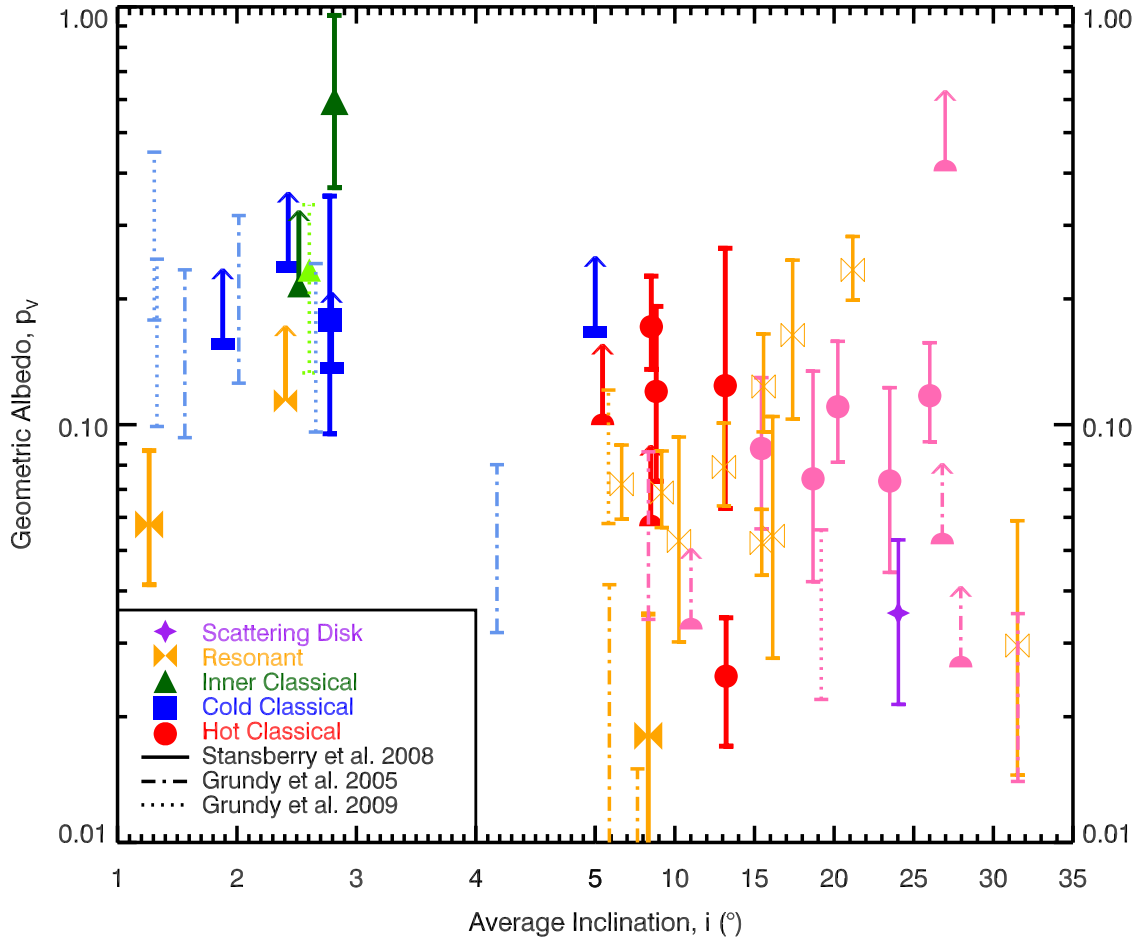

Figure 5.12. The visual geometric albedo, p_V, is plotted versus the 10 Myr mean inclination, i. The symbols are as in Figure 5.1 with the addition of solid orange bow ties for P3542 Resonant KBOs, open orange bowties for Resonant KBOs from Stansberry et al. (2008), orange dot-dashed lines for Resonant KBOs from Grundy et al. (2005), and orange dotted lines for Resonant KBOs from Grundy et al. (2009). The purple diamond represents the Scattering Disk object from Stansberry et al. (2008).

Including the Resonant objects and the Scattering Disk object in Figure 5.12 does not add greatly to our understanding of how albedo is related to inclination. The Resonant KBOs from the combined sample have a wide range of albedos. Among the Resonant KBOs, there does not appear to be a trend in albedo with inclination. The possible trend of decreasing albedo with decreasing inclination is upset by the moderate to high albedo of 2001 KD_{77}.

The currently accepted theory is that Resonant KBOs were swept up by Neptune

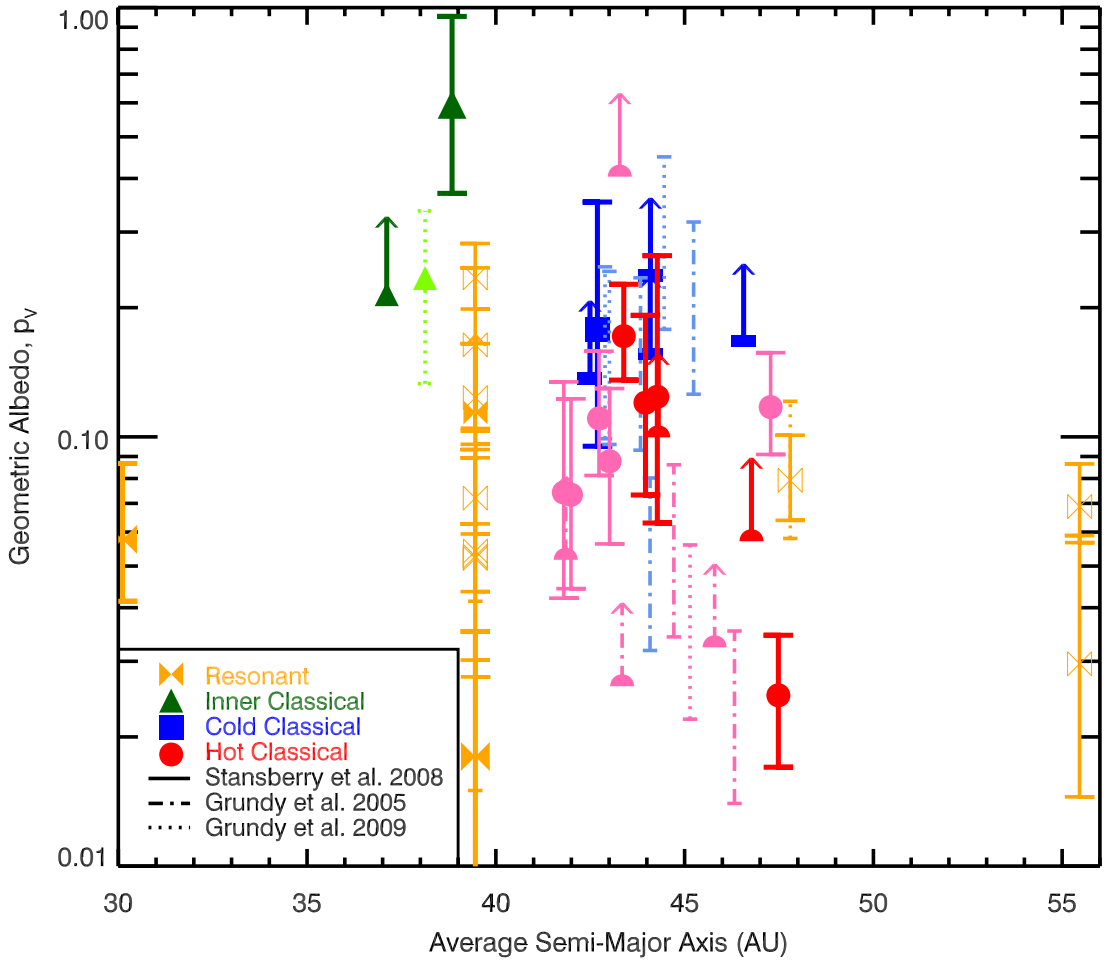

Figure 5.13. The visual geometric albedo, p_V, is plotted versus the 10 Myr mean semimajor axis, a. The symbols are as in Figure 5.2 with the addition of solid orange bow ties for P3542 Resonant objects, open orange bowties for Resonant objects from Stansberry et al. (2008), and orange dot-dashed lines for Resonant objects from Grundy et al. (2005). The Scattering Disk object from Stansberrty et al. (2008) does not appear because its semimajor axis is 83.6 AU.

as it migrated outward. Thus Resonant KBOs are not expected to have the same dynamical evolutionary history as Classical KBOs unless the Classicals were deposited from the 2:1 MMR during Neptune's outward migration. The Scattering Disk objects also should have a much different history than Classical KBOs. As a result, the relationships between albedo and inclination may be different for the different dynamical classes. The SDOs may have randomized inclinations that no longer correlate with formation location.

In Figure 5.13, we see that the Resonant KBOs do not shed additional light on the relationship between albedo and semimajor axis either. The most probable reason for this is the different dynamical histories for the different TNO populations.

Chapter 6

Discussion and Conclusions

6.1 Discussion

We have shown that dynamically cold Classical KBOs are drawn from a different parent distribution of visual geometric albedos than small hot Classicals. The cold Classical albedos are much higher (more reflective) than 0.04 which has been previously assumed (e.g. Jewitt and Luu 1993, Bernstein et al. 2004) because 0.04 is the average comet albedo and the Kuiper belt is the source of JFCs. In fact, the cold Classical albedos in our sample were higher than even we had presumed which resulted in non-detections in the 70 μm channel for many of the objects. Given that cold Classicals differ from other TNO populations in magnitude, color distribution, albedo distribution, and rate of binarity, they must have a different history than the other populations. Evolutionary models are being adjusted to account for this. For example, an expansion on the Nice model pushes out objects that were farther away from Neptune to become cold Classicals and scatters up and out excited objects close to Neptune to become hot Classicals (Levison et al. 2008).

Hot Classicals with high albedos may exist. The hot Classical population consists of objects with a diverse range of properties. Since there are hot Classicals that are red and that are binary, it is quite possible that there are hot Classicals with high albedos. The study involved in P3542 was not designed to rule out their existence.

The radius and albedo derived for Quaoar is consistent with those of Stansberry et al. (2008) and close but smaller and more reflective than those of Brown and Trujillo (2004). We conclude that our image reduction and modeling methods are self-consistent;

however, further information is required to determine the cause of the discrepancy between our results and those of Brown and Trujillo (2004).

As stated previously, the albedos of KBOs have often been assumed to be 0.04. The mass distribution and total mass estimate of the Kuiper belt have been determined using this value (i.e. Bernstein et al. 2004). We propose that the mass distribution and total mass estimate of the Kuiper belt should be adjusted to account for the results of Brucker et al. (2009) and Stanberry et al (2008). Stansberry et al. (2008) found an average albedo for TNOs that are not cold Classicals of 0.0988 and we have shown that the albedos of cold Classicals in our sample are greater than the albedos of hot Classicals. If the albedo of an object is underestimated, then its radius will be overestimated and its mass will be greatly overestimated. For example, consider a KBO of albedo 0.20 which was assumed to be 0.10. As a consequence, the true albedo has been underestimated by 2^{-1}, the radius has been overestimated by $2^{1/2}$, and the mass has been overestimated by $2^{3/2}$. If the true albedo is 0.40 when assumed to be 0.10, then the albedo has been underestimated by 2^{-2}, the radius overestimated by 2^{1}, and the mass overestimated by 2^{3}. Bernstein et al. (2004) derived a total mass for the cold Classical population of approximately 9×10^{-3} Earth-masses using an albedo of 0.04. If we apply an albedo of 0.20 to their equation for the total mass of the cold Classicals, we calculate an approximate mass of 8×10^{-4} Earth-masses. This is a reduction in the mass estimate by a factor of $5^{-3/2}$ or about 0.1. Furthermore, their formula assumes that TNOs have a density of 1 g/cm^3. Noll et al. (2008a) have recently compiled the available binary data which shows that some TNO binaries have densities less than 1 g/cm^3, so it is possible that the cold Classical population has a total mass even smaller than 8×10^{-4} Earth-masses.

2001 KD_{77}, the 3:2 Resonant KBO observed as part of P50540, did not reveal any additional information to support or contradict the theory that inner Classicals are former members of the low inclination 3:2 Resonant population that have dropped out of resonance as Neptune migrated. A new study on the colors of inner Classicals has revealed that they can be red or gray and do not share the same red distribution as cold Classicals (Romanishin et al. 2008, 2009). Thus, we will not be able to extrapolate definitively from the relationship between the 3:2 Resonant KBOs and inner Classicals to the relationship between the 2:1 Resonant KBOs and cold Classicals.

A possible trend in the albedos of 3:2 Resonant KBOs with inclination was hypothesized by Grundy et al. (2005). It appears that for 3:2 Resonant KBOs with inclinations greater than 5º, albedo increases with increasing inclination. However, the albedo of 2001 KD_{77}, which has an inclination of 2.4º, is much higher than would be extrapolated from the apparent trend.

In our thermal modeling, we employed a linear function for the phase integral: $q = 0.336 * p_V + 0.497$. We adopted this function as opposed to the canonical constant for rocky asteroids of 0.39 since, although the phase integral has not been measured yet for any TNOs, the phase integrals of icy satellites of gas giants exceed 0.39. Using 0.39 alters the value of the Bond albedo for thermophysical modeling to a less realistic value. Our function is not the true relationship but it is at least more physically realistic for TNOs.

As discussed in section 1.4, the scattered disk may not contain enough comet-sized objects to maintain the population of JFCs (Volk and Malhotra 2008). However, the fact that cold Classical KBOs are red with high albedos should not rule them out as an

ancillary source of JFCs (blue with low albedos; Jewitt 2002). During its passage from the main Kuiper belt, an object may undergo collisional fragmentation and structural alteration (Farinella and Davis 1996, Davis and Farinella 1997, Pan and Sari 2005) and will experience an increase in the intensity of sunlight. An increase in solar exposure will lead to possible cometary activity (Jewitt 2002) and the sublimation of water ice. The loss of water ice may reduce the observed redness and the albedo of objects whose surfaces contain red colored materials (Grundy 2009). Thus if an object escapes from the Classical Kuiper belt and becomes a JFC, then by that time it may very well be transformed enough to fit in with other JFCs.

After completing its flyby of Pluto in 2015, *New Horizons* will be redirected to flyby an additional KBO. This KBO, which is still to be discovered, will most likely be a cold Classical KBO. As such, the results of this study will be pivotal in interpreting the data sent back by the spacecraft.

6.2 Conclusions

By modeling flux measurements from images taken with *SST*/MIPS, we have constrained the albedos and radii of sixteen transneptunian objects, fourteen of which had not been observed previously with the *SST*. Eleven of the TNOs are classified as hot or cold Classical KBOs according to Gladman et al. (2008). The hot and cold Classicals in our sample with V-R colors are red. We therefore showed that albedo is not correlated with V-R as the red objects spanned a wide range of albedos. Based on albedos from our Classical sample and those of Stansberry et al. (2008), Grundy et al. (2005), and Grundy et al. (2009), we determined that, for an inclination boundary between 2.4º and 8.8º between the dynamically hot and cold Classical KBOs, the albedos of the two populations are drawn from different parent distributions. The dynamically cold Classical Kuiper belt objects, in general, have higher albedos than hot Classical KBOs. This increases support for orbital dynamic evolution theories involving separate origins and/or methods of transport to current orbits for the two populations.

The Neptune Trojan and the moderate-inclination 3:2 Resonant KBO have low albedos and the low inclination 3:2 Resonant KBO has an inclination greater than 0.11. Unfortunately, we did not obtain enough measurements to explore the relationship between cold Classicals and the low inclination members of the 2:1 MMR or the relationship between inner Classicals and the low inclination members of the 3:2 MMR.

The mass estimate of the cold Classical Kuiper belt should be revised downward about one order of magnitude to 8×10^{-4} Earth-masses due to the high albedos of this population. As a result, orbital evolution models will need to account for the increased amount of mass depletion in the Kuiper belt from primordial mass estimates.

Future observations with the *Herschel Space Observatory (HSO)* and the *James Webb Space Telescope* (*JWST*) hopefully will reveal whether or not the cold Classicals are former members of the 2:1 MMR that have been released. The *Herschel* Open Time Key Programme "TNOs Are Cool: A Survey of the Transneptunian Region" will be a great opportunity for further study of the albedos of Kuiper belt objects. This project proposes to observe a wide sample of objects from different dynamical classes at two infrared wavelength bands (Müller 2009). In addition to increasing the number of objects with albedo constraints, future observations will continue to expand on the search for binary TNOs and to measure the colors of additional objects as only about one third of the objects with well-defined orbits have published color indices. These TNO properties will tell us more about the formation and evolution of the solar system and can help us interpret disks about other stars as well.

References

Allen, R. L., Bernstein, G. M., Malhotra, R. 2002. Observational Limits on a Distant Cold Kuiper Belt. Astron. J. 124, 2949-2954.

Bagnulo, S., Belskaya, I., Muinonen, K., Tozzi, G. P., Barucci, M. A., Kolokolova, L., Fornasier, S. 2008. Discovery of Two Distinct Polarimetric Behaviours of Trans-Neptunian Objects. Astron. Astrophys. 491, L33-L36.

Barkume, K. M., Brown, M. E., Schaller, E. L. 2008. Near-Infrared Spectra of Centaurs and Kuiper Belt Objects. Astron J. 135, 55-67.

Barucci, M. A., Doressoundiram, A., Tholen, D., Fulchignoni, M., Lazzarin, M. 1999. Spectrophotometric Observations of Edgeworth-Kuiper Belt Objects. Icarus 142, 476-481.

Barucci, M. A., Romon, J., Doressoundiram, A., Tholen, D. J. 2000. Compositional Surface Diversity in the Trans-Neptunian Objects. Astron. J. 120, 496-500.

Benecchi, S. D., Noll, K. S., Grundy, W. M., Buie, M. W., Stephens, D. C., Levison, H. F., 2009. The Correlated Colors of Transneptunian Binaries. Icarus 200, 292-303.

Bernstein, G. N., Trilling, D. E., Allen, R. L., Brown, M. E., Holman, M., Malhotra, R. 2004. The Size Distribution of Trans-Neptunian Bodies. Astron. J. 128, 1364-1390.

Bianco, F., Protopapas, P., Alcock, C., McLeod, B. 2009a. New Constraints of the Small Size End of the Kuiper Belt Size Distribution from Occultation Surveys. Amer. Astron. Soc. mtg #213 poster 600.02, late abstract. http://www.abstractsonline.com/viewer/viewAbstract.asp?CKey={2AF113BC-9411-4745-94D0-E7E806E2E135}&MKey={8BEA5639-3EBB-47BD-9147-059E7CBA4CB4}&AKey={AAF9AABA-B0FF-4235-8AEC-74F22FC76386}&SKey={5A0867CD-CA57-49A3-9ED3-C3D7F6A1D943}

Bianco, F. B., Protopapas, P., McLeod, B. A., Alcock, C. R., Holman, M. J., Lehner, M. J. 2009b. A Search for Occultations of Bright Stars by Small Kuiper Belt Objects using Megacam on the MMT. Astron. J. 138, 568-578.

Boehnhardt, H., Tozzi, G. P., Birkle, K., Hainaut, O., Sekiguchi, T., Vair, M., Watanabe, J., Rupprecht, G., the FORS Instrument Team 2001. Visible and Near-IR Observations of Transneptunian Objects. Results from ESO and Calar Alto Telescopes. Astron. Astrophys. 378, 653-667.

Boehnhardt, H., 17 colleagues 2002. ESO Large Program on Physical Studies of Transneptunian Objects and Centaurs: Visible Photometry – First Results. Astron. Astrophys. 395, 297-303.

Boehnhardt, H., Bagnulo, S., Muinonen, K., Barucci, M. A., Kolokolova, L., Dotto, E., Tozzi, G. P. 2004. Surface Characterization of 28978 Ixion (2001 KX_{76}). Astron. Astrophys. 415, L21-L25.

Bowell, E., Hapke, B., Domingue, D., Harris, A. W. 1989. Application of Photometric Models to Asteroids. In: Binzel, R. P., Gehrels, T., Matthews, M. S. (Eds.), Asteroids II. Univ. of Arizona Press, Tucson, pp. 524-556.

Brown, M. E. 2001. The Inclination Distribution of the Kuiper Belt. Astron. J. 121, 2804-2814.

Brown, M. E., Trujillo, C. A. 2004. Direct Measurement of the Size of the Large Kuiper Belt Object (50000) Quaoar. Astron. J. 127, 2413-2417.

Brown, M. E., Barkume, K. M., Ragozzine, D., Schaller, E. L. 2007. A Collisional Family of Icy Objects in the Kuiper Belt. Nature 446, 294-296.

Brown, R. H., Matson, D. L. 1987. Thermal Effects of Insolation Propagation into the Regoliths of Airless Bodies. Icarus 72, 84-94.

Brucker, M. J., Grundy, W. M., Stansberry, J. A., Spencer, J. R., Sheppard, S. S., Chiang, E. I., Buie, M. W. 2009. High Albedos of Low Inclination Classical Kuiper Belt Objects. Icarus 201, 284-294.

Buie, M. W., Bus, S. J. 1992. Physical Observations of (5145) Pholus. Icarus 100, 288-294.

Buratti, B., Wong, F., Mosher, J. 1990. Surface Properties and Photometry of the Uranian Satellites. Icarus 84, 203-214.

Chiang, E. I., Brown, M. E. 1999. Keck Pencil-Beam Survey for Faint Kuiper Belt Objects. Astron. J. 118, 1411-1422.

Chiang, E., Lithwick, Y., Murray-Clay, R., Buie, M., Grundy, W., Holman, M. 2007. A Brief History of Trans-Neptunian Space. In: Reipurth, B., Jewitt, D., Keil, K. (Eds.), Protostars and Planets V. Univ. of Arizona Press, Tucson, pp. 895-911.

Cook, J. 2007. Dissecting Intermediate-Sized Kuiper Belt Objects. PhD Dissertation, Arizona State University, Tempe. 253 pp.

Cooper, J. F., Christian, E. R., Richardson, J. D., Wang, C. 2003. Proton Irradiation of Centaur, Kuiper Belt, and Oort Cloud Objects at Plasma to Cosmic Ray Energy. Earth Moon Planets 92, 261-277.

Cruikshank, D. P., Brown, R. H. 1986. Satellites of Uranus and Neptune, and the Pluto-Charon System. In: Burns, J. A., Matthews, M. S. (Eds.), Satellites. Univ. of Arizona Press, Tucson, pp. 836-873.

Davies, J. K., Green, S., McBride, N., Muzzerall, E., Tholen, D. J., Whiteley, R. J., Foster, M. J., Hillier, J. K. 2000. Visible and Infrared Photometry of Fourteen Kuiper Belt Objects. Icarus 146, 253-262.

Davis, D. R., Farinella, P. 1997. Collisional Evolution of Edgeworth-Kuiper Belt Objects. Icarus 125, 50-60.

de Bergh, C., Delsanti, A., Tozzi, G. P., Dotto, E., Doressoundiram, A., Barucci, M. A. 2005. The Surface of the Transneptunian Object 90482 Orcus. Astron. Astrophys. 437, 1115-1120.

Delsanti, A. C., Boehnhardt, H., Barrera, L., Meech, K. J., Sekiguchi, T., Hainaut, O. R. 2001. BVRI Photometry of 27 Kuiper Belt Objects with ESO/Very Large Telescope. Astron. Astrophys. 380, 347-358.

DeMeo, F. E., Fornasier, S., Barucci, M. A., Perna, D., Protopapa, S., Alvarez-Candal, A., Delsanti, A., Doressoundiram, A., Merlin, F., de Bergh, C. 2009. Visible and Near-Infrared Colors of Transneptunian Objects and Centaurs from the Second ESO Large Program. Astron. Astrophys. 493, 283-290.

Doressoundiram, A., Barucci, M. A., Romon, J., Veillet, C. 2001. Multicolor Photometry of Trans-neptunian Objects. Icarus 154, 277-286.

Doressoundiram, A., Peixinho, N., de Bergh, C., Fornasier, S., Thébault, P., Barucci, M. A., Veillet, C. 2002. The Color Distribution in the Edgeworth-Kuiper Belt. Astron. J. 124, 2279-2296.

Doressoundiram, A., Peixinho, N., Doucet, C., Mousis, O., Barucci, M. A., Petit, J.-M., Veillet, C. 2005. The Meudon Multicolor Survey (2MS) of Centaurs and Trans-Neptunian Objects: Extended Dataset and Status on the Correlations Reported. Icarus 174, 90-104.

Doressoundiram, A., Peixinho, N., Moullet, A., Fornasier, S., Barucci, M. A., Beuzit, J. L., Veillet, C. 2007. The Meudon Multicolor Survey (2MS) of Centaurs and Trans-Neptunian Objects: From Visible to Infrared Colors. Astron. J. 134, 2186-2199.

Doressoundiram, A., Boehnhardt, H., Tegler, S. C., Trujillo, C. 2008. Color Properties and Trends of the Transneptunian Objects. In: Barucci, M. A., Boehnhardt, H., Cruikshank, D. P., Morbidelli, A. (Eds.), The Solar System Beyond Neptune. Univ. of Arizona Press, Tucson, pp. 91-104.

Dotto, E., Barucci, M. A., Boehnhardt, H., Romon, J., Doressondiram, A., Peixinho, N., de Bergh, C., Lazzarin, M. 2003. Searching for Water Ice on 47171 1999 TC_{36}, 1998 SG_{35}, and 2000 QC_{243}: ESO Large Program on TNOs and Centaurs. Icarus 162, 408-414.

Duncan, M., Quinn, T., Tremaine, S. 1988. The Origin of Short-Period Comets. Astrophys. J. 328, L69-L73.

Elliot, J. L., 10 colleagues 2005. The Deep Ecliptic Survey: A Search for Kuiper Belt Objects and Centaurs. II. Dynamical Classification, the Kuiper Belt Plane, and the Core Population. Astron. J. 129, 1117-1162.

Engelbracht, C. W., 25 colleagues 2007. Absolute Calibration and Characterization of the Multiband Imaging Photometer for *Spitzer*. I. The Stellar Calibrator Sample and the 24 μm Calibration. Publ. Astron. Soc. Pacific 119, 994-1018.

Farinella, P., Davis, D. R. 1996. Short-Period Comets: Primordial Bodies or Collisional Fragments? Science 273, 938-941.

Feigelson, E. D., Nelson, P. I. 1985. Statistical Methods for Astronomical Data with Upper Limits: I. Univariate Distributions. Astrophys. J. 293, 192-206.

Fernandez, J. A., Ip, W.-H. 1984. Some Dynamical Aspects of the Accretion of Uranus and Neptune: The Exchange of Orbital Angular Momentum with Planetesimals. Icarus 58, 109-120.

Ford, E. B., Chiang, E. I. 2007. The Formation of Ice Giants in a Packed Oligarchy: Instability and Aftermath. Astrophys. J. 661, 602-615.

Fornasier, S., Doressoundiram, A., Tozzi, G. P., Barucci, M. A., Boehnhardt, H., de Bergh, C., Delsanti, A., Davies, J., Dotto, E. 2004. ESO Large Program on Physical Studies of Trans-Neptunian Objects and Centaurs: Final Results of the Visible Spectrophotometric Observations. Astron. Astrophys. 421, 353-363.

Fraser, W. C., Kavelaars, J. J. 2009. The Size Distribution of Kuiper Belt Objects for $D \geq 10$ km. Astron. J. 137, 72-82.

Fraser, W. C., Kavelaars, J. J., Holman, M. J., Pritchet, C. J., Gladman, B. J., Grav, T., Jones, R. L., MacWilliams, J., Petit, J.-M. 2008. The Kuiper Belt Luminosity Function from $m_R = 21$ to 26. Icarus 195, 827-843.

Fuentes, C. I., Holman, M. J. 2008. A Suburu Archival Search for Faint Trans-Neptunian Objects. Astron. J. 136, 83-97.

Gil-Hutton, R., Licandro, J. 2001. VR Photometry of Sixteen Kuiper Belt Objects. Icarus 152, 246-250.

Gladman, B., Kavelaars, J. J., Petit, J.-M., Morbidelli, A., Holman, M. J., Loredo, T. 2001. The Structure of the Kuiper Belt: Size Distribution and Radial Extent. Astron. J. 122, 1051-1066.

Gladman, B., Marsden, B. G., VanLaerhoven, C. 2008. Nomenclature in the Outer Solar System. In: Barucci, M. A., Boehnhardt, H., Cruikshank, D. P., Morbidelli, A. (Eds.), The Solar System Beyond Neptune. Univ. of Arizona Press, Tucson, pp. 43-57.

Gladman, B., Kavelaars, J., Petit, J.-M., Ashby, M. L. N., Parker, J., Coffey, J., Jones, R. L., Rousselot, P., Mousis, O. 2009. Discovery of the First Retrograde Transneptunian Object. Astrophys. J. 697, L91-L94.

Gomes, R. 2009. On the Origin of the Kuiper Belt. Celest. Mech. Dynam. Astron. 104, 39-51.

Gomes, R., Levison, H. F., Tsiganis, K., Morbidelli, A. 2005. Origin of the Cataclysmic Late Heavy Bombardment Period of the Terrestrial Planets. Nature 435, 466-469.

Gordon, K. D., 29 colleagues 2005. Reduction Algorithms for the Multiband Imaging Photometer for *Spitzer*. Publ. Astron. Soc. Pacific 117, 503-525.

Gordon, K. D., 23 colleagues 2007. Absolute Calibration and Characterization of the Multiband Imaging Photometer for *Spitzer*. II. 70 μm Imaging. Publ. Astron. Soc. Pacific 119, 1019-1037.

Grundy, W. M. 2009. Is the Missing Ultra-Red Material Colorless Ice? Icarus 199, 560-563.

Grundy, W. M., Noll, K. S., Stephens, D. C. 2005. Diverse Albedos of Small Trans-Neptunian Objects. Icarus 176, 184-191.

Grundy, W. M., 14 colleagues and the New Horizons team 2007. New Horizons Mapping of Europa and Ganymede. Science 318, 234-237.

Grundy, W. M., Noll, K. S., Buie, M. W., Benecchi, S. D., Stephens, D. C., Levison, H. F. 2009. Mutual Orbits and Masses of Six Transneptunian Binaries. Icarus 200, 627-635.

Guilbert, A., Alvarez-Candal, A., Merlin, F., Barucci, M. A., Dumas, C., de Bergh, C., Delsanti, A. 2009. ESO-Large Program on TNOs: Near-Infrared Spectroscopy with SINFONI. Icarus 201, 272-283.

Gulbis, A. A. S., Elliot, J. L., Kane, J. F. 2006. The Color of the Kuiper Belt Core. Icarus 183, 168-178.

Hainaut, O., Delsanti, A. 2002. Colors of Minor Bodies in the Outer Solar System: A Statistical Analysis. Astron. Astrophys. 389, 641-664. http://www.sc.so.org/~ohainaut/MBOSS

Hansen, O. L. 1977. An Explication of the Radiometric Method for Size and Albedo Determination. Icarus 31, 456-482.

Heim, G. B., Henderson, M. L., Macfeely, K. I., McMahon, T. J., Michika, D., Pearson, R. J., Rieke, G. H., Schwenker, J. P., Strecker, D. W., Thompson, C. L., Warden, R. M., Wilson, D. A., Young, E. T. 1998. Multiband Imaging Photometer for SIRTF. In: Bely, P. Y., Breckinridge, J. B. (Eds.), Space Telescopes and Instruments V. Proc. SPIE 3356, 985-1000.

Isobe, T., Feigelson, E. D., Nelson, P. I. 1986. Statistical Methods for Astronomical Data with Upper Limits: II. Correlation and Regression. Astrophys. J. 306, 490-507.

Jewitt, D. C. 2002. From Kuiper Belt Object to Cometary Nucleus: the Missing Ultrared Matter. Astron. J. 123, 1039-1049.

Jewitt, D. C., Luu, J. X. 1993. Discovery of the Candidate Kuiper Belt Object 1992 QB_1. Nature 362, 730-732.

Jewitt, D. C., Luu, J. X. 2001. Colors and Spectra of Kuiper Belt Objects. Astron. J. 122, 2099-2114.

Jewitt, D. C., Luu, J. 2004. Crystalline Water Ice on the Kuiper Belt Object (50000) Quaoar. Nature 432, 731-733.

Jewitt, D., Peixinho, N., Hsieh, H. H. 2007. U-Band Photometry of Kuiper Belt Objects. Astron. J. 134, 2046-2053.

Kavelaars, J. J., Jones, L., Gladman, B., Parker, J. W., Petit, J.-M. 2008. The Orbital and Spatial Distribution of the Kuiper Belt. In: Barucci, M. A., Boehnhardt, H., Cruikshank, D. P., Morbidelli, A. (Eds.), The Solar System Beyond Neptune. Univ. of Arizona Press, Tucson, pp. 59-69.

Kavelaars, J. J., 17 colleagues 2009. The Canada-France Ecliptic Plane Survey – L3 Data Release: The Orbital Structure of the Kuiper Belt. Astron. J. 137, 4917-4935.

Kenyon, S. J., Bromley, B. C. 2004. The Size Distribution of Kuiper Belt Objects. Astron. J. 128, 1916-1926.

Kenyon, S. J., Luu, J. X. 1998. Accretion in the Early Kuiper Belt. I. Coagulation and Velocity Evolution. Astron. J. 115, 2136-2160.

Kenyon, S. J., Windhorst, R. A. 2001. The Kuiper Belt and Olber's Paradox. Astrophys. J. 547: L69-L73.

Krist, J. 2002. Tiny Tim/*SIRTF* User's Guide (Pasadena: SSC).

Larsen, J. A., Gleason, A. E., Danzl, N. M., Descour, A. S., McMillan, R. S., Gehrels, T., Jedicke, R., Montani, J. L., Scotti, J. V. 2001. The Spacewatch Wide-Area Survey for Bright Centaurs and Trans-Neptunian Objects. Astron. J. 121, 562-579.

LaValley, M., Isobe, T., Feigelson, E. D. 1990. ASURV. Bull. Amer. Astron. Soc. (software reports) 22, 917-918.

Lebofsky, L. A., Spencer, J. R. 1989. Radiometry and Thermal Modeling of Asteroids. In: Binzel, R. P., Gehrels, T., Matthews, M. S. (Eds.), Asteroids II. Univ. of Arizona Press, Tucson, pp. 128-147.

Levison, H. F., Duncan, M. J. 1997. From the Kuiper Belt to Jupiter-Family Comets: the Spatial Distribution of Ecliptic Comets. Icarus 127, 13-32.

Levison, H. F., Morbidelli, A. 2003. The Formation of the Kuiper Belt by the Outward Transport of Bodies during Neptune's Migration. Nature 426, 419-421.

Levison, H. F., Morbidelli, A. 2007. Models of the Collisional Damping Scenario for Ice-Giant Planets and Kuiper Belt Formation. Icarus 189, 196-212.

Levison, H. F., Stern, S. A. 2001. On the Size Dependence of the Inclination Distribution of the Main Kuiper Belt. Astron. J. 121, 1730-1735.

Levison, H. F., Morbidelli, A., Dones, L. 2004. Sculpting the Kuiper Belt by a Stellar Encounter: Constraints from the Oort Cloud and Scattered Disk. Astron. J. 128, 2553-2563.

Levison, H. F., Morbidelli, A., VanLaerhoven, C., Gomes, R., Tsiganis, K. 2008. Origin of the Structure of the Kuiper Belt during a Dynamical Instability in the Orbits of Uranus and Neptune. Icarus 196, 258-273.

Luu, J., Jewitt, D. 1996. Color Diversity among the Centaurs and Kuiper Belt Objects. Astron. J. 112, 2310-2318.

Lykawka, P. S., Mukai, T. 2005. Higher Albedos and Size Distribution of Large Transneptunian Objects. Planet. Space Science 53, 1319-1330.

Lykawka, P. S., Mukai, T. 2007a. Origin of Scattered Disk Resonant TNOs: Evidence for an Ancient Excited Kuiper Belt of 50 AU Radius. Icarus 186, 331-341.

Lykawka, P. S., Mukai, T. 2007b. Dynamical Classification of Trans-Neptunian Objects: Probing Their Origin, Evolution, and Interrelation. Icarus 189, 213-232.

Malhotra, R. 1993. The Origin of Pluto's Peculiar Orbit. Nature 365, 819-821.

Malhotra, R. 1995. The Origin of Pluto's Orbit: Implications for the Solar System beyond Neptune. Astron. J. 110, 420-429.

Morbidelli, A. 2007. Portrait of a Suburban Family. Nature 446, 273-274.

Morbidelli, A., Levison, H. F. 2004. Scenarios for the Origin of the Orbits of the Trans-Neptunian Objects 2000 CR_{105} and 2003 VB_{12} (Sedna). Astron. J. 128, 2564-2576.

Morbidelli, A., Levison, H. F., Gomes, R. 2008. The Dynamical Structure of the Kuiper Belt and Its Primordial Origin. In: Barucci, M. A., Boehnhardt, H., Cruikshank, D. P., Morbidelli, A. (Eds.), The Solar System Beyond Neptune. Univ. of Arizona Press, Tucson, pp. 275-292.

Morrison, D. 1973. Determination of Radii of Satellites and Asteroids from Radiometry and Photometry. Icarus 19, 1-14.

Morrison, D., Owen, T., Soderblom, L. A. 1986. The Satellites of Saturn. In: Burns, J. A., Matthews, M. S. (Eds.), Satellites. Univ. of Arizona Press, Tucson, pp. 764-801.

Müller, T. G., 32 colleagues 2009. TNOs are Cool: A Survey of the Transneptunian Region. Earth Moon Planets DOI 10.1007/s11038-009-9307-x.

Murray-Clay, R. A., Chiang, E. I. 2006. Brownian Motion in Planetary Migration. Astrophys. J. 651, 1194-1208.

Noll, K. S., Grundy, W. M., Chiang, E. I., Margot, J.-L., Kern, S. D. 2008a. Binaries in the Kuiper Belt. In: Barucci, M. A., Boehnhardt, H., Cruikshank, D. P., Morbidelli, A. (Eds.), The Solar System Beyond Neptune. Univ. of Arizona Press, Tucson, pp. 345-363.

Noll, K. S., Grundy, W. M., Stephens, D. C., Levison, H. F., Kern, S. D. 2008b. Evidence for Two Populations of Classical Transneptunian Objects: The Strong Inclination Dependence of Classical Binaries. Icarus 194, 758-768.

Ortiz, J. L., Gutiérrez, P. J., Sota, A., Casanova, V., Teixeira, V. R. 2003. Rotational Brightness Variations in Trans-Neptunian Object 50000 Quaoar. Astron. Astrophys. 409, L13-L16.

Ortiz, J. L., Sota, A., Moreno, R., Lellouch, E., Biver, N., Doressoundiram, A., Rousselot, P., Gutiérrez, P. J., Márquez, I., González Delgado, R. M., Casanova, V. 2004. A Study of Trans-Neptunian Object 55636 (2002 TX_{300}). Astron. Astrophys. 420, 383-388.

Osip, D. J., Kern, S. D., Elliot, J. L. 2003. Physical Characterization of the Binary Edgeworth-Kuiper Belt Object 2001 QT_{297}. Earth Moon Planets 92, 409-421.

Pan, M., Sari, R. 2005. Shaping the Kuiper Belt Size Distribution by Shattering Large but Strengthless Bodies. Icarus 173, 342-348.

Peixinho, N. 2008. Deconstructing the Correlations among Classical KBOs: In the End, There Can Be Only One. Bull. Amer. Astron. Soc. 40: 465.

Peixinho, N., Boehnhardt, H., Belskaya, I., Doressoundiram, A., Barucci, M. A., Delsanti, A. 2004. ESO Large Program on Centaurs and TNOs: Visible Colors – Final Results. Icarus 170, 153-166.

Peixinho, N., Lacerda, P., Jewitt, D. 2008. Color-Inclination Relation of the Classical Kuiper Belt Objects. Astron. J. 136, 1837-1845.

Petit, J.-M., Holman, M. J., Gladman, B. J., Kavelaars, J. J., Scholl, H., Loredo, T. J. 2006. The Kuiper Belt Luminosity Function from m_R = 22 to 25. Monthly Not. Royal Astron. Soc. 365, 429-438.

Petit, J.-M., Kavelaars, J. J., Gladman, B., Loredo, T. 2008. Size Distribution of Multikilometer Transneptunian Objects. In: Barucci, M. A., Boehnhardt, H., Cruikshank, D. P., Morbidelli, A. (Eds.), The Solar System Beyond Neptune. Univ. of Arizona Press, Tucson, pp. 71-87.

Press, W. H., Teukolsky, S. A., Vetterling, W. T., Flannery, B. P. 1992. Numerical Recipes in C. Cambridge Univ. Press, New York.

Rieke, G. H., 42 colleagues 2004. The Multiband Imaging Photometer for *Spitzer* (MIPS). Astrophys. J. Supp. 154, 25-29.

Romanishin, W., Tegler, S. C. 2005. Accurate Absolute Magnitudes for Kuiper Belt Objects and Centaurs. Icarus 179, 523-526.

Romanishin, W., Tegler, S. C., Consolmagno, G. 2008. Colors of Inner Disk KBOs. Asteroids, Comets, Meteors X. Baltimore, MD. LPI Contribution No. 1405, paper I.D. 8331.

Romanishin, W., Tegler, S. C., Consolmagno, G. 2009. Colors of Inner Disk Classical Kuiper Belt Objects. Astron. J., submitted.

Santos-Sanz, P., Ortiz, J. L., Barrera, L., Boehnhardt, H. 2009. New BVRI Photometry Results on Kuiper Belt Objects from the ESO VLT. Astron. Astrophys. 494, 693-706.

Schaller, E. L., Brown, M. E. 2007a. Volatile Loss and Retention on Kuiper Belt Objects. Astrophys. J. 659, L61-L64.

Schaller E. L., Brown, M. E. 2007b. Detection of Methane on Kuiper Belt Object (50000) Quaoar. Astrophys. J. 670, L49-L51.

Schaller, E. L., Brown, M. E. 2008. Detection of Additional Members of the 2003 EL_{61} Collisional Family via Near-Infrared Spectroscopy. Astrophys. J. 684, L107-L109.

Schwamb, M. E., Brown, M. E., Rabinowitz, D. L. 2009. A Search for Distant Solar System Bodies in the Region of Sedna. Astrophys. J. 694, L45-L48.

Sheppard, S. S. 2007. Light Curves of Dwarf Plutonian Planets and Other Large Kuiper Belt Objects: Their Rotations, Phase Functions, and Absolute Magnitudes. Astron. J. 134, 787-798.

Sheppard, S. S., Jewitt, D. C. 2002. Time-Resolved Photometry of Kuiper Belt Objects: Rotations, Shapes, and Phase Functions. Astron. J. 124, 1757-1775.

Sheppard, S. S., Lacerda, P., Ortiz, J. L. 2008. Photometric Lightcurves of Transneptunian Objects and Centaurs: Rotations, Shapes, and Densities. In: Barucci, M. A., Boehnhardt, H., Cruikshank, D. P., Morbidelli, A. (Eds.), The Solar System Beyond Neptune. Univ. of Arizona Press, Tucson, pp. 129-142.

Simonelli, D. P., Kay, J., Adinolfi, D., Veverka, J., Thomas, P. C., Helfenstein, P. 1999. Phoebe: Albedo Map and Photometric Properties. Icarus 138, 249-258.

Spencer, J. R. 1987. The Surfaces of Europa, Ganymede, and Callisto: An Investigation Using Voyager IRIS Thermal Infrared Spectra. PhD Dissertation, University of Arizona, Tucson. 228 pp.

Spencer, J. R. 1990. A Rough-Surface Thermophysical Model for Airless Planets. Icarus 83, 27-38.

Spencer, J. R., Lebofsky, L. A., Sykes, M. V. 1989. Systematic Biases in Radiometric Diameter Determinations. Icarus 78, 337-354.

Stansberry, J. A., 17 colleagues 2007. Absolute Calibration and Characterization of the Multiband Imaging Photometer for *Spitzer*. III. An Asteroid-based Calibration of MIPS at 160μm. Publ. Astron. Soc. Pacific 119, 1038-1051.

Stansberry, J. A., Grundy, W. M., Brown, M., Cruikshank, D. P., Spencer, J., Trilling, D., Margot, J.-L. 2008. Physical Properties of Kuiper Belt Objects and Centaurs: *Spitzer Space Telescope* Constraints. In: Barucci, M. A., Boehnhardt, H., Cruikshank, D. P., Morbidelli, A. (Eds.), The Solar System Beyond Neptune. Univ. of Arizona Press, Tucson, pp. 161-179.

Stephens, D. C., Noll, K. S., Grundy, W. M., Millis, R. L., Spencer, J. R., Buie, M. W., Tegler, S. C., Romanishin, W., Cruikshank, D. P. 2003. HST Photometry of Trans-Neptunian Objects. Earth Moon Planets 92, 251-260.

Strazzulla, G., Cooper, J. F., Christian, E. R., Johnson, R. E. 2003. Ion Irradiation of TNOs: From the Fluxes Measured in Space to the Laboratory Experiments. Comptes Rendus Phys. 4, 791-801.

Tegler, S. C., Romanishin, W. 1997. The Extraordinary Colors of Trans-Neptunian Objects 1994 TB and 1993 SC. Icarus 126, 212-217.

Tegler, S. C., Romanishin, W. J. 2000. Extremely Red Kuiper-Belt Objects in Near-Circular Orbits beyond 40 AU. Nature 407, 979-981.

Tegler, S. C., Romanishin, W. J., Consolmagno, S. J., G. J. 2003. Color Patterns in the Kuiper Belt: A Possible Primordial Origin. Astrophys. J. 599, L49-L52.

Thomas, P. C., Veverka, J., Helfenstein, P. 1996. Neptune's Small Satellites. In: Cruikshank, D. (Ed.), Neptune and Triton. Univ. of Arizona Press, Tucson, pp. 685-699.

Trujillo, C. A., Brown, M. E. 2002. A Correlation between Inclination and Color in the Classical Kuiper Belt. Astrophys. J. 566, L125-L128.

Trujillo, C. A., Brown, M. E. 2003. The Caltech Wide Area Sky Survey. Earth Moon Planets 92, 99-112.

Trujillo, C. A., Jewitt, D. C., Luu, J. X. 2001. Properties of the Trans-Neptunian Belt: Statistics from the Canada-France-Hawaii Telescope Survey. Astron J. 122, 457-473.

Tsiganis, K., Gomes, R., Morbidelli, A., Levison, H. F. 2005. Origin of the Orbital Architecture of the Giant Planets of the Solar System. Nature 435, 459-461.

Veverka, J., Thomas, P., Johnson, T. V., Matson, D., Housen, K. 1986. The Physical Characteristics of Satellite Surfaces. In: Burns, J. A., Matthews, M. S. (Eds.), Satellites. Univ. of Arizona Press, Tucson, pp. 342-402.

Volk, K., Malhotra, R. 2008. The Scattered Disk as the Source of the Jupiter Family Comets. Astrophys. J. 687, 714-725.

Appendix A

Acronyms

AOR – astronomical observation request

CCD – charge-coupled device

CFEPS – Canada-France Ecliptic Plane Survey

DCE – data collection event

DES – Deep Ecliptic Survey

EKO – Edgworth-Kuiper Object

FOV – field of view

FWHM – full width half maximum

HRC – High Resolution Camera

HSO – Herschel Space Observatory

HST – Hubble Space Telescope

IDL – Interactive Data Language

ILM – Isothermal Latitude Model

JFC – Jupiter family comet

JPL – Jet Propulsion Laboratory

JWST – James Webb Space Telescope

KBO – Kuiper belt object

LDSS3 – Low Dispersion Survey Spectrograph 3

MBA – main belt asteroid

MIPS – Multiband Imaging Photometer for *Spitzer*

MMR – mean motion resonance

MMT – Multiple Mirror Telescope, Monolithic Mirror Telescope

NASA – National Aeronautics and Space Administration

NIR – near-infrared

OCIW – Observatories of the Carnegie Institution of Washington

PSF – point spread function

S/N – signal-to-noise ratio

SDO – Scattered/ing Disk Object

SIRTF – Space Infrared Telescope Facility

SST – Spitzer Space Telescope

STM – Standard Thermal Model

TAOS – Taiwanese-American Occultation Survey

TNO – transneptunian object

TPM – thermophysical model